

THE EFFECTS OF CARBON CONTENT ON THE PROPERTIES OF
PLASMA DEPOSITED AMORPHOUS SILICON CARBIDE THIN FILMS

A THESIS SUBMITTED TO
THE GRADUATE SCHOOL OF NATURAL AND APPLIED SCIENCE
OF
MIDDLE EAST TECHNICAL UNIVERSITY

BY

KIVANÇ SEL

IN PARTIAL FULFILLMENT OF THE REQUIREMENTS
FOR
THE DEGREE OF DOCTOR OF PHILOSOPHY
IN
PHYSICS

MARCH 2007

Approval of the Graduate School of Natural And Applied Sciences

Prof. Dr. Canan Özgen
Director

I certify that this thesis satisfies all the requirements as a thesis for the degree of Doctor of Philosophy.

Prof. Dr. Sinan Bilikmen
Head of Department

This is to certify that we have read this thesis and that in our opinion it is fully adequate, in scope and quality, as a thesis for the degree of Doctor of Philosophy.

Assoc. Prof. Dr. İsmail Atılgan
Supervisor

Examining Committee Members

Prof. Dr. Nizami Hasanli (METU, PHYS) _____

Assoc. Prof. Dr. İsmail Atılgan (METU, PHYS) _____

Prof. Dr. Bayram katırcıođlu (METU, PHYS) _____

Assoc. Prof. Dr. Osman Kodolbař (TÜBİTAK, UME) _____

Assist. Prof. Dr. Orhan Özdemir (Yıldız Technical Univ., PHYS) _____

I hereby declare that all information in this document has been obtained and presented in accordance with academic rules and ethical conduct. I also declare that, as required by these rules and conduct, I have fully cited and referenced all material and results that are not original to this work.

Name, Last name : Kıvanç SEL

Signature :

ABSTRACT

THE EFFECTS OF CARBON CONTENT ON THE PROPERTIES OF PLASMA DEPOSITED AMORPHOUS SILICON CARBIDE THIN FILMS

Sel, Kıvanç

Ph.D., Department of Physics

Supervisor: Assoc. Prof. Dr. İsmail Atılğan

March 2007, 122 pages

The structure and the energy band gap of hydrogenated amorphous silicon carbide are theoretically revised. In the light of defect pool model, density of states distribution is investigated for various regions of mobility gap. The films are deposited by plasma enhanced chemical vapor deposition system with various gas concentrations at two different, lower (30 mW/cm^2) and higher (90 mW/cm^2), radio frequency power densities. The elemental composition of hydrogenated amorphous silicon carbide films and relative composition of existing bond types are analyzed by x-ray photoelectron spectroscopy measurements. The thicknesses, deposition rates, refractive indices and optical band gaps of the films are determined by ultraviolet visible transmittance measurements. Uniformity of the deposited films is analyzed along the radial direction of the bottom electrode of the plasma enhanced chemical vapor deposition reactor. The molecular vibration characteristics of the films are reviewed and analyzed by Fourier

transform infrared spectroscopy measurements. Electrical characteristics of the films are analyzed by dc conductivity measurements. Conduction mechanisms, such as extended state, nearest neighbor and variable range hopping in tail states are revised. The hopping conductivities are analyzed by considering the density of states distribution in various regions of mobility gap. The experimentally measured activation energies for the films of high carbon content are too low to be interpreted as the difference between Fermi level and relevant band edge. This anomaly has been successfully removed by introducing hopping conduction across localized tail states of the relevant band. In other words, the second contribution lowers the mobility edge towards the Fermi level.

Keywords: Amorphous silicon carbide, DOS distribution, PECVD (Plasma enhanced chemical vapor deposition), optical constants, conduction mechanisms.

ÖZ

KARBON İÇERİĞİNİN PLAZMA İLE BİRİKTİRİLMİŞ AMORF SİLİSYUM KARBÜR İNCE FİLMLEİN ÖZELLİKLERİNE ETKİLERİ

Sel, Kıvanç

Doktora, Fizik Bölümü

Tez Yöneticisi: Doç. Dr. İsmail Atılgan

Mart 2007, 122 sayfa

Hidrojenlenmiş amorf silisyum karbürün yapısı ve enerji bant aralığı yapısı teorik olarak incelenmiştir. Kusur havuzu modeli ışığı altında, durum yoğunluğu dağılımı mobilite aralığının değişik bölgeleri için araştırılmıştır. Filmler farklı gaz konsantrasyonlarında ve alçak (30 mW/cm^2) ve yüksek (90 mW/cm^2) olmak üzere iki farklı radyo frekansı güç yoğunluğunda plazma destekli kimyasal buhar biriktirme sistemi ile büyütülmüştür. Hidrojenlenmiş amorf silisyum karbür filmlerin element kompozisyonu ve mevcut bağların tipleri x-ışını fotoelektron tayf ölçümleri ile analiz edilmiştir. Filmlerin kalınlıkları, büyüme oranları, kırılma indisleri ve optik bant aralıkları mor ötesi ve görünür bölge tayf ölçümleri ile belirlenmiştir. Büyütülen filmlerin düzenliliği plazma destekli kimyasal buhar biriktirme reaktörünün alt elektrotunun yarı çapı boyunca analiz edilmiştir. Filmlerin moleküler salınım karakterleri incelenmiş ve Fourier dönüşümü kızıl ötesi tayf ölçümleri ile analiz edilmiştir. Filmlerin elektriksel karakterleri dc iletkenlik ölçümleri ile analiz edilmiştir. Yaygın durumlarda iletim

ve bant eteđi durumlarında en yakın komşuya ve deđişik mesafelere hoplama iletimi gibi iletim mekanizmaları incelenmiştir. Hoplama iletimleri mobilite aralığının farklı bölgelerindeki durum yoğunluğu dağılımı göz önünde bulundurularak analiz edilmiştir. Yüksek karbon içerikli filmler için deneysel olarak ölçülmüş aktivasyon enerjileri, Fermi seviyesi ve ilgili bandın eşiđi arasındaki farkla karşılaştırıldığında çok düşük kalmaktadırlar. Bu anormallik ilgili bandın yerleşmiş etek durumlarındaki hoplama iletiminin devreye sokulması ile başarılı bir şekilde giderilmiştir. Başka bir deyişle, bu ikincil katkı, mobilite eşiđini Fermi seviyesine doğru görünüşte azaltmıştır.

Anahtar kelimeler: Amorf silisyum karbür, durum yoğunluğu dağılımı, PDKBB (Plazma destekli kimyasal buhar biriktirme), optik sabitler, iletim mekanizmaları.

ACKNOWLEDGMENTS

I would like to thank to my supervisor Assoc. Prof. Dr. İsmail Atılın for his support, helpful criticism and sharing his experience in laboratory works and data analysis, throughout this work.

I would like to thank to Prof. Dr. Bayram Katırcıođlu for instructive discussions and comments, and for sharing his knowledge and experiences.

I am thankful to my lab colleagues, Barıř Akaođlu and Oben Sezer for their friendship, co-operation and support.

I would like to thank the Scientific and Technical Research Council of Turkey for financial support during my study in Middle East Technical University.

I would also like to thank to Devrim Kōseođlu, Mustafa Kurt, Tolga Kaya for their friendship.

I would like to express my gratitude to my mother Meral Sel and my father Gūven Sel for their endless support and encouragement.

I am thankful to my wife, Emel, for her unshakable faith in me and for her understanding and support. I am also thankful to my daughter Melis for giving me enormous life energy and happiness in my difficult times. I sincerely apologize from my wife and daughter for times that we become apart during my long lasting works.

TABLE OF CONTENTS

ABSTRACT.....	iv
ÖZ.....	vi
ACKNOWLEDGMENTS.....	viii
TABLE OF CONTENTS.....	ix

CHAPTER

1. INTRODUCTION.....	1
2. THE CHARACTERISTICS OF HYDROGENATED AMORPHOUS SILICON CARBIDE.....	4
2.1 The structure of a-SiC _x :H.....	4
2.2 The density of states of a-SiC _x :H	7
2.2.1 Energy band of a-Si:H.....	7
2.2.2 Energy band of a-C:H.....	8
2.2.3 Energy band of a-SiC _x :H.....	11
2.3 Analysis of density of states distribution in the mobility gap.....	13
3. EQUIPMENTS AND THEIR IMPLEMENTATIONS.....	23
3.1 Aspects of plasma enhanced chemical vapor deposition technique	23
3.2 Plasma enhanced chemical vapor deposition system.....	26
3.3 Metallization system.....	29
3.4 Fourier transform infrared spectroscopy system.....	31
3.5 Ultraviolet-visible transmission spectroscopy system.....	32
3.6 Conductivity measurement system.....	33

4. SAMPLE PREPERATION.....	36
4.1 Substrate cleaning.....	36
4.2 Preparation of a-SiC _x :H films.....	37
4.2.1 Plasma reactions.....	37
4.2.1.1 Ethylene reactions.....	38
4.2.1.2 Silane reactions.....	40
4.2.1.3 Ethylene and silane mixture reactions.....	42
4.2.2 Deposition of a-SiC _x :H films by PECVD system.....	43
4.3 Metallization.....	44
5. X-RAY PHOTOELECTRON SPECTROSCOPY ANALYSIS OF a-SiC _x :H FILMS.....	46
6. THE OPTICAL CHARACTERISTICS OF a-SiC _x :H FILMS.....	54
6.1 Light absorption by thin films.....	54
6.2 Determination of optical energy band gap.....	59
6.3 Ultraviolet-visible spectroscopy analysis of a-SiC _x :H.....	62
7. VIBRATIONAL CHARACTERISTICS OF a-SiC _x :H FILMS.....	73
7.1 Molecular vibrations of a-SiC _x :H films.....	73
7.2 Fourier transform infrared spectroscopy analysis of a-SiC _x :H films.....	76
8. ELECTRICAL CHARACTERISTICS OF a-SiC _x :H FILMS.....	88
8.1 Conductivity in amorphous semiconductors.....	88
8.2 Electrical transport in extended states.....	89
8.3 Electrical transport by hopping mechanism.....	89
8.3.1 Variable range hopping.....	92
8.3.2 Nearest neighbor hopping.....	94
8.4 Electrical analysis of a-SiC _x :H films.....	104
9. CONCLUSIONS.....	110
REFERENCES.....	114
VITA.....	122

LIST OF TABLES

TABLES

4.1. Film deposition parameters.....	44
5.1. Elemental compositions of the LP a-S:H film (M=0) obtained from surface and bulk.....	49
5.2. Gas concentration and carbon contents of a-SiC _x :H films, obtained from UV-Visible spectroscopy analysis (Chapter 5) and XPS analysis, together. (XPS analysis of LP a-SiC _x :H with M=0.5 could not be performed.).....	49
5.3. The binding energies and bond types of peaks, corresponding the Si 2p and C 1s core levels.....	50
5.4. The gas concentrations and bonding compositions for a-SiC _x :H films. (XPS analysis of LP a-SiC _x :H with M=0.5 could not be performed.).....	52
6.1. Gas concentration and average thicknesses of a-SiC _x :H films deposited at lower (LP) (30 mW/cm ²) and higher (HP) (90 mW/cm ²) power densities.....	66
6.2 Table of optical constants and carbon content (x) of the films. The optical constants and carbon contents in literature are given as: x ^a (Mui, 1987), x ^b (Siebert, 1987), x ^c (Sitiropoulos, 1987), x ^d (Summonte, 2004), x ^e (Ambrosone, 2002, Sussman, 1981) and the carbon content obtained by XPS measurements are given as 'x (XPS)'. The average carbon	

content $\langle x \rangle$ of a-SiC _x :H films were determined by comparing the corresponding energy and refractive index values with the values given in the literature. Where σ is their standard deviations (Akaoglu et. al., 2006).....	67
7.1. The basic types of vibration and the special types of bending vibration.....	74
7.2. The possible geometric structures of ordinary and carbon rich a-SiC _x :H molecules.....	76
7.3. Absorption peaks of different molecular vibrational in FTIR spectra of a-SiC _x :H films.....	82

LIST OF FIGURES

FIGURES

2.1 σ bonded tetrahedral structure, with 109.5° angle between four atoms.....	5
2.2 a) The structure of sp^2 hybridized carbon atoms constituted of σ and π bonds. b) The structure of graphite.....	6
2.3 The structure of sp^1 hybridized carbons.....	6
2.4 Schematic diagram of the density of states in a-Si:H.....	7
2.5 Schematic electronic band structure of amorphous carbons.....	8
2.6 The planar orientation of a pair of sp^2 molecules, where ‘ ϕ ’ is the dihedral angle.....	9
2.7 π band DOS for compact clusters of fused 6-fold rings of increasing size (Robertson, 1986).....	11
2.8 The band tail variation of a-SiC _x and eventual defect levels (Robertson, 1992a) and schematic diagram of the DOS of a-SiC _x :H.....	12
2.9 Diagram of the potential well.....	15
2.10 Localization of discrete eigenvalues for odd solutions in square well. Rising curves represents $-\cot y$; falling curves are $\sqrt{\lambda - y^2}/y$ for different values of λ (Gasiorowicz, 1996).....	17
2.11 $(U(E)/V_0)^2$ versus (E/V_0) graph. (1) Fitting curve for 1 st region (Equation 2.24); (2) Fitting curve for 2 nd region (Equation 25); (3) Fitting curve for 3 rd region (Equation 2.26).....	19

2.12 Total number of DOS ($N(E)$) corresponding to various selections of potential well widths (a); $N(E_C)$ is set to $10^{22} \text{ cm}^{-3} \text{ eV}^{-1}$ in all cases.....	22
3.1 Schematic diagram of a capacitively coupled radio frequency discharge. Spatial distribution of the average potential between the electrodes is given just below the inter-electrode region, I_e and I_{ions} denote electron and ion currents, respectively (Atilgan, 1993).....	25
3.2 PECVD reactor.....	27
3.3 Gas delivery system.....	28
3.4 Schematic view of Univex450 model e-beam and magnetron sputtering system (Atilgan, 1993).....	30
3.5 Schematic view of metallization system.....	30
3.6 Fourier transform infrared spectroscopy system.....	31
3.7 UV-Visible transmission spectroscopy system.....	33
3.8 Room temperature conductivity measurement system.....	34
3.9 Temperature dependent dc conductivity measurement system.....	35
4.1 Metal electrodes were coated on the films on glass substrate for a) transverse, b) lateral conductivity measurements.....	45
4.2 Metal electrodes were coated on the films on crystalline substrate for transverse conductivity measurements.....	45
5.1 Photoemission process in XPS.....	47
5.2 XPS spectrum of LP a-SiC _x :H film with M=0.7 obtained from the surface and from the bulk.....	48
5.3 Deconvolutions of XPS Si 2p and C 1s peaks of LP a-SiC _x :H films for various gas concentrations. (XPS analysis of LP a-SiC _x :H film with M=0.5 could not be performed.).....	51
5.4 Deconvolutions of XPS Si 2p and C 1s peaks of HP a-SiC _x :H films for various gas concentrations.....	51
5.5 Percentage of bonding configurations as a function of gas concentration for LP and HP a-SiC _x :H films. Si-Si/Si/H (squares), Si-C (diamonds), C-C/C-H (triangles).....	53

6.1	Transmission and reflection of an electromagnetic field through a absorbing film on a transparent substrate of infinite thickness.....	54
6.2	Transmission and reflection through a transparent substrate.....	55
6.3	Transmission and reflection through an absorbing thin film on a transparent substrate of finite thickness.....	57
6.4	UV-Visible transmittance spectrum of ordinary glass substrate and a-SiC _x :H HP M=0.7 films deposited on ordinary glass substrates located at the center and at the edge of the bottom electrode of the PECVD reactor. The position of the substrates are illustrated in the inset where the circle represents the bottom electrode of the PECVD reactor.....	62
6.5	a) Refractive index as a function of wavelength, b) absorption coefficient as a function of energy for a-SiC _x :H HP M=0.7 films at the center and at the edge of the bottom electrode of PECVD reactor.....	63
6.6	(a) The deposition rates of a-SiC _x :H films along the radial direction of the bottom electrode grown with relative gas concentrations M=0.2 (squares), M=0.5 (triangles) and M=0.7 (diamonds). (b) The refractive indices (n), and (d) E ₀₄ values for the a-SiC _x :H films of M=0.7. Radial distances of about 0 cm and 12 cm correspond to the edge and the center of the electrode, respectively. Empty and full markers denote a-SiC _x :H films deposited at LP (30 mW/cm ²) and HP (90 mW/cm ²), respectively (Akaoglu et. al., 2006).....	64
6.7	The thickness obtained form optical characterization software (d _{fit}) is plotted as a function of the thickness obtained from envelop method (d _{env}). Empty and full markers denote a-SiC _x :H films deposited at LP (30 mW/cm ²) and HP (90 mW/cm ²), respectively (Akaoglu et. al., 2006).....	65
6.8	Deposition rate of a-SiC _x :H films as function of gas concentration, M (Akaoglu et. al., 2006).....	66
6.9	Carbon concentration (x) of a-SiC _x :H films as function of gas concentration M (Akaoglu et. al., 2006).....	69

6.10(a) Optical gaps E_g^{Tauc} , E_g^{Cody} and E_{04} , and as an inset, the slope parameters B^{Tauc} and B^{Cody} are plotted as function of carbon content (x) for a-SiC _x :H films at LP (empty markers) and HP (full markers) . (b) Urbach energies E_U are plotted as function of carbon content (x), for a-SiC _x :H films, together with suitable representative fittings. (Akaoglu et. al., 2006).....	71
7.1 Transmission and reflection of an electromagnetic field through an absorbing film on a transparent substrate of infinite thickness.....	78
7.2 The FTIR spectrum obtained from a-SiC _x :H HP M=0.7 film.....	80
7.3 First FTIR absorption band of a-SiC _x :H thin films deposited at lower (30 mW/cm ²) (LP) and higher power densities (90 mW/cm ²) (HP) with deconvolutions of the peaks according to the assignments given in Table 7.3 (Akaoglu et. al., 2006).....	81
7.4 Second (a) and third (b) FTIR absorption band of a-SiC _x :H thin films deposited at lower (30 mW/cm ²) (LP) and higher power densities (90 mW/cm ²) (HP) with deconvolutions of the peaks according to the assignments given in Table 7.3 (Akaoglu et. al., 2006).....	81
7.5 (a) Concentration of the vibration mode and (b) FWHM of the absorption peak, at 770 cm ⁻¹ are plotted as a function of carbon content (x). Empty markers denote LP films and and full markers denote HP films (Akaoglu et. al., 2006).....	83
7.6 The sum of concentrations of the vibrational modes at about 640 cm ⁻¹ and 670 cm ⁻¹ is plotted, as a function of carbon content (x). Empty markers denote LP films and and full markers denote HP films (Akaoglu et. al., 2006).....	84
7.7 Carbon content influence on the sum of concentrations of wagging and stretching vibration modes of Si-H _n bonds. Empty markers denote LP films and full markers denote HP films (Akaoglu et. al., 2006).....	85

7.8 Peak position of Si-H stretching mode at 2090 cm^{-1} is plotted, as a function of carbon content (x). Empty markers denote LP films and full markers denote HP films (Akaoglu et. al., 2006).....	86
7.9 The sum of the relative concentrations of symmetric and asymmetric stretching modes of (a) C-H ₂ and (b) C-H ₃ bonds plotted as a function of carbon content (x). Empty markers denote LP films and full markers denote HP films (Akaoglu et. al., 2006).....	87
8.1 DOS distribution in the mobility gap of amorphous semiconductors.....	94
8.2 Differential hopping conductivity plotted for various values of a) temperatures; b) E_0 ; c) a; and d) $N(E_C)$, by considering the 1 st and the 2 nd regions together (a1, b1, c1, d1) and by considering only the 2 nd region (a2, b2, c2, d2). For each graph fixed parameters are taken as $\omega_{ph}=10^{12}\text{ s}^{-1}$, $E_F=1\text{ eV}$, $a=5\text{ nm}$, $T=300^\circ\text{K}$, $E_0=0.3\text{ eV}$ and $N(E_C)=10^{22}\text{ cm}^{-3}\text{eV}^{-1}$...	101
8.3 Hopping conductivity plotted for various values of a) temperatures; b) E_0 ; c) a; and d) $N(E_C)$ by assuming equation 8.44 and 8.45 (a1, b1, c1), together and assuming only equation 8.44 (a2, b2, c2). For each graph fixed parameters are taken as $\omega_{ph}=10^{12}\text{ s}^{-1}$, $E_F=1\text{ eV}$, $a=5\text{ nm}$, $E_0=0.3\text{ eV}$ and $N(E_C)=10^{22}\text{ cm}^{-3}\text{eV}^{-1}$	103
8.4 Schematic diagram of sample prepared for conductivity measurements...	104
8.5 Room temperature dc conductivity measurements of HP and LP a-SiC _x :H films, are plotted as a function of carbon content (x). Ohmic trend is shown by solid line.....	104
8.6 Room temperature dc conductivities of HP and LP a-SiC _x :H films are plotted as a function of carbon content (x).....	105
8.7 Conductivity of HP and LP a-SiC _x :H films are plotted as a function of inverse temperature.....	106
8.8 Activation energies of a-SiC _x :H films obtained for only standard transport model case (LP1 and HP1) and for both standard model and hopping mechanism case (LP2 and HP2) are plotted as a function of	

carbon content (x). Where Hp denotes higher (90 mW/cm ²), and LP denotes lower (30 mW/cm ²) power densities.....	107
8.9 Disorder parameters obtained for the hopping conduction mechanism for a-SiC _x :H films, deposited at higher (90 mW/cm ²) (HP), and lower (30 mW/cm ²) (LP) power densities are plotted as a function of carbon content (x).....	108
8.10 Hopping conduction percentage among the overall conduction of a-SiC _x :H films, deposited at higher (90 mW/cm ²) (HP), and lower (30 mW/cm ²) (LP) power densities are plotted as a function of carbon content (x).....	109

CHAPTER 1

INTRODUCTION

The hardware of modern information system can be divided into two categories: Electronic processors (microelectronics) and input/output devices. The improvement of processors has been associated with continuous miniaturization on crystalline silicon chips. Therefore integrated circuit technology develops as electronic processors with gradually reducing device dimensions below micrometer (Submicron). On the other hand, input/output devices have to continue to be of large dimensions, i.e. electronic displays, printers, keyboards or document scanners require electronics technology with large formats, which is called large area electronics. Each of these applications requires an electronic device, whose size matches the interface with human activity – either a display screen or a sheet of paper- with typical dimensions of 25 cm or larger. Therefore, economic fabrication of large area electronic devices requires homogeneous materials with larger size. These sort of large area semiconductor materials, at reasonable cost, are only achievable by thin film technologies on low cost substrate (Such as ordinary glass plates). Thus, whereas crystalline silicon is the material of choice for integrated circuits, its poor optical properties and high costs makes it unsuitable for making large displays. The solutions developed on the semiconductors other than the crystalline silicon have created mismatching problems with the existing silicon based microelectronic technologies. On the other hand, hydrogenated amorphous silicon (a-Si:H) and its

alloys could be selectively doped both n and p types leading to various devices such as p-n, p-i-n, Schottky diodes etc... Additionally, they could be deposited at low temperatures by the glow discharge method at reasonable cost as large area thin films on low cost substrates. In this respect, a-Si:H and its alloys are gaining increasing use in large area arrays of electronic devices, as they meet these requirements.

Among the other amorphous silicon alloys, hydrogenated amorphous silicon carbide (a-SiC_x:H) has been extensively studied, because of its usefulness as an important technological material, which its optical, electrical and mechanical properties can be modified by changing the relative composition of the individual elements, Si and C. At one end of the spectrum (x=0), hydrogenated amorphous silicon (a-Si:H) is a semiconductor with an optical band gap of approximately 1.75 eV, while at the opposite end (x=1) hydrogenated amorphous carbon (a-C:H) is an insulator with a gap as large as 4 eV. Between these two extremes, the band gap can be systematically controlled in order to provide materials with desired properties. In this respect, the optical gap of a-SiC_x:H covers the visible region of the spectrum. Therefore a-SiC_x:H is highly suitable for fabrication of large area flat panel displays, which have significant importance in commercial monitors (Kanicki, 1991, Tean, 1994, Jong, 1996, Kuhman et. al. 1989).

In second chapter, the structure of a-SiC_x:H is theoretically revised. For the films, the bonding organization changes drastically from pure a-Si:H, x=0, to pure a-C:H, (x=1). In this respect, the characteristics of DOS distribution are investigated by reviewing the corresponding characteristics of a-Si:H and hydrogenated amorphous carbon (a-C:H). In the light of defect pool model, the DOS distribution in the mobility gap is investigated.

In the third chapter, firstly, the film deposition and metallization systems such as plasma enhanced chemical vapor deposition system (PECVD) and e-beam and sputtering system and then, the experimental systems such as, ultraviolet-visible spectroscopy (UV-Visible), Fourier transform infrared spectroscopy (FTIR), and conductivity systems are outlined.

In the fourth chapter, the deposition procedure of films with various gas concentrations at two different, lower (30 mW/cm^2) and higher (90 mW/cm^2), r.f. power densities by PECVD system is outlined. The aspects of PECVD system and dissociation of plasma gases are revised.

In the fifth chapter, elemental composition of the $\text{a-SiC}_x\text{H}$ films and relative composition of existing bond types, which are analyzed by XPS measurements, are reported.

In the sixth chapter, thicknesses, deposition rates, refractive indices and optical band gaps of the films are determined by UV-Visible transmittance measurements. Uniformity of the deposited films are analyzed along the radial direction of the PECVD reactor. The carbon contents of the films are determined by comparing the optical gaps and refractive indices separately, with the values published in the literature.

In the seven chapter, vibrational characteristics of the $\text{a-SiC}_x\text{H}$ films are reviewed and analyzed by FTIR measurements.

Finally, in the eight chapter, electrical characteristics of the films are analyzed by dc conductivity measurements performed both at room temperature and in the temperature range of 250 K° to 450 K° . The conduction mechanisms, such as extended state, nearest neighbor and variable range hopping in tail states are revised. Variable range hopping conductivities are analyzed by considering the DOS distribution in various regions of mobility gap. The activation energies are determined by firstly considering only extended state conduction and next by considering both extended state and hopping conduction. Finally, as a result of considering hopping conduction, besides extended state conduction, an increase in the activation energies is observed especially for HP films.

CHAPTER 2

THE CHARACTERISTICS OF HYDROGENATED AMORPHOUS SILICON CARBIDE

2.1 THE STRUCTURE OF a-SiC_x:H

a-SiC_x:H consists of three different atoms, silicon, carbon and hydrogen. These three different atoms, having unique and different properties, change the characteristics of the resultant a-SiC_x:H by a correlation in the balance of the concentrations of them in the material.

The bonding organization, affecting the structure of the films, changes drastically from $x=0$, pure a-Si:H, to $x=1$, pure a-C:H. For $x<0.5$, both Si-Si homonuclear bonds and Si-C heteronuclear bonds, for $x\approx 0.5$ Si-C heteronuclear bonds and finally for $x>0.5$ Si-C heteronuclear bonds and various types of C-C homonuclear bonds are expected. Therefore $x<0.5$ region of a-SiC_x:H has an a-Si:H dominant character, whereas $x>0.5$ has an a-C:H dominant character. The intermediate values, $x\approx 0.5$, show a mixed character of these two regions. As a result, the properties of both a-Si:H and a-C:H must be examined separately, in order to understand the properties of a-SiC_x:H (Robertson, 1986, 1987, 1991, 1992a, 1992b).

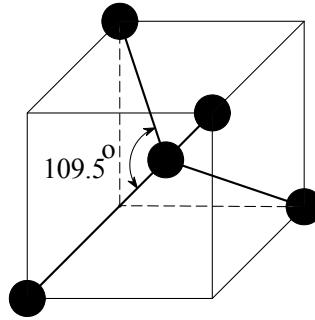


Figure 2.1 σ bonded tetrahedral structure, with 109.5° angle between four atoms.

Si rich $a\text{-SiC}_x\text{:H}$ ($x < 0.5$) is mainly composed of σ bonded tetrahedral structure, with 109.5° angle between four atoms like $a\text{-Si:H}$ structure, as shown in Figure 2.1 (Street, 1991). On the other hand, the structure of carbon rich $a\text{-SiC}_x\text{:H}$ has many different properties. In order to understand the nature of $a\text{-SiC}_x\text{:H}$ at rich carbon concentration, the properties of $a\text{-C:H}$ must be reviewed (Robertson, 1986, 1987, 1991, 1992a, 1992b).

Carbon atom has four valence electrons, enabling carbon to form sp^3 , sp^2 and sp^1 hybridization. The sp^3 hybridization of carbon atoms, similar to silicon atoms, form σ bonded tetrahedral structure (Figure 2.1). In the sp^2 hybridization, atoms bond to three neighboring atoms, forming a planar structure with an angle of 120° . The bonds between the atoms in planar structure are two types as shown in Figure 2.2.a. The first one is the σ type, which forms the skeleton of the amorphous network. σ bonds are common for both sp^3 and sp^2 hybridization. The second type π bond is generated from unhybridized or delocalized p_z orbitals. The π orbitals are present only in the sp^2 and sp^1 hybridized atoms. The planar structure of sp^2 hybrid orbitals favors the formation of hexagonal rings (Aromatic structure) to optimize the interactions between the unhybridized p_z orbitals (The six p_z orbitals in these rings of hexagonal structure combine by producing π bonds). These six electrons belong to the structure as a hole, in other words, they are delocalized in the π orbitals. The hexagonal rings continuously combine, forming planes on one another whose stacking sequence is ABA. The planes of

hexagonal rings are held together by weak Van Der Waals interaction between the π bonded electrons, forming the graphitic structure (Figure 2.2.b).

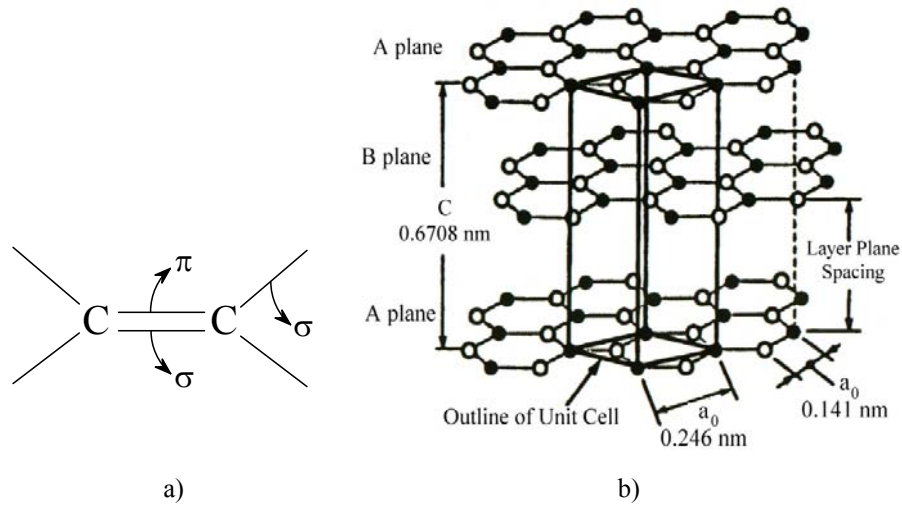


Figure 2.2 a) The structure of sp^2 hybridized carbon atoms constituted of σ and π bonds. b) The structure of graphite.

The sp^1 hybridized carbons form linear structures with triple bonds (Olefinic structure). Two carbon atoms bond to each other by one σ bond and two π bonds. One of the π bonds is in the z- plane and the other one is in the y-plane, whereas the σ bond is in the x-plane (Figure 2.3).

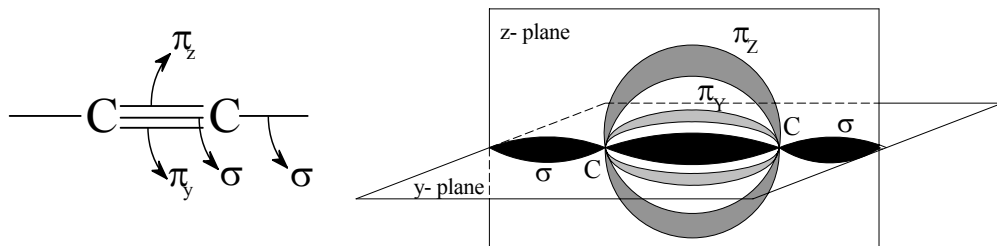


Figure 2.3. The structure of sp^1 hybridized carbons.

2.2 THE DENSITY OF STATES OF a-SiC_x:H

The structural diversity of the a-SiC_x:H films, by the change in the carbon content, also impinges on energy band. Consequently, the characteristics of the energy band of a-SiC_x:H could be investigated better by reviewing the corresponding characteristics of a-Si:H and a-C:H.

2.2.1 ENERGY BAND OF a-Si:H

The extended states of conduction and valence bands of a-Si:H are followed by the localized states called band tails as shown in Figure 2.4. The tail states are caused by the fluctuations of the bond lengths and bond angles in the continuous and disordered structure of amorphous material. In the interval of these bands, there are deep states due to dangling bonds in the structure.

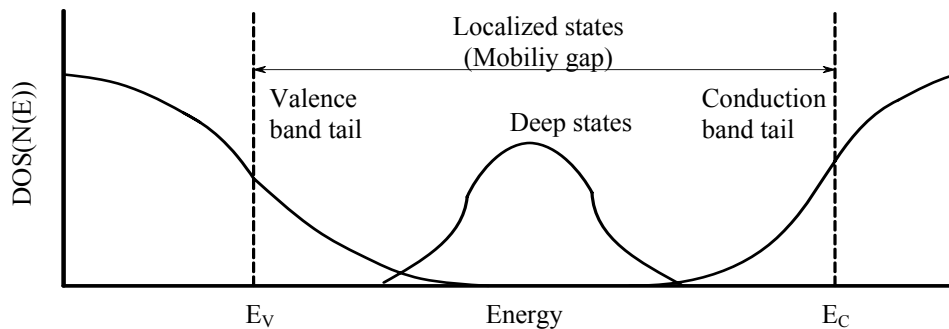


Figure 2.4. Schematic diagram of the density of states in a-Si:H.

The chemical forces between atoms tend to optimize both the bond lengths and bond angles, since each atom is free to be relaxed in three dimensions. These optimizations create modified band states, which are generated by weak bonds (WB). Therefore, the states can be divided into localized and extended variants. Charge carriers in localized states have very low mobility, whereas the extended states provide much higher mobility to carriers and are separated from localized states by a conceptual mobility gap. These

strains lead also to gross structural features, such as cracks or voids and hence create coordination defects. Apart from tail states, deep states may arise from coordination defects, which are dangling bonds (DB), or abnormally bounded configurations. As their energies are much deeper than weak bonds, they cause a distribution of relatively high density of deep states, located around the midgap. In order to have a functional optoelectronic material, these localized states must be reduced. In this respect, hydrogenation is inevitable. Hydrogenation firstly reduces the density of dangling bonds by saturating these bonds. Secondly, it increases the band gap of the material, because hydrogen is more electronegative than silicon and hence Si-H bonding states are relatively deep in the a-Si:H valence band (Street, 1991).

2.2.2 ENERGY BAND OF a-C:H

The energy band gap of a-C:H possesses a different DOS distribution with respect to a:Si:H. The structure of the a-C:H, being tetrahedral (sp^3), aromatic (sp^2) and olefinic (sp^1), strongly influences the DOS distribution by the effect of relevant π bonds. For tetrahedral a-C:H structure (sp^3), σ (bonding) states exist at valence band and σ^* (anti-bonding) states exist at conduction band. Whereas, for aromatic and olefinic π (bonding) and π^* (anti-bonding) bonds are located between the σ and σ^* states, as shown in Figure 2.5. Consequently, they mainly determine the electronic and optical properties of the material (Robertson, 1986, 1987, 1991, 1992a, 1992b).

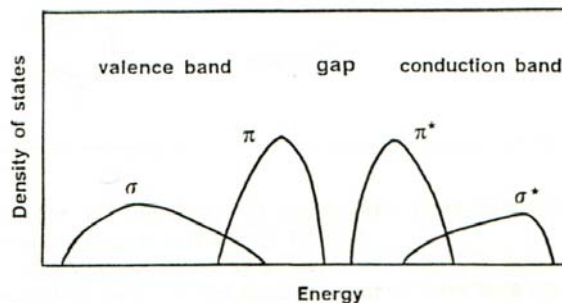


Figure 2.5. Schematic electronic band structure of amorphous carbons.

The energetics of π states can be investigated by Hückel model. In this model, the Hamiltonian (H) of the valence electrons is simplified by the assumptions that, first, σ and π state energies (H_σ and H_π) can be treated independent from each other.

$$H = H_\sigma + H_\pi + H_{\sigma\pi} \quad (2.1)$$

Additionally, the energy of the decoupling of the σ states from π states ($H_{\sigma\pi}$) goes to zero, due to the minimization of the interaction between these states by the local perpendicular configuration of π and σ planes (Figure.2.6.).

$$H_{\sigma\pi} \approx 0 \quad (2.2)$$

As a result of these assumptions, the problem is reduced to a system of p_z orbitals, which is a one-electron atomic orbital model, where only nearest-neighbor interaction energy is considered.

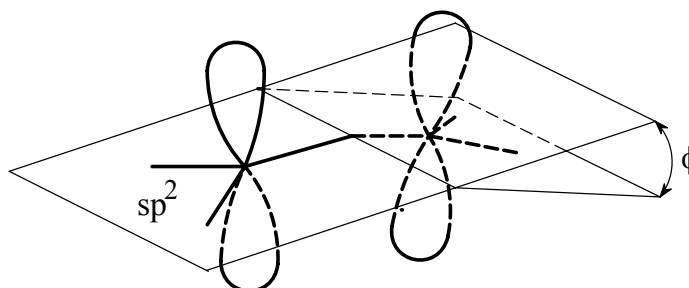


Figure 2.6. The planar orientation of a pair of sp^2 molecules, where ' ϕ ' is the dihedral angle.

The simplest cluster of sp^2 hybridized atoms is a pair of adjacent π sites, seen in Figure 2.6. For this cluster one bonding (occupied) π and one anti-bonding (empty) π^* sites are present.

$$E_b = -\beta \cos \phi \quad (2.3)$$

$$E_{ab} = +\beta \cos \phi \quad (2.4)$$

where E_b is the energy for bonding π state, E_{ab} is the energy for π^* state, ϕ is the dihedral angle and β is the energy for the case when ϕ is 0° . In order to maximize the interaction of adjacent orbitals and minimize the total energy, the dihedral angle must approach to zero and the orbitals must orient themselves in a parallel arrangement. These conditions are important to understand the stability of the hybrid carbon atoms. As a result, the energy of gap is maximized tending to a more stable structure.

Generally, for isolated regular and planar rings with N vertices of aromatic structures, the energy eigenvalues (E_n) are given by (Robertson, 1986)

$$E_n = 2\beta \cos\left(\frac{2\pi n}{N}\right), \quad (2.5)$$

In the equation 2.5, $N=3$ and $N=4$ are ignored, because they distort the σ backbone too much to be structurally stable. Only $N=6$, with levels distributed symmetrically around Fermi energy ($E_F=0$), produces a stable structure. The olefinic structure has 6 π electrons and the energy per site for this formation is equal to $6\beta/6=\beta$. In the aromatic structure the energy per site is $8\beta/6=1.33\beta$. This states that, formation of 6 fold rings results in a more stable structure. This stability is called as aromatic stability. Resultantly, six fold rings are favored and more probable. When the cluster size increases by addition of new rings, the binding energy of the π electrons per site increases, forming more stable structures, such as graphite, which is formed by respectively infinite number of six-fold rings. The DOS of finite layers of fused benzene rings are given in the Figure 2.7. (Robertson, 1986). For number of rings greater than 18, DOS resembles that of the graphite, which has no energy gap. On the other hand, experiments have carried out that a-C:H have an optical gap between 1.6-2.7 eV. In order to have an optical energy gap, the a-C:H film should not be continuously

sp^2 like bonded and it must be built by random distribution of medium sized sp^2 bonded islands, separated from each other by sp^3 dominant boundaries. This carries out the importance of size effect of aromatic clusters on the existence of the energy gap.

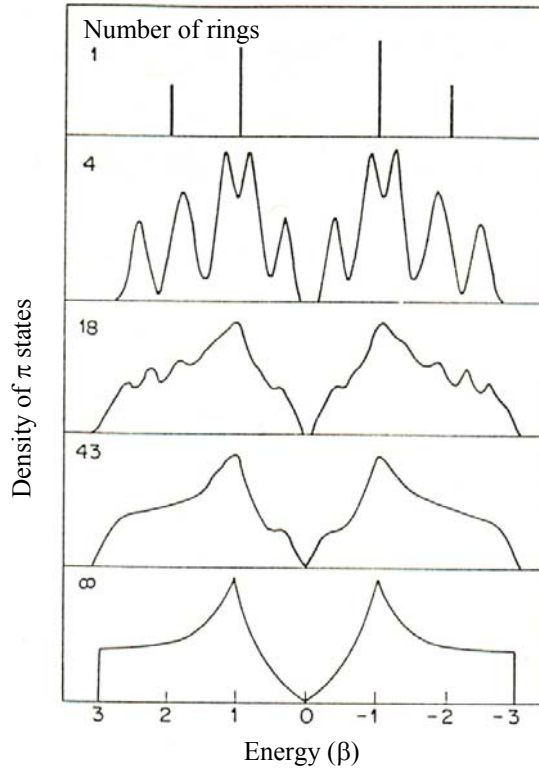


Figure 2.7. π band DOS for compact clusters of fused 6-fold rings of increasing size (Robertson, 1986).

2.2.3 ENERGY BAND OF $a\text{-SiC}_x\text{:H}$

The energy band gap structure of $a\text{-SiC}_x\text{:H}$ can be understood more easily and properly by combining the special characteristics of both $a\text{-Si:H}$ and $a\text{-C:H}$. The characteristics of $a\text{-Si:H}$ becomes dominant at values $x < 0.5$, and similarly the characteristics of $a\text{-C:H}$ become dominant at values $x > 0.5$. The electrical characteristics change from that of the tetrahedral structure (sp^3) of $a\text{-Si:H}$ to that of the clustered aromatic structure (sp^2) of carbon, as the carbon concentration increases.

In the silicon rich region sp^3 type Si-Si bonds exist. If carbon is introduced into the film, with small concentration ratio, more stronger sp^3 type σ Si-C bonds are formed, which eventually increase the energy gap (Figure 2.8). The carbon atoms affect the valence band more than the conduction band, because energy level of Si-C lies deep in the valence band. Therefore, valence band edge moves towards lower energies, but steps more smoothly than that of the conduction band. Higher amounts of carbon start to form π bonds between themselves. Thus, the energy band gap exhibits a maximum around $x \approx 0.6$, where σ and π -like band edges cross each other, shown in the Figure 2.8. After the ratio $x > 0.6$, the energy band gap starts to decrease (Robertson, 1992a, 1992b).

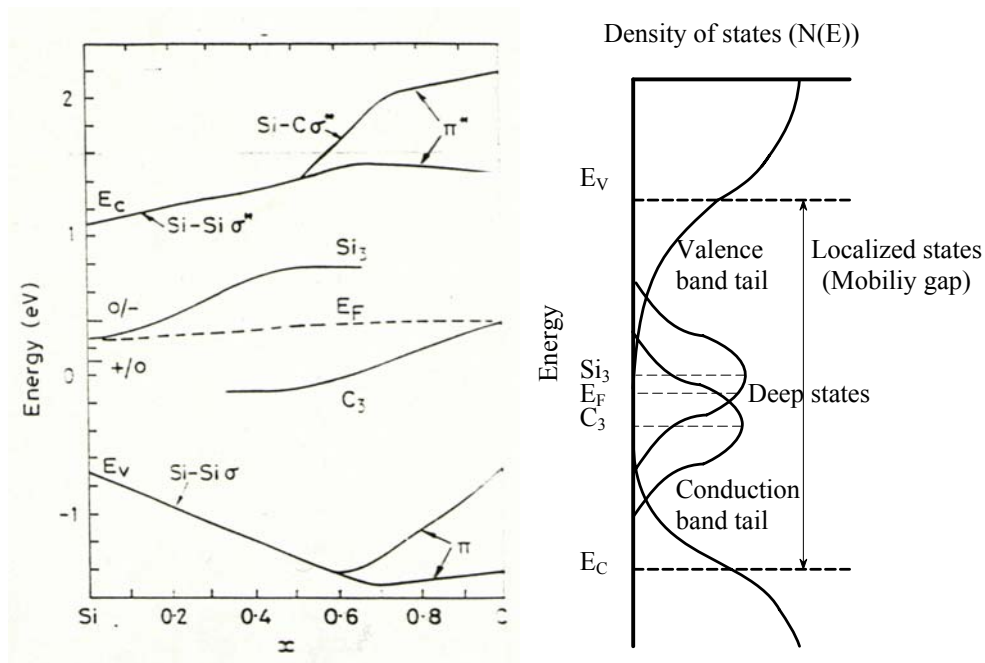


Figure 2.8. The band tail variation of a-SiC_x and eventual defect levels (Robertson, 1992a) and schematic diagram of the DOS of a-SiC_x:H.

The defects in the a-SiC_x:H can also be characterized better by examining the defects of intrinsic a-Si:H and a-C:H. The σ type dangling bond defects generally exist in the sp^3 hybridized SiC. The defects are categorized as; defects of Si dominant and C dominant regions and represented by the symbols Si₃ and

C_3 respectively shown in Figure 2.8. Since, C is more electronegative than Si, energy of the C_3 defects is deeper than that of the S_3 defects. Because of this, the charge transfer from Si_3 to C_3 occurs in a way that defects changes their charge states to Si_3^+ and C_3^- . The π defects occur at the odd-member clusters or at the boundary of the π bonded clusters in the C dominant region (Katircioğlu, 2004).

2.3 ANALYSIS OF DENSITY OF STATES DISTRIBUTION IN THE MOBILITY GAP

For ideal crystal structure, the three components of the quasimomenta as quantum numbers determine the electronic state on the form of Bloch function, which is obtained from the Schrodinger equation (Schiff, 1968, Katircioğlu, 2004).

$$\Psi(r) = U_k(r) e^{ikr} \quad (2.6)$$

$\Psi(r)$ is extended throughout the crystal, possessing perfect phase coherence, which means that the phase at a given point may be determined at any other point in the crystal provided that the wavevector 'k' is known. But, in real crystal, due to phonon/impurity scattering phenomena a finite mean free path or coherence length 'L' is established. If each scattering is weak, the wavevector or quasimomentum remains as a good quantum number. Since $\Delta k/k \ll 1$, the surface of constant energy is almost spherical and then $E(k) = \hbar^2 k^2 / 2m^*$ is valid. If each scattering is strong, translational and orientational long range order is lost and some sort of disorder dominates, which is the situation of amorphous structures. The effect of the disorder on the band width (B) and coherence length (L) could be outlined by the Anderson localization model (Overhof, 1989). The non-periodic potential of the disordered material is derived from the crystal structure by random displacement of each atom by a random amount and the addition of a random potential energy $V_0/2$ to each well such that the energy of the electron

inside becomes $E+V_0/2$. As the disorder further increases, the coherence length (L) becomes meaningless ($L \ll a$) and the wavefunction becomes localized. The exponentially decaying rate depends on the magnitude of disorder V_0 . For this case, the quasimomentum is undefined and as a result $E(k)$ can not be constructed. As $\Delta k_x = 2\pi/L$, the minimum value of L (interatomic distance 'a', since $\Delta k/k > 1$ is meaningless), causes $\Delta k_x = 2\pi/a \approx k$ and resultantly, $\Delta k/k$ becomes nearly equal to 1. In other words, for the amorphous structure, which is based on long range disorder, more or less short range order and coordination defects, k is not a good quantum number and instead of k , density of states (DOS), which is an isotropic quantity, could be used (Mott, 1969, 1979).

The localized DOS distribution for amorphous semiconductor structures could be formalized in the following way by the defect pool model (Street, 1991). The majority of states within a band possess extended wave functions although their phase coherence lengths are relatively very short. Beyond a limit, this distortion, around a site at the average position 'R', leads to a local trapping potential $V(R-r)$, which in its turn localizes one of the band energy level E (where 'r' denotes the localization of the defect). In this respect, the total number of states remaining conserved, the band tail may be broadened more or less on either site, depending on the strength of the local perturbations. The overall amount of V , reflecting the strength of the local distortion, is related to the defect formation energy such that larger defect formation energy decreases the thermodynamic existence probability of this defect. Taking into account the independence and randomness of each local potential, the probability of occurrence of a local potential V is reasonably expected to be a one sided Gaussian relation (Economou, 1987, O'Leary, 1997, Bacalis, 1988, Tanaka, 1999, John, 1986, O'Leary, 1995).

$$P(V) = \frac{1}{\sqrt{\pi E_0}} \exp\left(-\frac{V^2}{E_0}\right) \quad (2.7)$$

where $P(V)$ gives the probability of occurrence of a local potential (V) and E_0 is the standard deviation from the mean value (Disorder parameter). In this respect, E_0 may be taken as a degree of average distortion or disorder parameter. In equation 2.7, the band edge is taken as reference level and resultantly equal to zero.

The effective extension of each local potential should remain within about the interatomic distance, at least the core effect of the distortion might be expected to be very narrow. In this respect, the effective mass and the dielectric constant of the medium could not be used for these atomic ranges. Although a spherical symmetry of the local distortion being not irrefutable, here for a first insight, a spherical square well may be assumed. Therefore, bound states in a potential well can be defined by:

$$V(r-R) = -U \quad \text{for} \quad r-R < a \quad \text{with} \quad U > 0 \quad (2.8)$$

$$V(r-R) = 0 \quad \text{for} \quad r-R > a \quad (2.9)$$

where ‘ U ’ denotes the well depth, ‘ a ’ being the well radius (Figure 2.9).

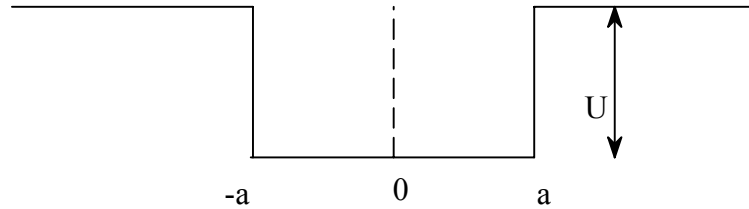


Figure 2.9. Diagram of the potential well.

The solutions outside the well, that are bounded at infinity are:

$$v(x) = C_1 \exp(\kappa(r-R)) \quad r-R < -a \quad (2.10)$$

$$v(x) = C_2 \exp(-\kappa(r-R)) \quad r-R > a \quad (2.11)$$

where

$$\kappa = -\sqrt{\frac{2m^*E}{\hbar^2}}$$

Since dealing with real functions, it is more convenient to write the solution inside the well in the form:

$$u(x) = A\cos q(r-R) + B\sin q(r-R) \quad (2.12)$$

where

$$q = \sqrt{\frac{2m^*}{\hbar^2}(U - |E|)} > 0$$

Matching these solutions and derivatives at the edges ($r-R=-a$ and $r-R=a$) yields:

$$\kappa = -q \cot qa \quad (\text{odd solution. Figure 2.10}) \quad (2.13)$$

$$\kappa = q \tan qa \quad (\text{even solution}) \quad (2.14)$$

Substituting $\lambda = \frac{2m^*Ua^2}{\hbar^2}$ and $y = qa$ into equations 2.13 and 2.14, the solutions

become:

$$\frac{\sqrt{\lambda - y^2}}{y} = -\cot y \quad (\text{odd solution}) \quad (2.15)$$

$$\frac{\sqrt{\lambda - y^2}}{y} = \tan y \quad (\text{even solution}) \quad (2.16)$$

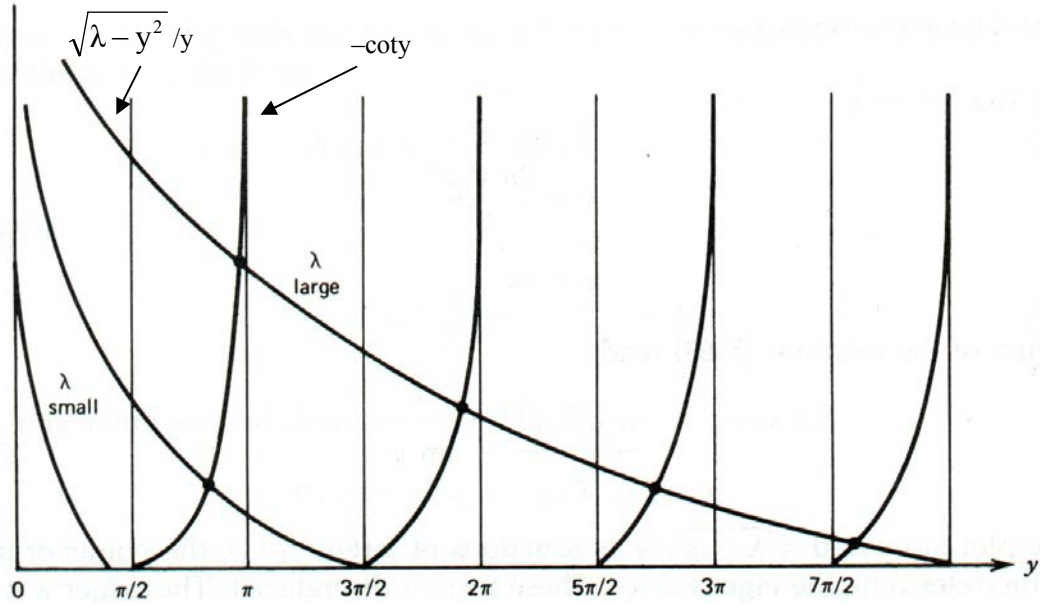


Figure 2.10. Localization of discrete eigenvalues for odd solutions in square well. Rising curves represents $-\cot y$; falling curves are $\sqrt{\lambda - y^2}/y$ for different values of λ (Gasiorowicz, 1996).

The solutions of the set can be obtained by graphical intersection of right handside and left hand side of the expressions in terms of y , depicted in Figure 2.10. The points of the intersection determine the eigenvalues (Figure 2.10), forming a discrete solution set. The larger λ is, the further the curves for $\sqrt{\lambda - y^2}/y$ go, that is, when the potential is deeper and/or broader, there are more bound states.

$$y \approx n\pi \quad (\text{odd solution}) \quad n=1,2,3,\dots \quad (2.17)$$

$$y \approx (n + \frac{1}{2})\pi \quad (\text{even solution}) \quad n=0,1,2,3,\dots \quad (2.18)$$

For odd solution, there will be an intersection if $\sqrt{\lambda - \frac{\pi^2}{4}} > 0$. That is:

$$\frac{2m^* U a^2}{\hbar^2} \geq \frac{\pi^2}{4} \Rightarrow V_0 \approx \frac{\pi^2 \hbar^2}{8m^* a^2} \quad (2.19)$$

Consequently, for any potential well shallower than V_0 , there will be no solution; no electron will be trapped in the well. On the other hand, for even solutions (equations 2.16 and 2.18), there will always be a bound state. Since, the condition $\psi(0)=0$ is imposed on the wave functions in the three dimensional systems, the odd solutions (equations 2.15 and 2.17), all vanish at the origin ($x=0$), will be used in the spherical square potential well systems; (Gasirowicz, 1996).

The numerical or graphical solutions of the well with potential U , can be determined (Katircioğlu, 2004):

For	$0 < U < V_0$: There is no solution
	$V_0 < U < 9V_0$: There is 1 bound state (E)
	$9V_0 < U < 25V_0$: There are 2 bound states (E, E')
	$(2n-1)^2V_0 < U < (2n+1)^2V_0$: There are n bound states (E, E', ..., E ⁽ⁿ⁺¹⁾)

Realistically, the eventual excited states could not be kept as true binding states, as a result, only fundamental state (one bound state) may be reasonably considered. In the light of these, to determine $U(E)$, the ground state energy level E , corresponding to an abrupt spherical potential well of depth V and radius a , must be solved. This can be achieved by solving the roots of equation 2.15 and dividing by V_0 ;

$$\frac{\sqrt{\lambda - y^2}}{y} = -\cot y \Rightarrow -\sqrt{\frac{U-E}{E}} = \tan \left[a \sqrt{\frac{2m^*}{\hbar^2} (U-E)} \right] \quad (2.20)$$

Dividing both sides of equation 2.20. by V_0 gives:

$$-\sqrt{\frac{\omega - f}{f}} = \tan \left[\frac{\pi}{2} \sqrt{(\omega - f)} \right] \quad (2.21)$$

where $\omega = U/V_0$ and $f = E/V_0$.

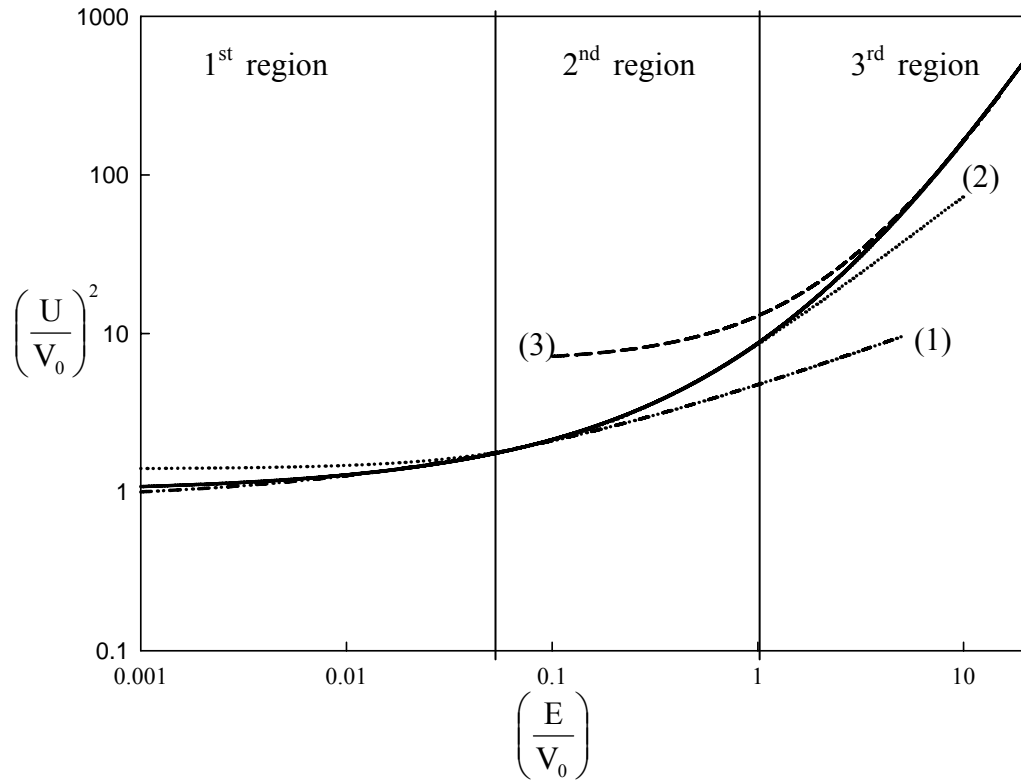


Figure 2.11. $(U(E)/V_0)^2$ versus (E/V_0) graph. (1) Fitting curve for 1st region (Equation 2.24); (2) Fitting curve for 2nd region (Equation 25); (3) Fitting curve for 3rd region (Equation 2.26).

The functional dependence of U on E is evaluated by numerical solution and seen to exhibit different regions, as E is increased (Figure 2.11). The numerical solution approximation points out three main regions where simple analytic solutions can be obtained for $U(E)^2$ vs. E curve (Figure 2.11.) (O'Leary, 1997, Bacalis, 1988, Tanaka, 1999, John, 1986, O'Leary, 1995, Baldereschi, 1973, Baldereschi, 1974, Schiff, 1968):

a) 1st region: Shallow binding energy for $\frac{|E|}{V_0} < E_1 = 0.08$.

$$U^2 \approx V_0^2 \left[A + B \sqrt{\frac{|E|}{V_0}} \right], \text{ where } A=0.68 \text{ and } B=5 \text{ are constants.} \quad (2.22)$$

b) 2nd region: Intermediate binding energy for $E_1 < \frac{|E|}{V_0} < E_2 = 1$.

$$U^2 \approx V_0^2 C|E| + D, \quad \text{where } C=6.19 \text{ and } D=1.4 \text{ are constants.} \quad (2.23)$$

c) 3rd region: Deep binding energy for $E_2=1 < \frac{|E|}{V_0}$.

$$U \approx F|E| - GV_0, \quad \text{where } F=1.1 \text{ and } G=1.96 \text{ are constants.} \quad (2.24)$$

The one electron potentials as being composed of an ensemble of potential wells, represents the various forms of potential wells. Within the framework of a potential well model, these various forms of local disorder are represented by potential wells of different sizes, shapes and depths. By determining the binding energy corresponding to each potential well and then averaging over the ensemble of the wells, the number of localized DOS ($N(E)$) can be obtained (Equation 2.25). For this purpose, first it is assumed that, these wells are uniformly distributed throughout an otherwise perfect solid, second the possibility of well overlap is ignored and third the depth of each well is independently selected from the ensemble of possible well depths. Additionally, the higher order states are also ignored, as they would require considerably deeper and less probable wells. As a result, the number of localized DOS in the energy interval between E and $E+dE$ takes the form (Economou, 1987, O'Leary, 1997, Bacalis, 1988, Tanaka, 1999, John, 1986, O'Leary, 1995):

$$N(E)dE = 2N_L P(U)dU \quad (2.25)$$

where N_L is the total number of local trapping potential sites per unit volume and $P(U)dU$ representing the probability of states, whose energy is between U and $U+dU$. 2 represents the the spin factor.

$N(E)$ for the shallow binding energy region (1st region) is determined by using equation 2.22:

$$N(E)_{1^{\text{st}} \text{ region}} \approx N_L \frac{1}{\sqrt{E}} \exp\left(-\frac{B\sqrt{E}V_0^{3/2}}{E_0}\right) \quad (2.26)$$

The square root functional dependence of energy arises as a result of subtle relationship between well depth, binding energy and well extend of the loosely bound states. Here, DOS at the band edge ($N(E_C)$), is approximated ($10^{22} \text{ cm}^{-3} \text{ eV}^{-1}$) being equal to $N_L/\sqrt{0.001}$.

For the intermediate binding energy region (2nd region), DOS is determined by using equation 2.23:

$$N(E)_{2^{\text{nd}} \text{ region}} \approx N(E_1)_{1^{\text{st}} \text{ region}} \exp\left(-\frac{CEV_0}{E_0}\right) \quad (2.27)$$

Finally, for the deep binding energy region, total number of DOS is determined by using equation 2.24:

$$N(E)_{3^{\text{rd}} \text{ region}} \approx N(E_2)_{2^{\text{nd}} \text{ region}} \exp\left(-\frac{FE^2V_0^2}{E_0}\right) \quad (2.28)$$

In this approximation, in the calculation of total number of DOS, the third region is ignored, as it would require considerably deeper and less probable wells,

In the Figure 2.12, $N(E)$ versus energy is graphed for various potential well depths (a). A substantial enhancement in the number of tail states is observed as ‘a’ is increased. This is probably because of the increased probability of binding. In all cases, a divergence is observed as $E \rightarrow 0$, due to the $1/\sqrt{E}$ pre-exponential factor in equation 2.26. The semiclassical limit places an upper bound on these trends because as ‘a’ goes to infinity, probability of binding goes to 1 (O’Leary, 1997).

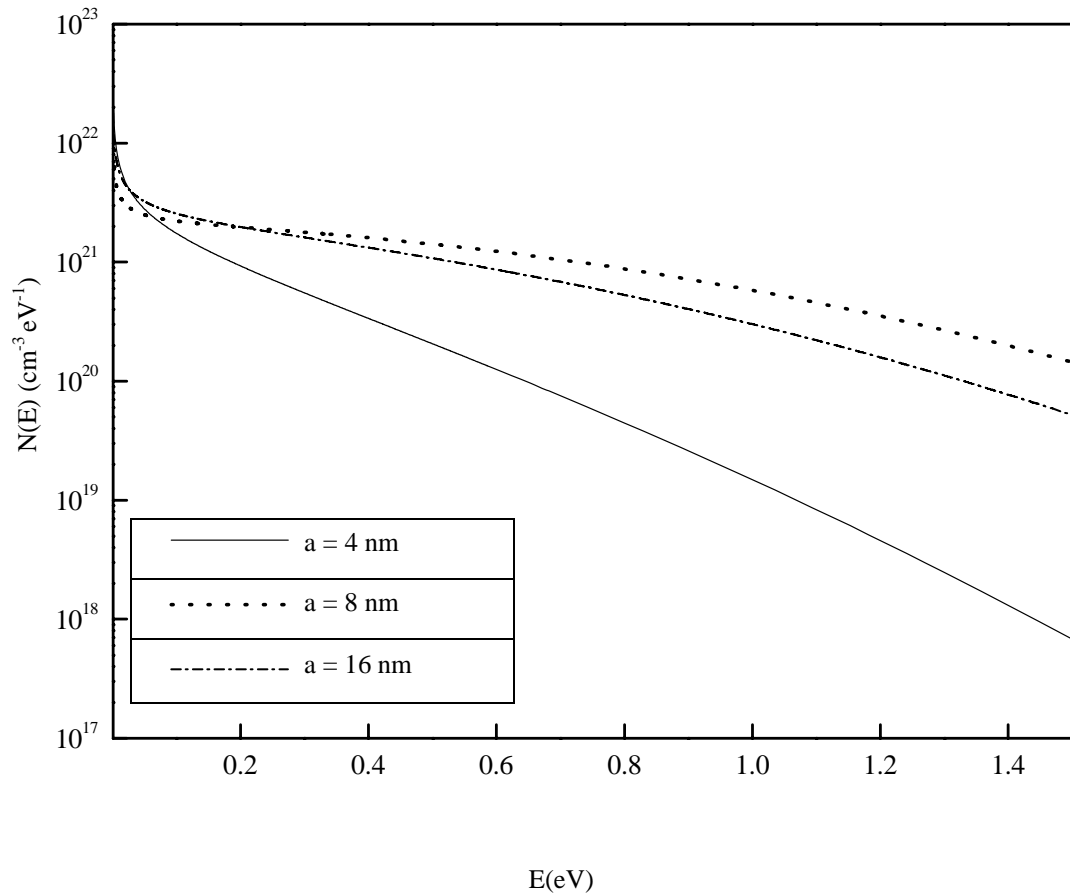


Figure 2.12. Total number of DOS ($N(E)$) corresponding to various selections of potential well widths (a); $N(E_C)$ is set to $10^{22} \text{ cm}^{-3} \text{ eV}^{-1}$ in all cases.

As a result, the DOS distributions for the three different energy regions in the mobility gap are obtained by using the defect pool model. This analysis is essential to understand the optical and electrical characteristics of the amorphous structure in which transitions via localized states play an important role for conduction mechanisms. Therefore, the obtained DOS distribution especially allows us to characterize the electrical transport mechanisms of $\text{a-SiC}_x\text{:H}$ thin films, reported in chapter 8.

CHAPTER 3

EQUIPMENTS AND THEIR IMPLEMENTATIONS

3.1 ASPECTS OF PLASMA ENHANCED CHEMICAL VAPOR DEPOSITION TECHNIQUE

Plasma is a collection of free charge particles moving in random directions that is, on the average, electrically neutral. Under sufficient electric field, the gas in the plasma reactor starts to breakdown by a random initial electron or cosmic radiation, generating a highly reactive plasma medium, which consists of electrons, ions, radicals and other active species. Types of collisions between particles in the plasma can be given most generally as follows (Lieberman, 1994, Atilgan, 1993):

1. Elastic collision: $e_{\text{fast}} + A_{\text{slow}} \rightarrow A_{\text{fast}} + e_{\text{slower}}$

2. Inelastic collision: $e + B \rightarrow B^+ + 2e$ (Ionization)

$e + AB \rightarrow e + A + B$ (Dissociation)

$e + AB \rightarrow A^- + B$ (Dissociative attachment)

$e + B \rightarrow B^+ + 2e$ (Dissociative ionization)

$e + A \rightarrow A^* + e$ (Excitation; kinetic energy transferred to

internal energy leading to glow, during the return to ground state)

Through inelastic collisions respectively small energies are interchanged, since the mass of the electrons are very small with respect to the heavy atoms. The electrons loose their energy mainly by inelastic collisions. These type of collisions produce electron and ion pairs whereas molecular dissociation leads to atoms and free radicals. The free radicals are neutral, but in a state of incomplete chemical bonding and resultantly very reactive. These radicals are behind the etching process or film deposition process by plasma. There are continuous loss and creation of charged species in the plasma medium. At steady state, charged particle generation and the loss balance each other, in other words, the plasma is self sustained.

A schematic diagram of capacitively coupled radio frequency (RF) discharge is given in Figure 3.1. As soon as the plasma is obtained, the current starts to flow between electrodes. For ac voltage of sufficient amplitude for creation breakdown at negative cycle positive ions are accelerated towards electrode 'A'. At positive cycle negative ions and electrons are accelerated towards the electrode A. During one cycle many more electrons than positive ions are collected, leading to a net negative charges on this electrode. For the subsequent cycles, this negative charges will repel the new incoming electrons and attract the new incoming positive ions, such that at steady state electron charge flowing towards live electrode is equal to positive ion charge. So permanently, a negative charge exists at this electrode, causing a negative dc offset voltage bias, V_A .

There are three main regions in potential distribution between the electrodes (Figure 3.1): Grounded electrode with potential V_B , glow discharge region with a potential V_P and power electrode with potential V_A with respect to ground electrode. The larger potential drop occurs at the powered electrode, which is more negative with respect to ground, therefore powered electrode is called the cathode (A) and the grounded electrode is called anode (B). If the samples are placed on anode, this is called plasma etching or plasma deposition. Contrarily, if the samples are placed on cathode (A), this process is generally used for reactive ion etching.

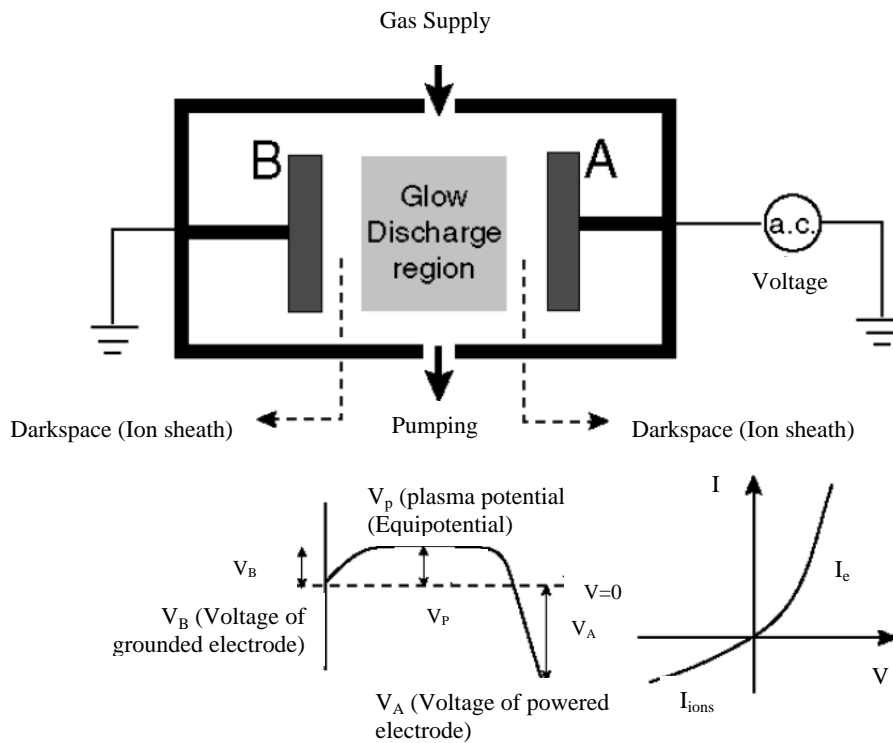


Figure 3.1. Schematic diagram of a capacitively coupled radio frequency discharge. Spatial distribution of the average potential between the electrodes is given just below the inter-electrode region, I_e and I_{ions} denote electron and ion currents, respectively (Atlgan, 1993).

The electrons are more rapidly accelerated, due to their smaller mass with respect to the ions. So average crossing time of electrons is smaller than the average crossing time of ions. Consequently, at any instant ion concentration is larger than the electron concentration. Because of this reason, space charges are built by ions near the electrons. Upon entering the dark space from the electrode, the electrons are accelerated by the space charge field and they cause ionization. This region is called dark space or ion sheath. The electrons, after losing most of their energy in dark region, are slowed and could only cause excitation. The glow discharge region occurs upon recombination of electronically excited molecules and corresponds to the region, where the potential is approximately equals to the plasma potential, seen in Figure 3.1.

The conductivity characteristic of the plasma is like a leaky diode (Figure 3.1). As the frequency of the applied field increases from very low (dc) to higher

values (ac), beyond a certain value, the ions created during the breakdown cannot be fully extracted from the inter-electrode gap in one half cycle of the field. On the other hand, electrons are easily extracted, due to their lighter masses. As a result, the electron current is always greater than ion current ($I_e > I_{ions}$). For higher frequencies, a large fraction of electrons has insufficient time to drift to the positive electrode, during a half cycle. Instead, these electrons oscillate in the inter-electrode gap and undergo collisions with gas molecules. This range of frequency is called RF range (typically 25 kHz-25 MHz) (Atilgan 1993).

3.2 PLASMA ENHANCED CHEMICAL VAPOR DEPOSITION SYSTEM

Plasma enhanced chemical vapor deposition system (PECVD) consists of a plasma reactor and a gas handling equipment, given in Figures 3.2 and 3.3, respectively. The operation of this system needs sensitive and careful control of deposition parameters such as pressure, temperature, power and flow rates of the source gases, due to the fact that, they strongly influence the structural, electronic and optical properties of deposited film.

The deposition of the films obtained on the bottom electrode of the parallel plate capacitor type plasma reactor. The RF power of plasma generator, which is applied to the top electrode, is one of the main parameter of this unit, that must be controlled effectively. The RF power is generated by the quartz crystal oscillator at the frequency of 13.56 MHz and then amplified by appropriate solid state electronic circuits and finally applied effectively to the top electrode through a matching unit. The impedance matching unit is needed to transfer the power from the generator to the electrodes, because some of the power may be reflected back, if the output impedance of the generator does not match with the impedance of the load circuit including the capacitance of the reactor electrodes. Since, the electrode diameter in the reactor is 24 cm, the maximum power applied on the electrodes has a power density of 0.66 W/cm^2 .

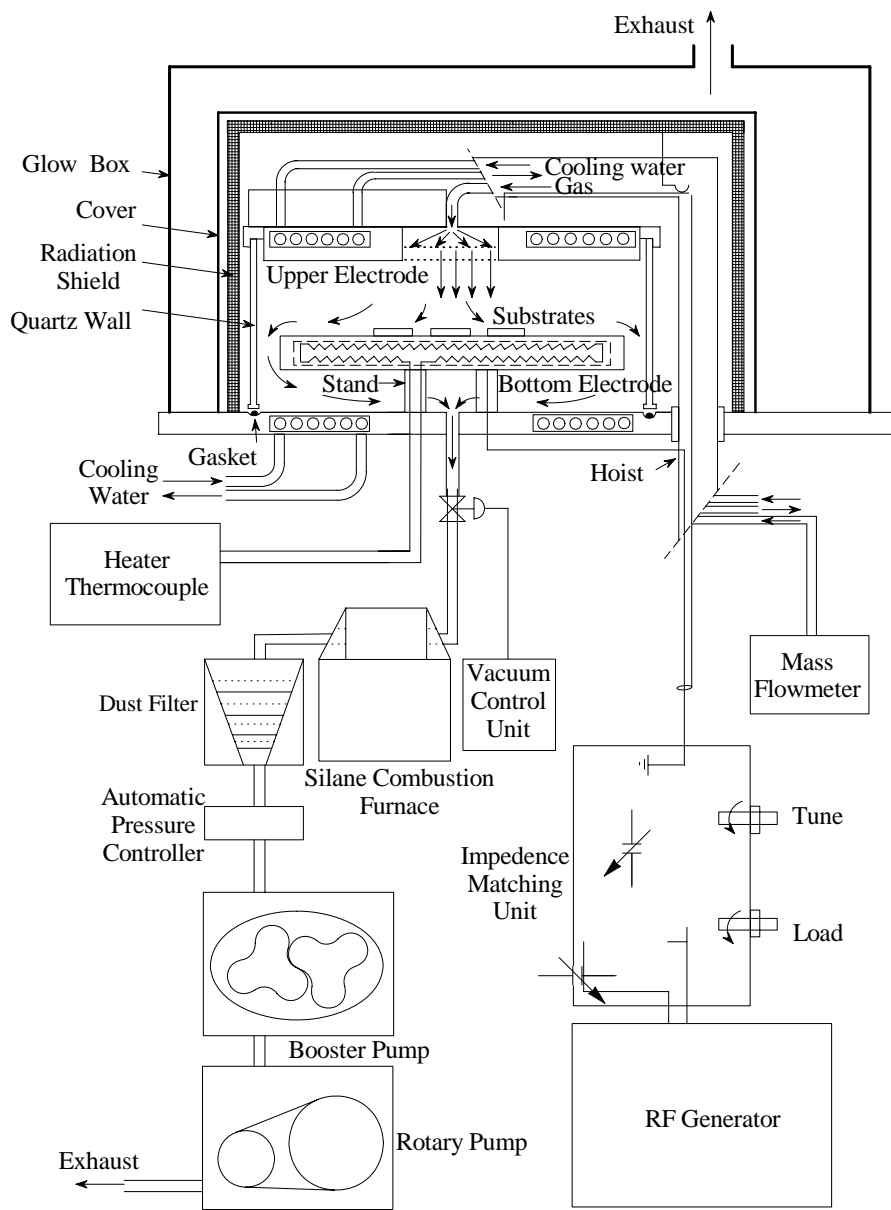


Figure 3.2. PECVD reactor.

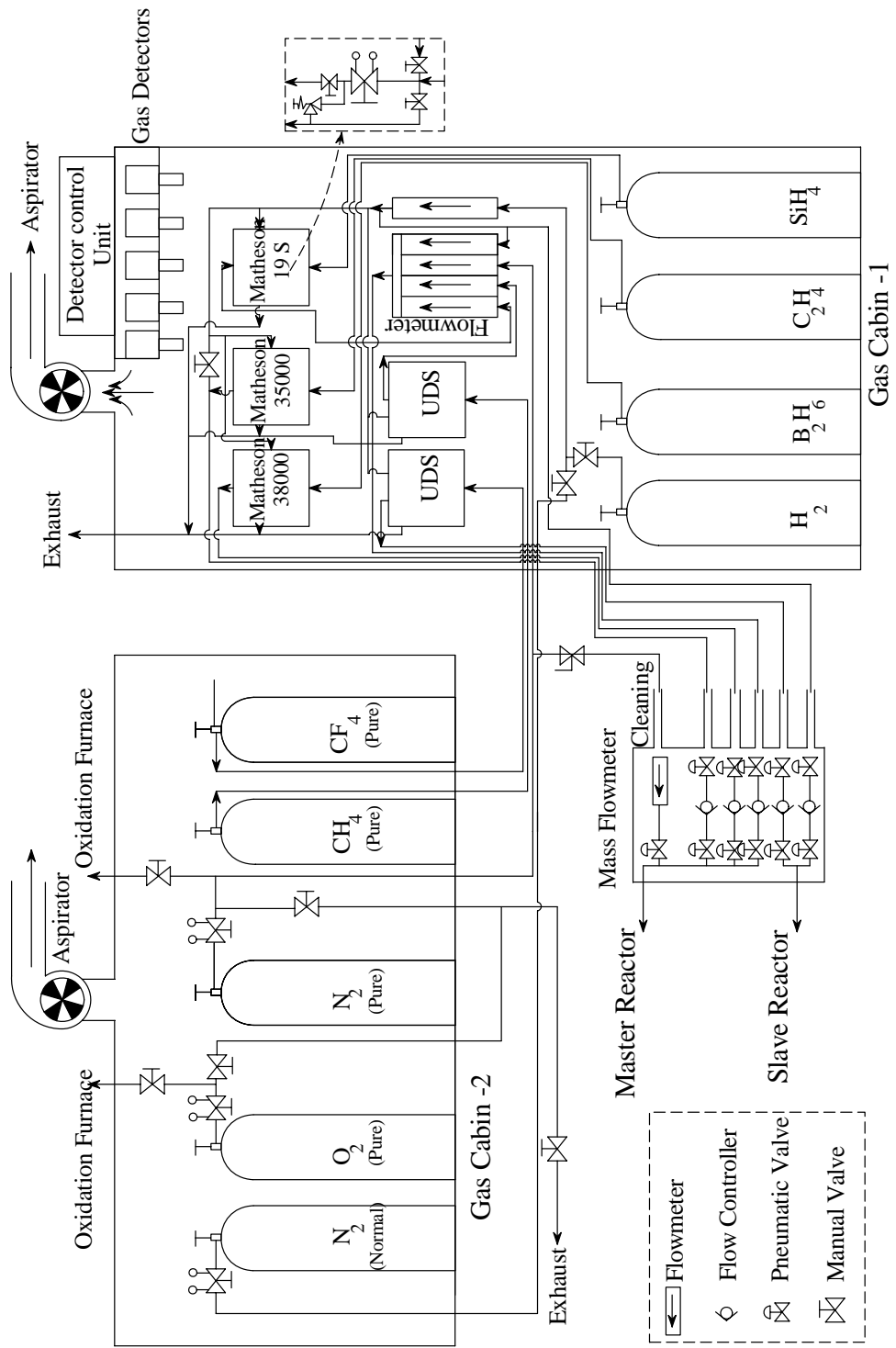


Figure 3.3. Gas delivery system.

Sensitive control of vacuum is crucial for maintaining the sufficient vacuum level for effective decomposition. The pumping rate of the integrated pumping system (A booster and a rotary pump) is controlled by the automatic pressure control unit, which enables us to adjust vacuum level between 0.1 mTorr to atmospheric pressure. Along with the vacuum control, independent control of the flow rate of the gases also assists the desired deposition conditions. The relative concentration of gases in the reactor can be adjusted by the flowmeters and mass flow controllers. The mass flow controllers can adjust the gas flows from 1 ccm to 200 ccm depending on the type of the gas.

The temperature of the substrates on the bottom electrode can be adjusted in the range 0 to 400 °C, in order to control the properties of the deposited film.

3.3 METALLIZATION SYSTEM

Metallization is required for electrical characterization measurements of the films. In this respect, for current-voltage measurements of the films, metal contacts, such as Al, Cr, should be deposited. For this purpose, two different metallization systems are available. One of them is Univex450 vacuum system consist of an e-beam and a magnetron sputtering system, given in Figure 3.4.

The vacuum pumping mechanism of this system consists of rotary and turbo molecular pumps. The system is very fast and so high vacuum up to 10^{-6} Torr , detected by pirani and ion gauge, could be attained. The deposited film thickness is measured by XTC thickness monitor by the help of resonance frequency of a piezo-electric crystal. (Atılgan, 1993).

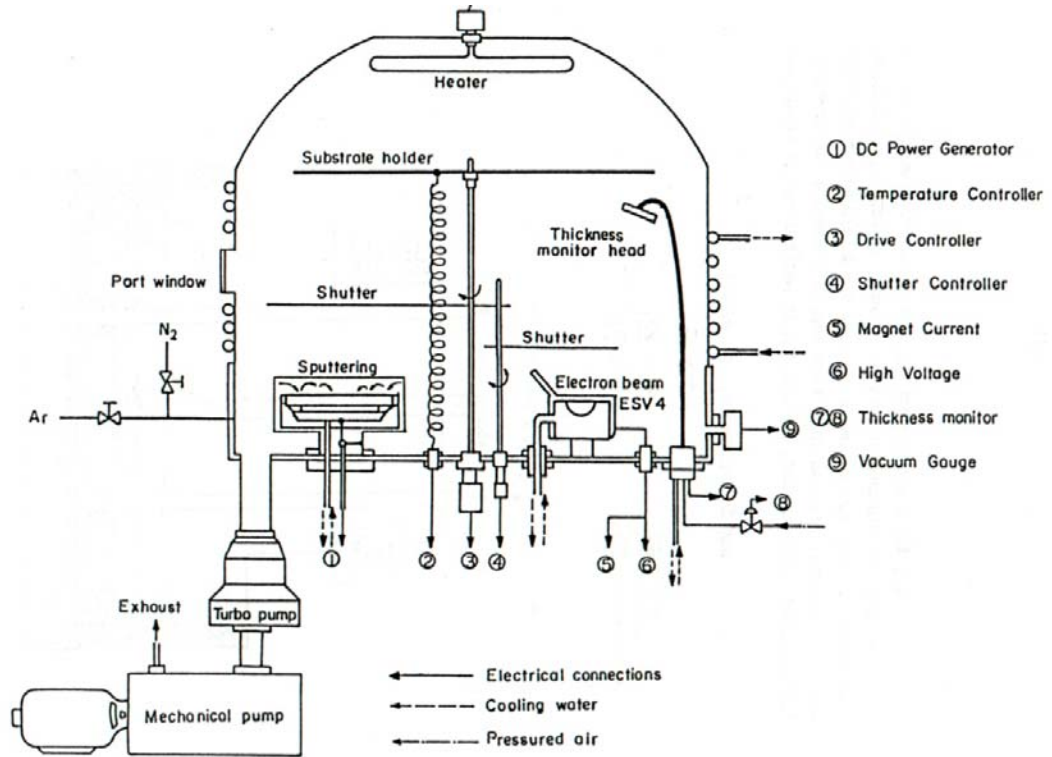


Figure 3.4. Schematic view of Univex450 model e-beam and magnetron sputtering system (Atılgan, 1993).

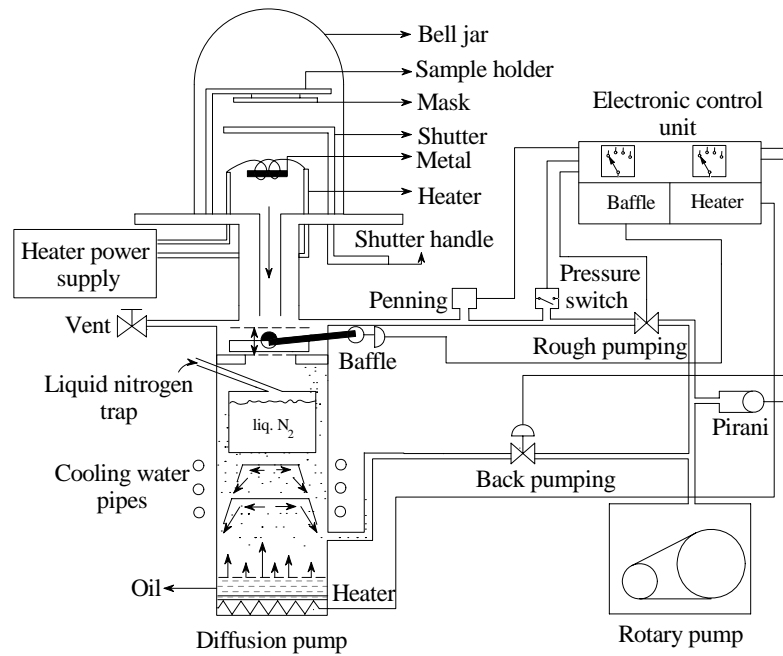


Figure 3.5. Schematic view of metallization system.

The other metallization system, given in Figure 3.5, consists of resistive evaporator unit and rotary and diffusion pumps. The vacuum level of the system is detected by pirani and penning gauges. It is used only for Al coating, which does not require very high temperatures under vacuum.

3.4 FOURIER TRANSFORM INFRARED SPECTROSCOPY SYSTEM

Fourier transform infrared spectroscopy (FTIR) enables us to analyze the molecular vibration characteristics of the films. FTIR system consists of an air pump, an air drying unit, FTIR spectrometer and a computer

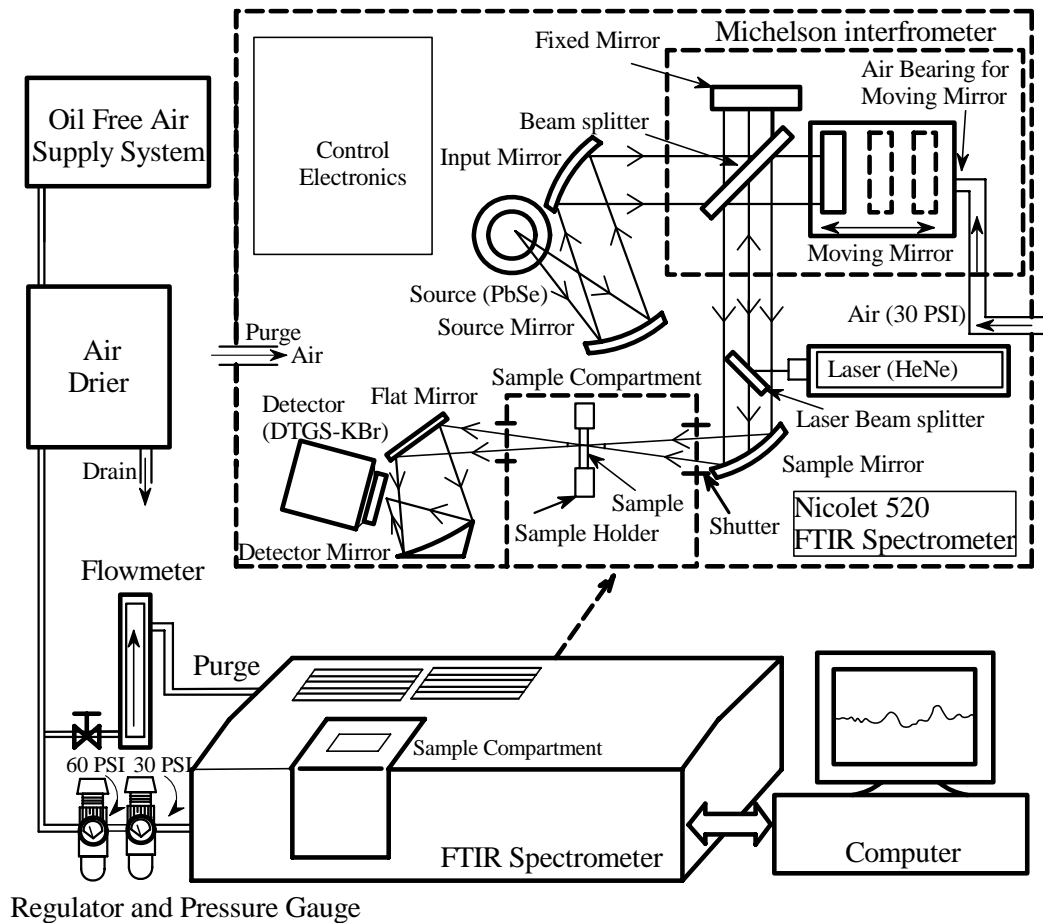


Figure 3.6. Fourier transform infrared spectroscopy system.

The air pump and air drying unit is primarily used to purge the system of water vapor, CO₂ and volatile solvents and secondly to operate the delicate air bearing for the moving mirror of the spectrometer. By purging the system with nitrogen or air the unwanted absorbencies of water vapor and CO₂ could be minimized. For best performance, instead of air, nitrogen should be used for this purpose.

FTIR spectroscopy measurements are taken by using a Nicolet 520 spectrometer. In FTIR spectrometer, there are three basic components: A source (PbSe), a Michelson interferometer and a detector (DTGS-KBr). The Michelson interferometer, which consists of a beamsplitter, a fixed mirror and a moving mirror, preserves both frequency and intensity information and replaces the conventional monochromator. The control of the system and the resultant data processing are accomplished by a computer. For further analysis, such as peak deconvolutions of the obtained absorption spectrum, Peak Fit v4.12 computer program is used.

3.5 ULTRAVIOLET-VISIBLE TRANSMISSION SPECTROSCOPY SYSTEM

Ultraviolet-Visible (UV-Visible) transmission spectroscopy enables us to determine the thickness, refractive index, absorption coefficient and the energy band gap of the films.

Perkin Elmer Lambda 2 double beam spectrometer is used for ultraviolet-visible (UV-Visible) transmission spectroscopy measurements. This system consists of a monochromator with concave holographic grating with 1053 lines/mm for a wavelength range of 200-1100 nm, photo-diode detector and a computer. As the radiation sources, deuterium and Tungsten-halogen lamps are used. The transmittance is detected by photo-diode detectors.

The output data is transmitted to the computer by RS-232 interface and further optical analysis of the transmittance is performed by an optical analysis

software, called OptiChar. It has been experienced that the numerical inversion methods may result in multiple solutions. In order to avoid such an ambiguity in results such as thickness, refractive index... obtained from OptiChar, the spectra are analyzed additionally by the envelop method (Tikhonravov, 2002, Manificier, 1976, Swannepoel, 1983a, 1983b).

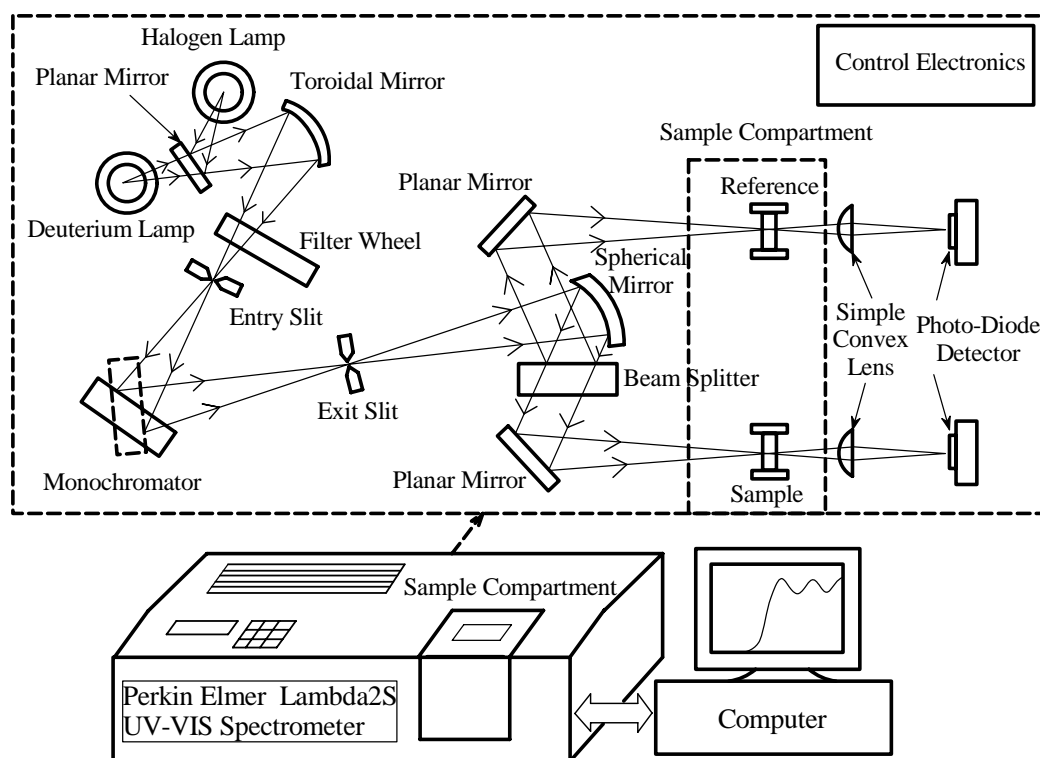


Figure 3.7. UV-Visible transmission spectroscopy system.

3.6 CONDUCTIVITY MEASUREMENT SYSTEM

The conductivity measurements are important to determine the electrical characteristics of the films. There are two different conductivity measurement systems, one of which is for the room temperature conductivity measurements and the other one is for the temperature dependent conductivity measurements. The room temperature conductivity measurement system is relatively simpler and enables more practical and quick measurements. It consists of an

electrometer/voltage source (KEITHLEY 6517), a sample box and a computer (Figure 3.8). The sample is placed in the sample box and the needle contacts, are mounted on three-dimensionally movable stages. The conductivity data is obtained automatically by the control of a computer, via Labview program.

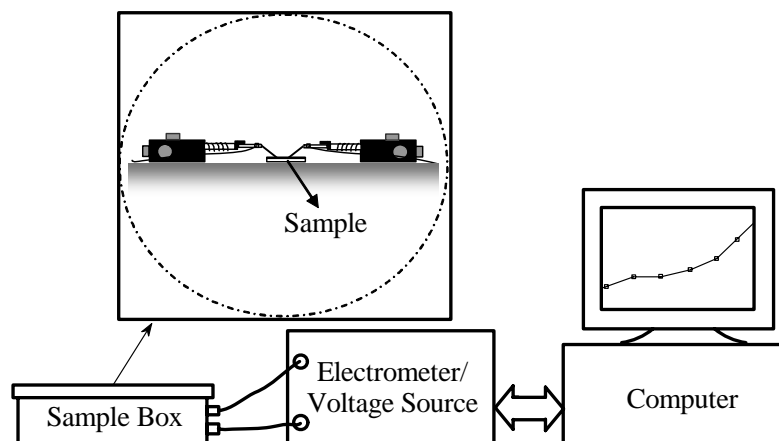


Figure 3.8. Room temperature dc conductivity measurement system

The temperature dependent conductivity measurement system includes some additional components with respect to the room temperature conductivity measurement system. The schematic diagram of the system is given together with a detailed diagram of the sample compartment in Figure 3.9. In this system, a closed cycle He cryostat (S204 of ARS) is used for cooling. And hence it enables us to adjust the sample temperature between 13-450 °K. The electrical contacts to the sample are obtained by two conductive needles on the tail of the cryostat. To scope the temperature, there are two thermal sensors; one of the sensors is placed on the heater, whereas the other one is placed on the sample to measure the sample temperature. The temperature control is accomplished by using a LakeShore 331 model temperature controller by processing the output data obtained from heater thermal sensor and adjusting the gain of the heater. The sample compartment is covered by radiation shield and vacuum shield. The

radiation enables us to reach lower temperatures by shielding the blackbody radiation. The vacuum shield covers over the cryostat, since the vacuum, maintained by a rotary pump, is essential at low temperatures. The vacuum level is detected by ionization vacuum gauge (Leybold model).

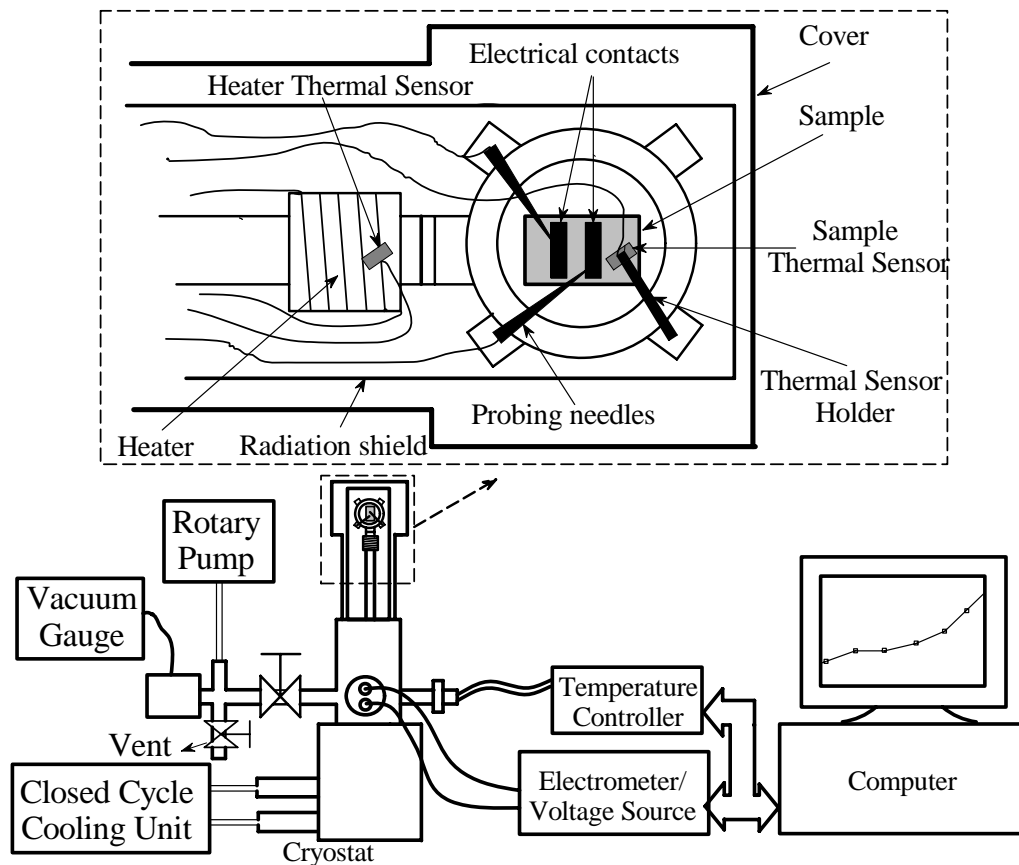


Figure 3.9. Temperature dependent dc conductivity measurement system.

CHAPTER 4

SAMPLE PREPERATION

a-SiC_x:H films were deposited on various substrates, such as crystal silicon wafers, ordinary glass and quartz. The crystal silicon wafers were used for FTIR spectroscopy and conductivity measurements. Ordinary glasses were used for UV-visible, photoluminescence and electroluminescence spectroscopy and conductivity measurements. Finally, the quartz substrates were used for UV-Visible spectroscopy measurements of the films.

The film deposition is susceptible to cleanliness of both deposition environment and substrates. So to fabricate samples a meticulous cleaning procedure must be performed. The fabrication set up and substrates must be cleaned by appropriate cleaning procedure.

4.1 SUBSTRATE CLEANING

Crystal silicon wafers were cleaned by performing the following procedure. First, samples were boiled in trichlorethylene for 5 minutes. Second, they were rinsed in deionized water (DW) H₂O and agitated by ultrasound at the same time. The rinsing process was repeated after each step during the cleaning procedure. Third, samples were dipped in HCl/H₂O₂ mixture, with 1/1 mixing ratio, for 10 minutes. Fourth step was dipping samples in H₂SO₄/H₂O₂ mixture, with 2/1 mixing ratio, for 5 minutes. After that, they were washed in running DW

for 5 minutes. Finally, samples were dipped in HF/H₂O mixture, with 1/10 mixing ratio, for 30 seconds and then washed in running DW for 15-20 minutes.

Ordinary glasses and quartz substrates were cleaned by the following procedure. First, they were boiled in detergent for 5 minutes. Second, they were rinsed in deionized water DW and agitated by ultrasound at the same time. Similar to the crystal cleaning procedure, this step is repeated after each step. Third, they were boiled in trichlorethylene for 5 minutes. Fourth, they were dipped in H₂O₂ for 5 minutes.

4.2 PREPARATION OF a-SiC_x:H FILMS

4.2.1 PLASMA REACTIONS

The gas molecules lose some of their electron or atom by colliding with energetic plasma species. The resultant electrons or charged atoms, which oscillate by the electric signals, are responsible for continuous plasma environment and called plasma species, as mentioned in chapter 3. Although the energy of ions or radicals is very low, they could react to each other or other gas molecules upon collisions and result in radical generation. On the other hand, the free electrons could be easily accelerated by the applied electric field (Radio frequency, RF) to gain sufficient energy to break the bonds of a molecule. Although the densities of all of the species are nearly equal, mostly electrons, which are more energetic, collide with the incoming molecules to start and maintain continuous plasma dissociation processes. As a result, type of the radicals or ions, generated by these collisions, depends on the type of the incoming gas molecules. The reactions of ethylene silane mixture in the plasma can be grouped in to three (Atilgan, 2001).

- a) Ethylene reactions
- b) Silane reactions
- c) Ethylene and silane mixture reactions

4.2.1.1 ETHYLENE REACTIONS

The primary radicals, generated by the collisions of electrons with ethylene gas molecules entered into the plasma, are listed in the following reaction (Kruangham, 1991, Inagaki, 1996, Catherine, 1979, Dagel, 1996, Fujii, 1997):



The energies of the reactions 1b and 1c are nearly the same and so they can be reversed (Kobayashi, 1974a). Here, the resultant product is the acetylene which can be taken as the main radical responsible for the film deposition (Reaction 1d).

In the second phase, the higher mobility of H atoms compared to the other radicals and the rapid reaction between the radicals (including ethylene molecules) and H atom may lead to following reactions in the plasma atmosphere.



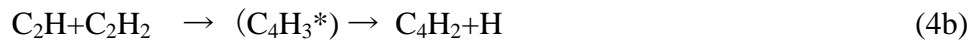
The C_2H_3 radical, which is formed in the reaction 2a, immediately forms C_2H_2 upon colliding with a hydrogen atom (Reaction 2b). Therefore, reactions 2a and 2b constitute a secondary source of C_2H_2 in the plasma glow. The reaction 2c is a little bit controversial; although, the reaction duration, at 30 mTorr, is about 10^{-14} s^{-1} , at high pressure it increases to 10^{-12} s^{-1} (Dagel, 1996). So, the reaction

2c, which enables the formation of radicals with more carbon atoms, is favored at high pressures and thus formation of radicals with more carbon atoms increases at high pressures.

In the plasma environment, the radicals, which have many atoms, could collide with each other with a probability less than the ones, with fewer atoms. The density of CH₃, formed by reaction 2d dominates the plasma atmosphere, because of its small reaction speed and small sticking coefficient. Thus following reactions could occur (Dagel, 1996).



If the radicals with more C atoms collide with ethylene or acetylene molecules, due to the enhanced probability of collisions at high pressures, they could react with them and thus form bigger radicals (Kobayashi, 1974b). As a result, the polymerization start and dust particles may be formed in the plasma atmosphere. These dust particles could stick to the growing film surface and damage the structure of the film. This effect especially occurs in the plasma when high density of radicals is generated by high power density and/or high pressure in the reaction chamber. The following reactions are the examples of these types of reactions (Fujii, 1997).



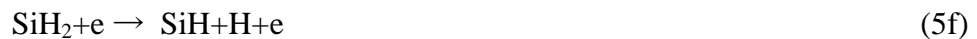
where ‘*’ represents the ionic form of that molecule. The ionic form of C₄H₃ is not stable, for this reason, C₄H₃^{*} could immediately lose one of its hydrogen atoms, forming the more stable C₄H₂. It is observed that, in the plasma

environment the high density of C_4H_3 is measured, pointing that the life time of C_4H_3 radical is long (Reaction 4c). As a result of the 4c reaction, aromatic rings could be formed in the gas environment (Dagel, 1996).

The plasma species reaching the growing film surface and then sticking on it are expected to be the neutral C_2H , C_2H_3 and C_3H_5 radicals as being the main precursors leading to film growth. These radicals might lose some of their hydrogen atoms as they form a bond on the growing film surface. However, it is known that deposited films involves a substantial amount of hydrogen (Giorgis, 1997, Robertson, 1991, Koos, 1999).

4.2.1.2 SILANE REACTIONS

In the plasma environment, initial reactions between silane (SiH_4) molecules and the plasma electrons are;



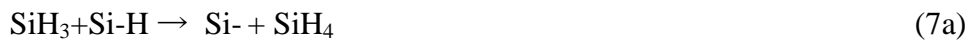
Although the reaction 5b is the fastest reaction of all, the SiH_3 radical becomes dominant radical in the plasma atmosphere due to the fact that the SiH_2 radical is highly reactive and reacts with other radicals easily. In the plasma, free Si could also be formed, but they do not contribute to the deposition of the film, because the density of them is rather small (Street, 1991).

In the second phase, when formed radicals collide with the molecules and other radicals, they react with each other. Since, the SiH_4 molecules are very dense, the reactions between the other molecules and radicals can be neglected

(Street, 1991). Moreover, SiH₃ is very stable after its collision with SiH₄ and its lifetime in SiH₄ plasma is significantly longer than that of any other radicals and atoms (Atilgan, 1993). Apart from the reactions between electrons and SiH₄ (primary reactions) at the initial stage of the plasma, secondary reactions occur between generated species, SiH₄ molecules, photons and electrons. SiH₃ is found to be at least 80% of the gas radicals in the silane plasma. Various experiments show that SiH₂ and SiH₃ are generated in the plasma with the highest efficiency whereas the other generated species such as SiH and Si require larger energies, that is, they have relatively limited efficiencies. The cross-sections for generation of ions (SiH⁺, SiH₂⁺, SiH₃⁺) and excited species have much lower values than generation of neutral radicals such as SiH₂, SiH₃, SiH and Si (Tanaka, 1999).



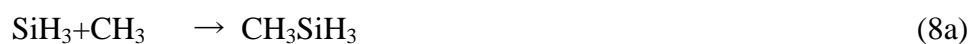
At the last phase, the radicals reaching the substrate or film, are adsorbed at the surface and then connected to the film. During, the deposition of hydrogenated amorphous silicon, all the radicals contained in the plasma cloud contribute to the deposition, but the SiH₃, which is very dense, is the dominant radical in this process (Street,1991, Atilgan, 1993). This mechanism at the surface can be outlined in the following way.



If the SiH₃ radical is adsorbed via the Si-H bond, the bond of hydrogen atom is broken and a gaseous silane molecule is formed, leaving a dangling bond (Reaction 7a). If it directly sticks to the dangling bond, Si-Si bond is formed and resultantly amorphous silicon film could be deposited. At higher plasma power densities, ion bombardment might be enhanced and these energetic ions can reduce the hydrogen surface coverage and break up polymeric chains with increasing the concentration of monohydride bonds (Jacobsson, 1965). Such a decrease in hydrogen coverage may increase the deposition rate because the surface of a-Si:H does not allow direct Si-Si bonding for SiH₃ radical if the surface is fully terminated by hydrogen. Besides, increasing the power density also increases the micro-columnar structure (Knights, 1981, Kampas, 1982)) and formation of microcrystalline silicon causing a sharp decrease in both the hydrogen content and the optical band gap.

4.2.1.3 ETHYLENE AND SILANE MIXTURE REACTIONS

If the mixture of ethylene and silane gases is present in the plasma, besides the reactions given above, the cross-reactions between the radicals of these two gases also occur (Catherine, 1981, Dieguez Cambo, 1998, Jasinski, 1995, Atilgan, 1993)).



It has been reported that, the reactions 8a and 8b occur in the plasma of silane-methane mixture (SiH₄-CH₄) (Catherine, 1981, Jasinski, 1995). In the silane-ethylene mixture the reaction 8c becomes dominant and it generates silirane molecule. In the deposited films, besides Si-C bonds, Si-Si and C-C bonds are also present. Keeping in mind the complexities of previously outlined

deposition mechanisms of a-Si:H and a-C:H films separately, it is not a surprise to have an even more complex deposition mechanism for hydrogenated amorphous silicon carbon alloys. Nevertheless, the formation and the amount of dangling bonds on the growing surface might be considered, as an essential part, which determines the deposition with various aspects, since radicals easily become bound on the surface through dangling bonds. As C_2H_4 and SiH_4 radicals react with H atoms on the growing surface, become physisorbed on the surface and then desorbed, leaving a dangling bond on the growing surface. On the other hand, the presence of unsaturated dangling bonds on the growing surface decreases the diffusion coefficient of the adsorbed radicals and hence deteriorates the film properties by causing columnar structure, which include voids, stressed bonds, sp^2 type bonds etc. In addition, it is difficult to eliminate H from the surface in comparison to the a-Si:H deposition, since C-H bonds are stronger than the Si-H bonds. Therefore, a- SiC_x :H films contain more H than a-Si:H films and most of the H atoms are found to be bonded to C. It should be noted that hydrogen dilution during the growth compensates elimination of hydrogen from the growing surface by saturating dangling bonds.

4.2.2 DEPOSITION OF a- SiC_x :H FILMS BY PECVD SYSTEM

For the deposition of a- SiC_x :H films PECVD system was used.. After the cleaning process, the substrates were loaded onto bottom electrode of the PECVD reactor as soon as possible, to prevent the substrates from atmospheric contamination. Afterwards, the reactor was pumped down to a base pressure of 1 mtorr and the temperature of the bottom electrode was adjusted to 250 °C. Next, an in situ cleaning was performed by the hydrogen plasma with 100 ccm H_2 flow under $100mW/cm^2$ of radio frequency (RF) power density, at the deposition pressure for 5 minutes. Right after the cleaning, the deposition gases silane and ethylene are introduced into the chamber under constant pressure of 0.5 torr. Then, the flow rates of the source gases are maintained. All deposition parameters

are given in table 4.1. and power to the values given in table 1 and the pressure to 0.5 torr, the deposition was started.

Finally, eight different depositions of a-SiC_x:H films with four different carbon concentrations, at two different RF power densities (Lower (LP) and higher (HP) of 30 mW/cm² and 90 mW/cm²) were performed.

Table 4.1. Film deposition parameters

RF power density (mW/cm ²)	M _{C₂H₄}	F _{C₂H₄} (ccm)	F _{SiH₄} (ccm)
LP 30 (mW/cm ²)	0	0	20
	0.2	4	16
	0.5	10	10
	0.7	20	6
HP 90 (mW/cm ²)	0	0	20
	0.2	4	16
	0.5	10	10
	0.7	20	6

4.3. METALLIZATION

The electrical characteristics of the films were analyzed in both lateral and transverse directions by I-V measurements. For this purpose, the electrodes on the samples were prepared by metal evaporation through shadow masks in the physical vapor deposition system, described in chapter 3. For lateral measurements of the films on the glass substrate, planar finger electrodes were formed on the films (Figure 4.1a). On the other hand, for transverse measurements, firstly a layer of metal was coated on the glass substrate, as a back electrode. Secondly, the metal was deposited on the film through shadow masks in order to have dot contacts, as front electrodes shown in Figure 4.1.b.

For the films deposited on the crystal silicon wafers electrical measurements were performed by sandwich structure. Hence, after depositing the film, a layer of metal was coated on the back of the substrate as a back electrode, and then dot contacts were coated onto the film, as front electrodes (Figure 4.2).

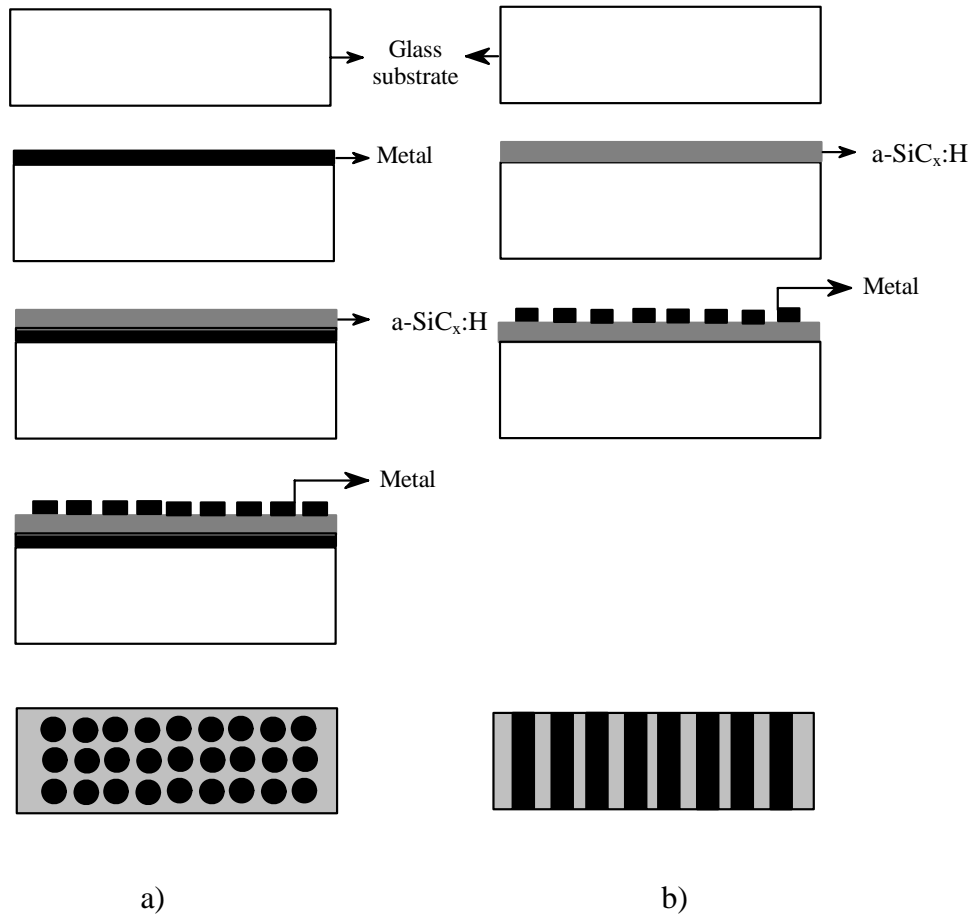


Figure 4.1. Metal electrodes were coated on the films on glass substrate for a) transverse, b) lateral conductivity measurements.

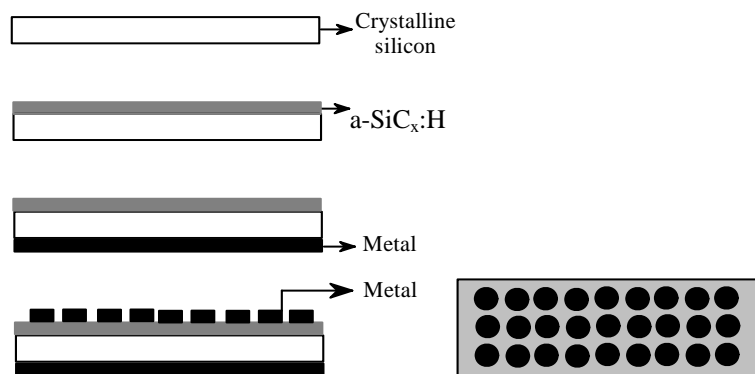


Figure 4.2. Metal electrodes were coated on the films on crystalline substrate for transverse conductivity measurements.

CHAPTER 5

X-RAY PHOTOELECTRON SPECTROSCOPY ANALYSIS OF a-SiC_x:H FILMS

The elemental compositions of a-SiC_x:H films, deposited by PECVD with various gas concentrations at two different r.f. power densities (Lower (LP) and higher (HP) powers of 30 mW/cm² and 90 mW/cm²) were investigated by a SPECS ESCA (Berlin/Germany) x-ray photoelectron spectroscopy (XPS) system. The XPS spectrum was recorded using unmonochromatic Al K α radiation. EA 200 hemispherical electrostatic energy analyzer equipped with multichannel detector (MCD) with 18 discrete channels is operated in constant pass energy mode of 144 eV. The x-ray source was run at 250 watt and at the take of angle of 90° (Central Laboratory, METU).

In XPS, the photon is absorbed by an atom in a molecule, leading to ionization and the emission of a core (inner shell) electron. The kinetic energy distribution of the emitted photoelectrons can be measured using an appropriate electron energy analyzer and a photoelectron spectrum can be obtained (Figure 5.1).

$$KE = h\nu - BE - \phi \quad (5.1)$$

where KE is the kinetic energy of the photoelectron, BE is the binding energy and ϕ is the work function. For the case, $\phi > h\nu$, no photoemission occurs and for the levels with energy $BE + \phi > h\nu$ again no photoemission could occur.

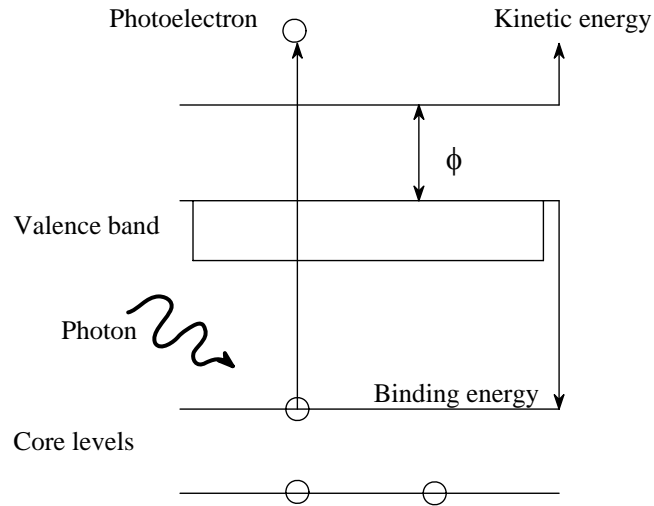


Figure 5.1. Photoemission process in XPS.

XPS analysis were obtained from 10x10 mm samples of a-SiC_x:H films, which were deposited on the ordinary glass substrates. Since, these analysis were performed nearly 6 months after the deposition of the films, the surface of the films could be affected and differentiated from the bulk of the film. In order to investigate the surface effects, such as oxidation due to presence of the films in the atmosphere prior to the XPS measurements; first, a measurement was performed from the surface of LP a-Si:H sample (M=0) by scans at the energy resolution of 0.4 eV, which is given in Figure 5.2. Second, to investigate the bulk of the film, it was sputtered by Ar ion bombardment at 5 keV for 15 minutes. After that, the detailed XPS spectrum was obtained by several scans at the energy resolution of 0.2 eV and given in Figure 5.2. In order to eliminate the charging effect, the binding energies were referenced with respect to C 1s core level at 284.5 eV (Handbook of XPS). In the Figure 5.2, the peak around 531 eV (Handbook of XPS), which corresponds to O 1s core level, was observed very intense for the surface measurement, whereas it reduced to very small intensity

for the bulk measurement of the film. The presence of O peak reveals that the surface of the film is oxidized and even in the bulk, there exists oxygen by the diffusion from the surface, occurred in the long pre-analysis time interval. Although this film, LP a-Si:H (M=0), should not contain C atoms, in the XPS spectrum (Figure 5.2), carbon peak around 284.5 eV were observed. This peak probably occurred from the background of the XPS system. On the other hand, Si 2s around 151 eV and Si 2p around 99 eV (Handbook of XPS) peaks remain almost the same for both surface and bulk measurements.

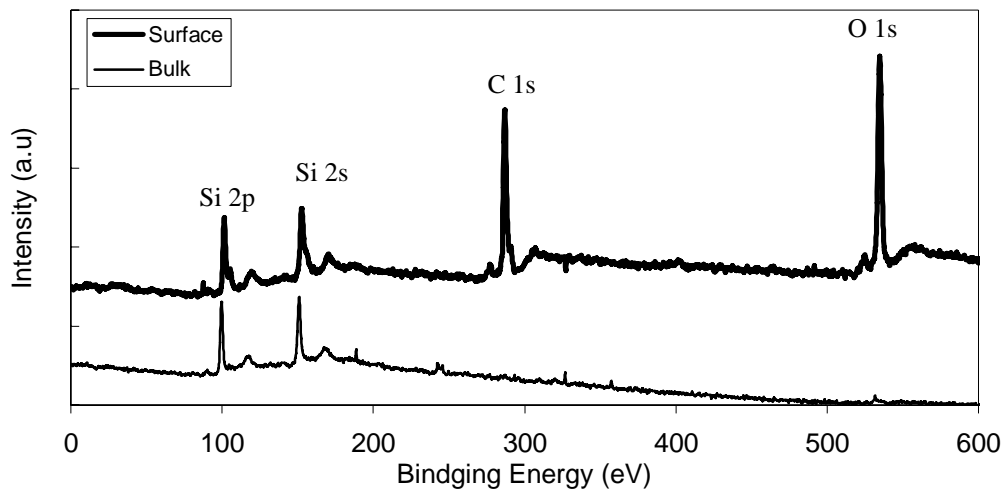


Figure 5.2. XPS spectrum of LP a-SiC_x:H film with M=0.7 obtained from the surface and from the bulk.

The elemental compositions of the films can be calculated as (Handbook of XPS);

$$\%X = \left(\frac{I_x}{S_x} \right) / \sum_{i=1}^N \left(\frac{I_i}{S_i} \right) \quad (5.2)$$

Where X is the elemental composition, I_x is the area under the peak of the element X in the spectrum and S_x is the sensitivity factor. The sensitivity factors for C and Si are 0.25 and 0.27, respectively (Briggs, 1990). The elemental compositions for the surface and bulk of the LP a-SiC_x:H film were calculated by

using equation 5.2 and reported in Table 5.1. For the surface measurement % 48 and even for the bulk measurement % 9 carbon was detected for LP a-Si:H film (M=0). Considering the source of unexpected carbon content of % 9 to be the background of the XPS system (Central Laboratory, METU) the actual elemental composition of LP a-Si:H M=0 film, which is given in Table 5.1, as normalized elemental composition of bulk, could be obtained.

Table 5.1. Elemental compositions of the LP a-S:H film (M=0) obtained from surface and bulk.

LP a-SiC _x :H M=0	Elemental Composition %	
	Si (2p)	C (1s)
Surface	52	48
Bulk	91	9
Bulk (Normalized)	100	0

In the light of the above analysis, the carbon contents of a-SiC_x:H films are determined and reported in Table 5.2

Table 5.2. Gas concentration and carbon contents of a-SiC_x:H films, obtained from UV-Visible spectroscopy analysis (Chapter 5) and XPS analysis, together. (XPS analysis of LP a-SiC_x:H with M=0.5 could not be performed.)

	Gas concentration ($M = \frac{C_2H_4}{C_2H_4 + SiH_4}$)	Carbon content (XPS) x
LP	0	0
	0.2	0.17
	0.5	-
	0.7	0.48
HP	0	0
	0.2	0.21
	0.5	0.42
	0.7	0.59

Additionally, for each sample, Silicon (Si 2p), carbon (C 1s) core levels were deconvoluted into a few smaller Gaussian peaks, which are presented in Figure 5.3 and 5.4. For a-SiC_x:H films, the typical binding energies and the bonding types of the peaks corresponding to C 1s and Si 2p core levels are given in Table 5.3. Si 2p peak is best fitted by three peaks, corresponding to Si-C at 101.2 eV (P₂) (Avilla, 2001), Si-Si/Si-H at 99.8 eV (P₁) (Choi, 1998) and O-Si-C/Si-O at 102.7 eV (P₃) (Choi, 1998). Whereas, C 1s peak comprised of four peaks, corresponding to C-Si at 283.2 eV (P₄) (Avilla, 2001, Choi, 1998, Toneva, 1999, Halac, 1999, Sha, 2005), C-C/C-H at 284.5 eV (P₅) (Avilla, 2001), C-O-H and C=O at 286 (P₆) and 288.4 eV (P₇) (Choi, 1998). Since the energy of the C-C and C-H peaks and Si-Si and S-H peaks are very close to each other, these peaks could not be differentiated. Additionally, the O-C and O-Si-C peaks are difficult to detect in C 1s peak, because of their low intensity with respect to the higher intensities of the C-C/C-H and C-Si peaks. In the peak analysis, the full width half maximums (FWHM) of the peaks were taken to be 1.6 eV.

Table 5.3. The binding energies and bond types of peaks, corresponding the Si 2p and C 1s core levels.

Peak No:	Core Level	Binding Energy (eV)	Bond Type
P1	Si 2p	99.8	Si-Si/Si-H (Choi, 1998)
P2		101.2	Si-C (Avilla, 2001)
P3		102.7	O-Si-C/Si-O (Choi, 1998)
P4	C 1s	283.2	C-Si (Avilla, 2001, Choi, 1998, Toneva, 1999, Halac, 1999, Sha, 2005)
P5		284.5	C-C/C-H (Avilla, 2001)
P6		286	C-O-H (Choi, 1998)
P7		288.4	C=O (Choi, 1998)

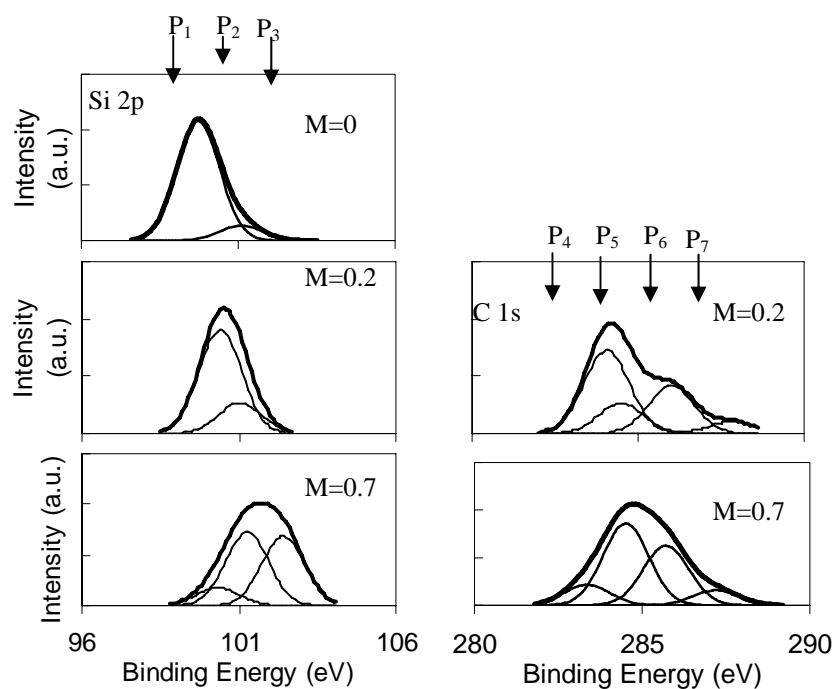


Figure 5.3 Deconvolutions of XPS Si 2p and C 1s peaks of LP a-SiC_x:H films for various gas concentrations. (XPS analysis of LP a-SiC_x:H film with M=0.5 could not be performed.)

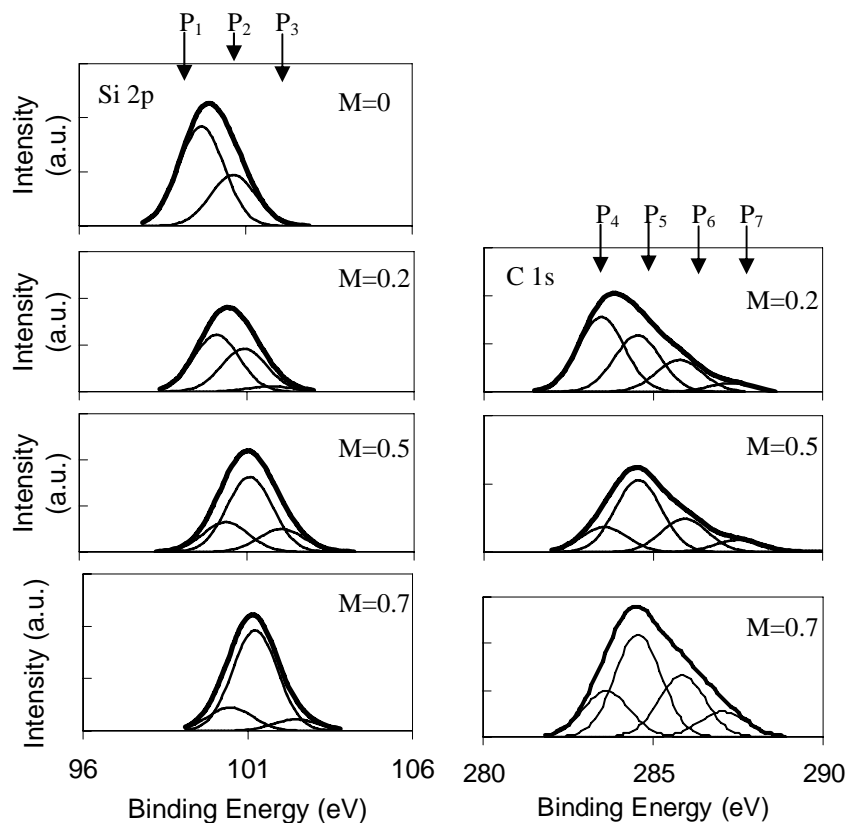


Figure 5.4 Deconvolutions of XPS Si 2p and C 1s peaks of HP a-SiC_x:H films for various gas concentrations.

Table 5.4. The gas concentrations and bonding compositions for a-SiC_x:H films. (XPS analysis of LP a-SiC_x:H with M=0.5 could not be performed.)

	Gas concentration ($M = \frac{C_2H_4}{C_2H_4 + SiH_4}$)	Si-C %	Si-Si/Si-H %	C-C/C-H %
LP	0	0	100	0
	0.2	22	73	5
	0.5	-	-	-
	0.7	36	8	56
HP	0	0	100	0
	0.2	37	50	13
	0.5	43	17	40
	0.7	41	9	50

In Table 5.4 and also in Figure 5.5, the relative compositions of Si-Si/Si-H, Si-C and C-C/C-H bonding configurations are reported. The composition of C-C/C-H bond increases with increasing M, furthermore this increasing trend is found to be relatively higher for LP films. It was expected for LP films that the carbon incorporation into the films and the resultant composition of C-C bonding are relatively small than HP films (Swhartz, 1996). Whereas, for the XPS the LP films seem to have more C-C bonds with respect to LP films, this is probably due to the fact that, for XPS analysis besides C-C bond C-H bond are also detected and added to the overall amount as C-C/C-H. Consequently, the higher amount is probably a result of the increase in the C-H bonds. Besides, Si-Si/Si-H bond decreases as M increases and this decreasing trend is relatively sharper for HP films. On the other hand, Si-C bond increases with the increase in carbon content; moreover, by this increase, Si-C composition reaches relatively higher values for HP films. The probable reason for this amount of composition distribution could be the magnitude of rf power. For LP, the ethylene molecules, since their energies are smaller, could not interact with silane molecule and dissociate them into radicals to combine with silicon, nevertheless they mostly

interact with silane radicals, and combine with hydrogen (See chapter 4). On the other hand, for HP, energetic ethylene molecules could react with silane molecules and resultant radicals could combine to form relatively more Si-C molecules with respect to the LP case.

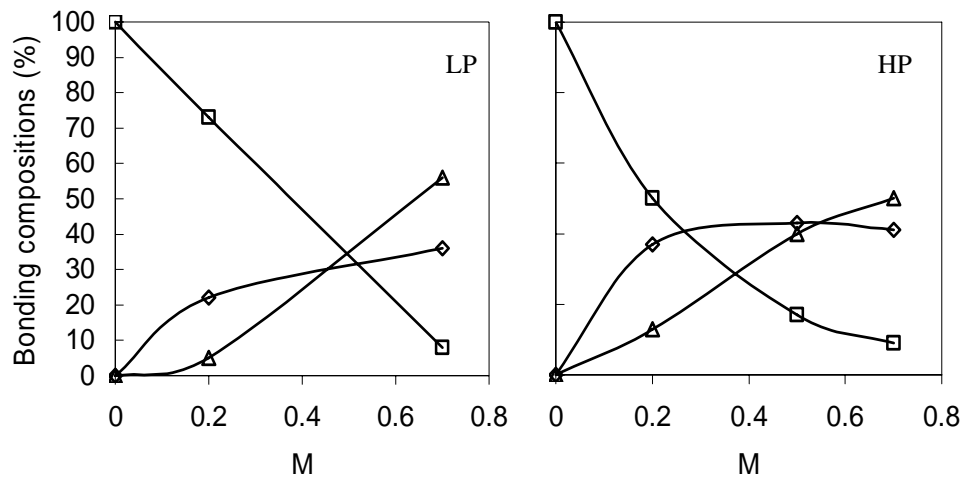


Figure 5.5. Percentage of bonding configurations as a function of gas concentration for LP and HP $a\text{-SiC}_x\text{:H}$ films. Si-Si/Si/H (squares), Si-C (diamonds), C-C/C-H (triangles).

CHAPTER 6

THE OPTICAL CHARACTERISTICS OF a-SiC_x:H FILMS

6.1 LIGHT ABSORPTION BY THIN FILMS

The light absorption in the direct energy gap of thin film crystal can be outlined in the following way. The transmission coefficient (t) and reflection coefficient (r) of an electromagnetic field through an absorbing film on a transparent substrate of semi-infinite thickness (Figure 6.1.) can be written, in terms of the transmitted (E_2^+), reflected (E_0^-) and incident (E_0^+) wave amplitudes by using Fresnel equations (Heavens, 1991).

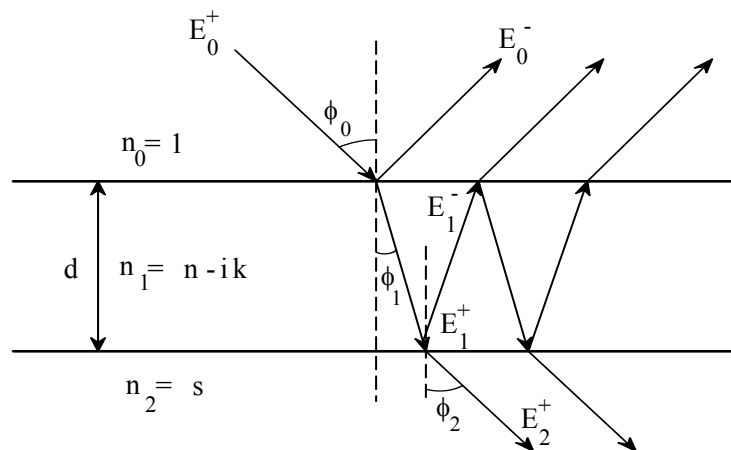


Figure 6.1. Transmission and reflection of an electromagnetic field through an absorbing film on a transparent substrate of infinite thickness.

where

$$\begin{aligned}
 A'' &= 16(n^2 - k^2)s \\
 B'' &= [(n+1)^2 + k^2][(n+s)^2 + k^2] \\
 C'' &= [(n^2 - 1 + k^2)(n^2 - s^2 + k^2) - 4k^2s]2\cos\phi - k[2(n^2 - s^2 + k^2) + 2s(n^2 - 1 + k^2)]2\sin\phi \\
 D'' &= [(n-1)^2 + k^2][(n-s)^2 + k^2], \quad \phi = \frac{4\pi n d_1}{\lambda}
 \end{aligned}$$

The transmission intensity (T_{Σ}) for the substrate alone (Figure 6.2) is the special case in which its thickness is much more than the coherence length of the light beam. Therefore, only intensities of transmitted and reflected components are taken into consideration. Thus, total transmitted intensity can be found as:

$$T_{\Sigma} = T_1 T_2 (1 + R_2^2 + R_2^4 + \dots) = \frac{T_1 T_2}{1 - R_2^2} = \frac{2s}{s^2 + 1} \quad (6.4)$$

where

$$R_2 = \frac{(s-1)^2}{s^2 + 1}$$

Finally, if the absorbing thin film is on a transparent substrate of finite thickness (Figure 6.3), considering the contribution of substrate, the transmission intensity can be expressed as (Heavens, 1991):

$$T = \frac{A''x}{B'' - C''x + D''x^2}, \quad x = \exp(-\alpha d_1), \quad \alpha = \frac{4\pi k}{\lambda} \quad (6.5)$$

where

$$\begin{aligned}
 A'' &= 16(n^2 - k^2)s \\
 B'' &= [(n+1)^2 + k^2][(n+1)(n+s^2) + k^2] \\
 C'' &= [(n^2 - 1 + k^2)(n^2 - s^2 + k^2) - 2k^2(s^2 + 1)]2\cos\phi - k[2(n^2 - s^2 + k^2) + (s^2 + 1)(n^2 - 1 + k^2)]2\sin\phi
 \end{aligned}$$

$$D'' = [(n-1)^2 + k^2][(n-1)(n-s^2) + k^2], \quad \phi = \frac{4\pi n d_1}{\lambda}$$

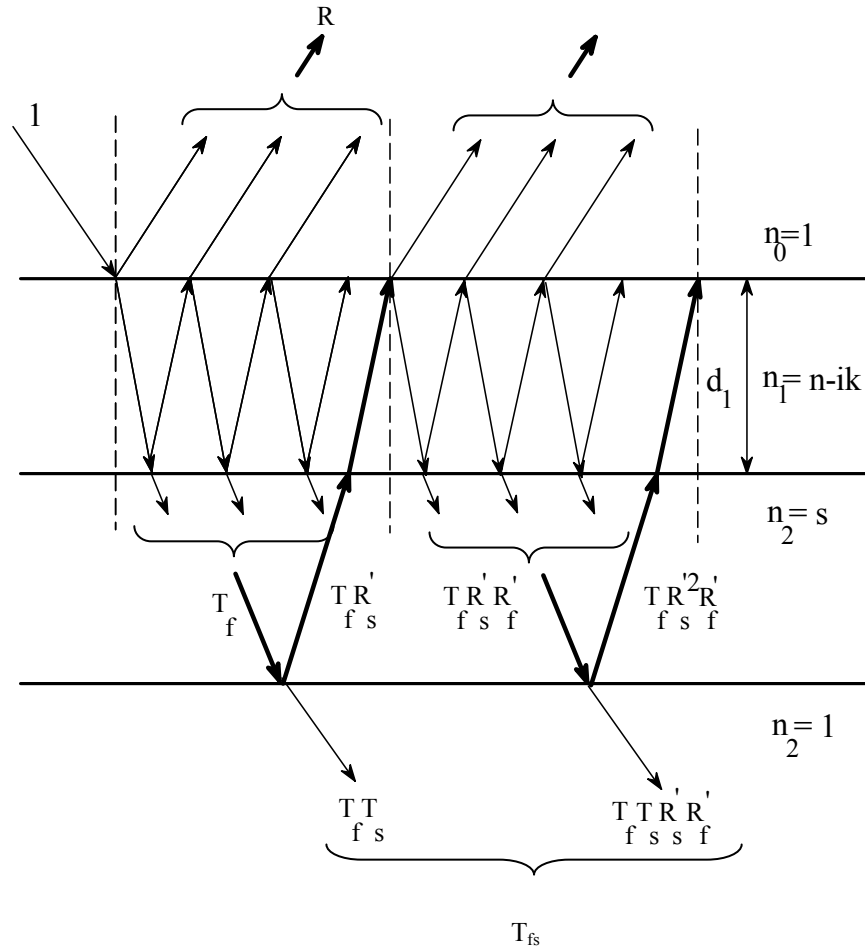


Figure 6.3. Transmission and reflection through an absorbing thin film on a transparent substrate of finite thickness.

The imaginary part of the refractive index (k) must be taken very small for the weak absorption region of the spectrum. Then, the transmission intensity reduces to the following equation.

$$T = \frac{A''x}{B'' - C''x \cos \phi + D''x^2}, \quad x = \exp(-\alpha d_1), \quad \alpha = \frac{4\pi k}{\lambda} \quad (6.6)$$

where

$$A''=16n^2s$$

$$B''=(n+1)^3(n+s^2)$$

$$C''=(n^2-1)(n^2-s^2) 2$$

$$D''=(n-1)^2 (n-1)(n-s^2), \quad \phi=\frac{4\pi n d_1}{\lambda}$$

In the absorption spectroscopy experiments, applied on an absorbing thin film on the transparent substrate of finite thickness, it is observed that, transmission intensity versus wavelength graph has interference fringes. The basic equation for these interference fringes is $2nd_1=m\lambda$, where m is an integer for maxima and half integer for minima. Substituting $x =1$ in equation 6.6:

$$T_M = \frac{2s}{s^2 + 1}, \quad \text{for maximum points} \quad (6.7)$$

$$T_m = \frac{4n^2s}{n^4 + n^2(s^2 + 1) + s^2}, \quad \text{for minimum points} \quad (6.8)$$

These two equations enable us to calculate the refractive index (n) of the film, using the equation.

$$n = \left[N + (N^2 - s^2)^{\frac{1}{2}} \right]^{\frac{1}{2}} \quad (6.9)$$

where

$$N = \frac{2s}{T_m} - \frac{s^2 + 1}{2}$$

The two adjacent maxima in the transmission intensity versus wavelength graph can be used in calculating the thickness of the film (d) for quick evaluation. This approach may give scattered results, as it is very sensitive to noise. If n_1 and n_2 are the refractive indices and λ_1 and λ_2 are the wavelengths of two adjacent maxima points the corresponding film thickness can be calculated by:

$$d = \frac{\lambda_1 \lambda_2}{2(\lambda_1 n_2 - \lambda_2 n_1)} \quad (6.10)$$

In order to determine the absorption coefficient (α), firstly, the parameter x can be calculated for maxima of interference fringes by the following equations:

$$x = \exp(-\alpha d) = \frac{F - \left[(F^2 - (n^2 - 1)^3 (n^2 - s^4)) \right]^{\frac{1}{2}}}{(n - 1)^3 (n - s^2)} \quad (6.11)$$

where

$$F = \frac{8n^2 s}{T_M} + (n^2 - 1)(n^2 - s^2)$$

Then, the absorption coefficient is easily calculated by;

$$\alpha = \frac{1}{d} \ln \left(\frac{1}{x} \right) \quad (6.12)$$

6.2 DETERMINATION OF OPTICAL ENERGY BAND GAP

The light absorption in the direct energy gap crystal is outlined above. The light absorption in the amorphous materials has some differences from the crystal case. In contrast to optical absorption in crystalline materials, the optical absorption in amorphous ones does not have sharp rise under changing light energy. This leads us to the concept of 'optical energy gap' (E_0). The

experimental determination of the optical band edge in the amorphous materials is more difficult than the determination of it in crystalline materials. Optical gaps, within the frame of effective mass approximation (square root dependence of density of state distributions around the extrema of valence and conduction bands), can be determined by two approaches: constant momentum matrix approximation (Tauc's method) (Tauc, 1966) and constant dipole matrix approximation (Cody's method) (Cody, 1982). In Tauc's and Cody's methods absorption coefficients can be defined as:

$$\sqrt{\hbar\omega\alpha} = B^{Tauc} (\hbar\omega - E_g^{Tauc}) \quad (6.13)$$

$$\sqrt{\frac{\alpha}{\hbar\omega}} = B^{Cody} (\hbar\omega - E_g^{Cody}) \quad (6.14)$$

where B^{Tauc} and B^{Cody} are the slope parameters depending on the joint DOS and momentum (dipole) matrix element. The factor B can be considered as a measure of the structural disorder, that is, high value of B indicates a smaller degree of structural disorder (Chui, 2001). According to Mott (Mott 1979), B is inversely proportional to the width of the conduction band tail. As a result, optical gaps E_g^{Tauc} and E_g^{Cody} can be determined by fitting $\sqrt{\hbar\omega\alpha}$ and $\sqrt{\frac{\alpha}{\hbar\omega}}$, to linear functions and extrapolating them to $\sqrt{\hbar\omega\alpha} = 0$ and $\sqrt{\frac{\alpha}{\hbar\omega}} = 0$, respectively. Additionally, the optical gap E_{04} , which is defined as an energy point in the absorption spectrum, where the absorption coefficient reaches 10^4 cm^{-1} , can also be determined, for comparison.

For amorphous materials, the absorption coefficient $\alpha(E)$ exponentially depends on energy, such as $\exp(\frac{E}{E_U})$ with a characteristic energy parameter E_U , called Urbach energy. The transitions from valence band tail to conduction band

are known as the ‘Urbach Edge’. Urbach energy, being a degree of average distortion, proportionally defines the width of the band tail. Accordingly, the transitions from valence band tail to conduction band are known as the ‘Urbach Edge’.

In the chapter 2, it was stated that, taking into account the independence and randomness of the local potentials, the probability of occurrence of a local potential V is reasonably expected to be a one sided Gaussian relation (Economou, 1987, O’Leary, 1997, Bacalis, 1988, Tanaka, 1999, John, 1986, O’Leary, 1995) (See chapter 2). As a result of the Gaussian potential distribution, Urbach energy can be expressed by the sum of the static disorder variance σ_s^2 , the thermal variance σ_T^2 and the compositional disorder variance σ_C^2 of the potentials, where the compositional disorder is a result of the potential fluctuations due to carbon incorporation in the film.

$$E_U = A \left[\underset{\substack{\text{STRUCTURAL} \\ \text{DISORDER}}}{\sigma_S^2} + \underset{\substack{\text{THERMAL} \\ \text{DISORDER}}}{\sigma_T^2} + \underset{\substack{\text{COMPOSITIONAL} \\ \text{DISORDER}}}{\sigma_C^2} \right] \quad (6.15)$$

where A is the proportionality factor. If the structural disorder and thermal disorder is assumed to be constant, the increase of E_U may be determined by the strength of compositional disorder. Within this approximation, for a completely random structure (uncorrelated two component alloy) for which the probabilities of finding Si-Si, Si-C and C-C bonds are x^2 , $2x(1-x)$ and $(1-x)^2$, respectively (Rovira, 1997), E_U can be given as (Skumanich, 1985, Frova, 1985).

$$E_U = C_1 + C_2 x (1 - x) \quad (6.16)$$

where

$$C_1 = A(\sigma_S^2 + \sigma_T^2), \quad C_2 x(1-x) = A\sigma_C^2.$$

6.3 ULTRAVIOLET-VISIBLE SPECTROSCOPY ANALYSIS OF a-SiC_x:H

In the analysis, the thicknesses, refractive indices and optical gaps of the films were obtained from transmittance measurements at normal incidence by using an optical characterization software (OptiChar). It has been experienced that the numerical inversion methods may result in multiple solutions. In order to avoid such an ambiguity in thickness obtained from OptiChar, the spectra are analyzed additionally by the envelop method (Manificier, 1976, Swannepoel, 1983a, 1983b). All measurements are performed as soon as (few minutes) the samples are brought out from the growth chamber in order to reduce eventual atmospheric contamination on the surfaces of the films.

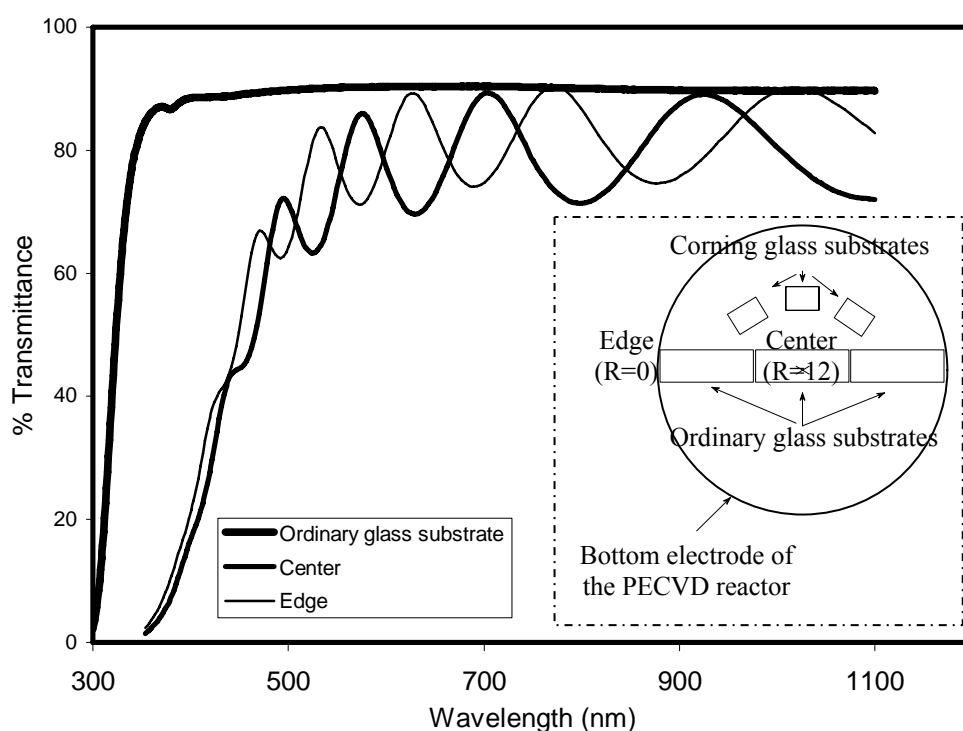


Figure 6.4. UV-Visible transmittance spectrum of ordinary glass substrate and a-SiC_x:H HP M=0.7 films deposited on ordinary glass substrates located at the center and at the edge of the bottom electrode of the PECVD reactor. The position of the substrates are illustrated in the inset where the circle represents the bottom electrode of the PECVD reactor .

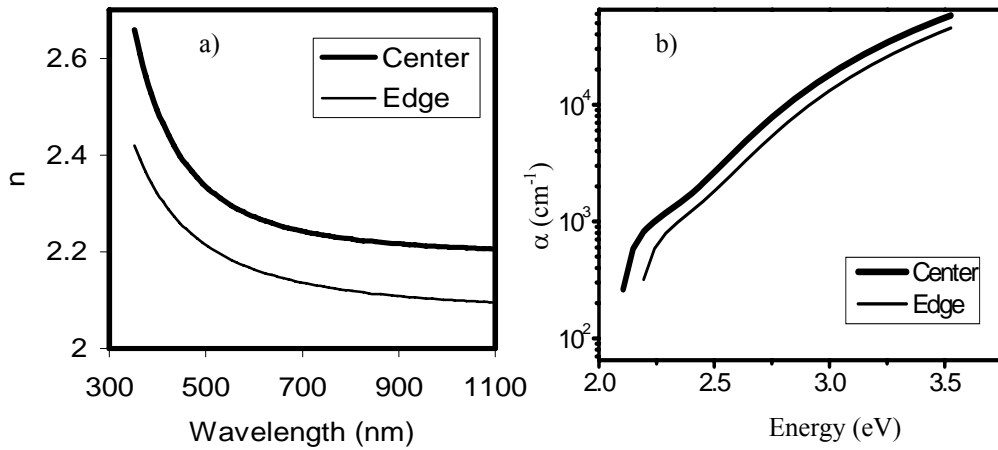


Figure 6.5.a) Refractive index as a function of wavelength, b) absorption coefficient as a function of energy for a-SiC_x:H HP M=0.7 films at the center and at the edge of the bottom electrode of PECVD reactor.

During the deposition of the a-SiC_x:H films, the ordinary glasses were placed along the radius of the bottom electrode of the PECVD reactor, in order to investigate the change in deposition rates of the a-SiC_x:H films. Typical UV-Visible transmittance spectrums for the ordinary glass substrate and a-SiC_x:H HP M=0.7 films deposited on ordinary glass substrates which are located at the center and at the edge of the bottom electrode of the PECVD reactor is presented in Figure 6.4. The higher number of fringes and the change in the amplitudes of the fringes at the edge with respect to center indicates that the thickness increases towards the edge. In Figure 6.5 refractive indices and absorption coefficients of the film are reported. The refractive index decreases towards the edge, whereas the absorption coefficient curves indicate that the optical energy band gap increases towards the edge. Corning glass substrates, which have reliable and uniform optical properties, were placed at the midway between the center and the edge of the bottom electrode, to investigate the optical properties of the films with respect to the growth parameters.

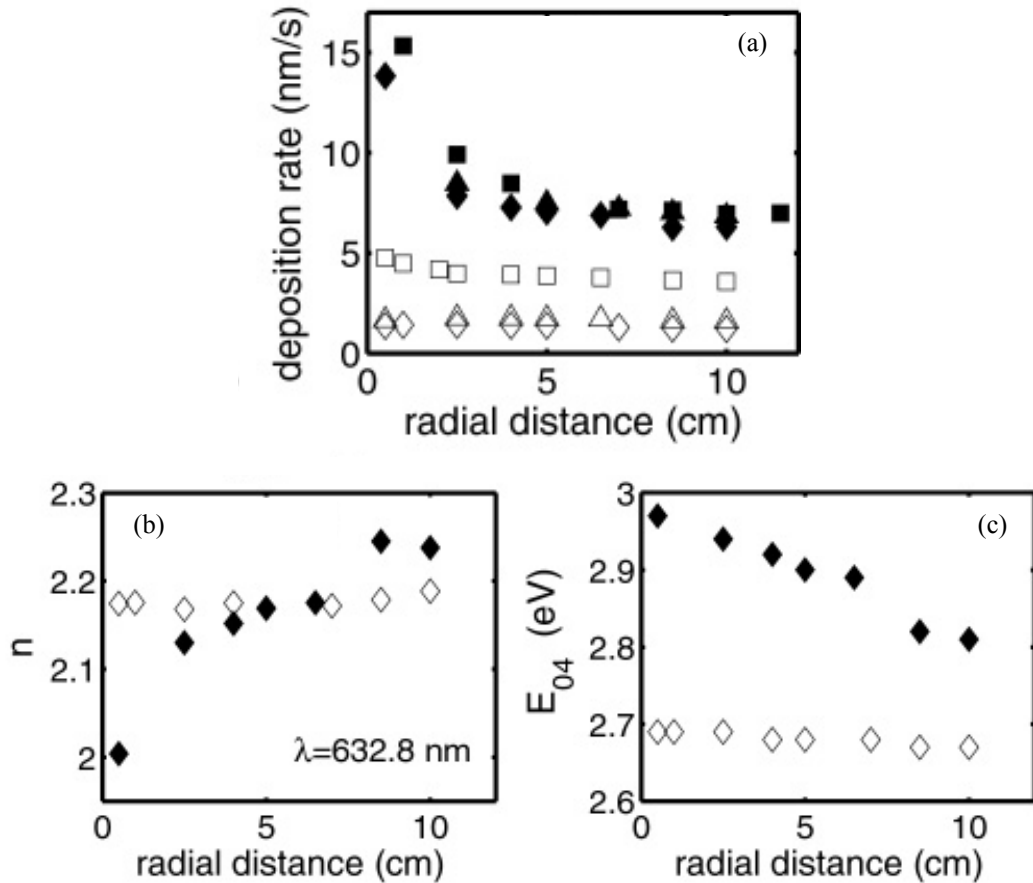


Figure 6.6. (a) The deposition rates of a-SiC_x:H films along the radial direction of the bottom electrode grown with relative gas concentrations M=0.2 (squares), M=0.5 (triangles) and M=0.7 (diamonds). (b) The refractive indices (n), and (d) E₀₄ values for the a-SiC_x:H films of M=0.7. Radial distances of about 0 cm and 12 cm correspond to the edge and the center of the electrode, respectively. Empty and full markers denote a-SiC_x:H films deposited at LP (30 mW/cm²) and HP (90 mW/cm²), respectively (Akaoglu et. al., 2006).

The change in deposition rates of the a-SiC_x:H films, as a function of the radial distance, measured from the edge of the electrode, is shown in Figure 6.6(a). Deposition rates are observed to be increasing towards the edge of the electrode for the a-SiC_x:H films deposited at higher power density (90 mW/cm²) (HP), whereas the deposition rates of the a-SiC_x:H films deposited at lower power densities (30 mW/cm²)(LP) remain constant. This inhomogeneity, due to high power density along the radial direction, is not restricted to a simple thickness

distribution, but also the refractive indices of the films deposited at HP, for the wavelength of 632.8 nm are found to be decreasing towards the edge of electrode, while no such distinguishable non-uniformity is observed for refractive indices of the LP films (Figure 6.6(b)). Similarly, optical gaps E_{04} , are evaluated along the radial distance and a uniformity in E_{04} at LP and a gradually increasing E_{04} at HP towards the electrode edge are observed (Figure 6.6(c)) Another result of this work is that there is a critical power density beyond which deposition rates, refractive indices and optical gaps of the films are not uniform along the radial direction of the bottom electrode. In other words, the carbon content of the films gradually increases towards the electrode edge beyond a critical power (Akaoglu et al., 2006).

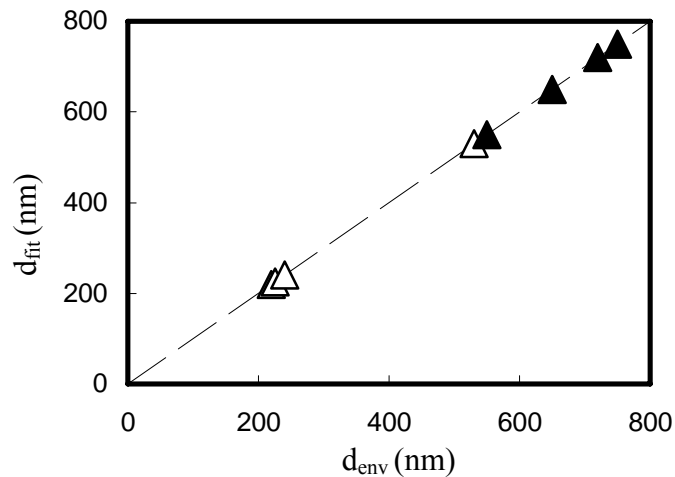


Figure 6.7. The thickness obtained from optical characterization software (d_{fit}) is plotted as a function of the thickness obtained from envelope method (d_{env}). Empty and full markers denote a-SiC_x:H films deposited at LP (30 mW/cm²) and HP (90 mW/cm²), respectively (Akaoglu et. al., 2006).

The optical properties of the films with respect to growth parameters are thoroughly analyzed by using only the transmittance data taken from the film grown on the Corning glass substrates. The result of this work is the excellent agreement obtained between the thicknesses of films grown on Corning glass

substrates, determined by both envelope method (d_{env}) and optical characterization software (d_{fit}), as shown Figure 6.7. Arithmetic average d_{av} of thicknesses d_{env} and d_{fit} is given in Table 6.1.

Table 6.1. Gas concentration and average thicknesses of a-SiC_x:H films deposited at lower (LP) (30 mW/cm²) and higher (HP) (90 mW/cm²) power densities.

	M	Film thickness d_{av} (nm)
LP	0	226.5
	0.2	523.4
	0.5	230.7
	0.7	240.8
HP	0	642.0
	0.2	548.2
	0.5	713.6
	0.7	748.9

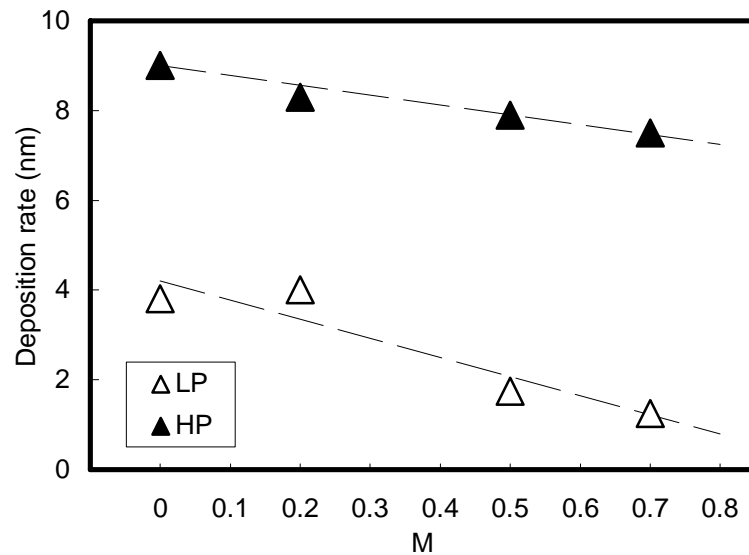


Figure 6.8. Deposition rate of a-SiC_x:H films as function of gas concentration, M (Akaoglu et. al., 2006).

In the Figure 6.8, the deposition rate of the films is plotted as a function of relative gas concentration (M). It is observed that the deposition rate decreases, as the M increases for both power densities. On the other hand, the decrease at HP is much smaller than the one at LP. Although, for low values of M, the ratios of deposition rates of HP and LP is 2.5, for higher values it reaches to 8. Besides, some slightly different behaviors have been observed for films grown with ethylene in the literature (Kuhman, 1989, Hopf, 2000).

Table 6.2. Table of optical constants and carbon content (x) of the films. The optical constants and carbon contents in literature are given as: x^a (Mui, 1987), x^b (Siebert, 1987), x^c (Sitiropoulos, 1987), x^d (Summonte, 2004), x^e (Ambrosone, 2002, Sussman, 1981) and the carbon content obtained by XPS measurements are given as 'x (XPS)'. The average carbon content $\langle x \rangle$ of a-SiC_x:H films were determined by comparing the corresponding energy and refractive index values with the values given in the literature. Where σ is their standard deviations (Akaoglu et. al., 2006).

M	0.2 (LP)	0.2 (HP)	0.5 (LP)	0.5 (HP)	0.7 (LP)	0.7 (HP)						
E_g^{Tauc} (eV)	2.03	2.03	2.40	2.28	2.55	2.71						
E_{04} (eV)	2.18	2.18	2.42	2.48	2.60	2.91						
n_1 ($\lambda=620$ nm)	3.21	3.18	2.63	2.49	2.29	2.07						
n_2 ($\lambda=820$ nm)	2.99	2.97	2.50	2.40	2.21	2.04						
n_3 ($\lambda=1100$ nm)	2.91	2.89	2.43	2.36	2.16	2.02						
	E_{04}, E_g	n	E_{04}, E_g	n	E_{04}, E_g	n	E_{04}, E_g	n	E_{04}, E_g	n		
x^a	0.22	0.15	0.22	0.15	0.32	0.32	0.33	0.35	0.38	0.44	0.61	0.54
x^b	0.20	0.20	0.20	0.20	0.40	0.43	0.45	0.47	0.50	0.52	0.57	0.62
x^c	0.15	0.17	0.15	0.17	0.39	0.37	0.45	0.40	0.48	0.48	0.53	0.53
x^d	0.20	0.15	0.20	0.15	0.36	0.38	0.38	0.40	0.44	0.50	0.54	0.61
x^e	0.22	0.19	0.22	0.19	0.38	0.30	0.36	0.32	0.46	0.44	0.56	0.50
$\langle x \rangle$	0.20	0.17	0.20	0.17	0.37	0.36	0.39	0.39	0.45	0.48	0.56	0.56
σ	0.028		0.028		0.041		0.053		0.041		0.041	
x (XPS)	0.17		0.21		-		0.42		0.48		0.59	

In Table 6.2, the experimentally obtained values of Tauc and E_{04} optical gaps and refractive indices for various wavelengths of the films are reported together with the values obtained from literature. This is a consequence of more carbon incorporation in the HP films. Additionally, the carbon contents (x) of the

films are determined by comparing the optical gaps and refractive indices separately with the values published in the literature (Mui, 1987, Siebert, 1987, Sitiropoulos, 1987, Summonte, 2004, Ambrosone, 2002, Sussman, 1981) as shown in Table 6.2. In these reference studies, the films are deposited by PECVD at substrate temperatures of 250 °C (Mui, 1987, Siebert, 1987, Sitiropoulos, 1987), 200 °C (Ambrosone, 2002) and 300 °C (Sussman, 1981) with CH₄ (Siebert, 1987, Sitiropoulos, 1987, Ambrosone, 2002), C₂H₂ (Mui, 1987) and C₂H₄ (Sussman, 1981) gas sources. Hydrogen concentrations in the films strongly depends on the temperature, thus, especially reference film, which was deposited at substrate temperature of 250 °C were selected as a reference for reliable comparison. The films studied in reference (Summonte, 2004) were produced with approximately the same hydrogen dilution level as we applied for our films. Since our films are mainly silicon rich, the effects of hydrogen dilution on the hydrogen content of the films, in turn, on the optical gaps and refractive indices of the films are assumed to be small (Summonte, 2004, Giorgis, 1997) and the quite narrow distribution of estimated x values also supports this assumption. This kind of statistical approach may be envisaged as a reliable alternative technique for a first order evaluation instead of using an empirical relation for x. In this approach, the final x compositions are determined by at least 10 independent comparisons for each film. The estimated x by using refractive indices are the same with the ones obtained by using the optical gaps. Additionally, almost similar carbon contents are obtained with UV-Visible spectroscopy and XPS, which were reported in chapter 5. In Figure 6.9, carbon content (x) of the films is plotted as a function of M. The variation of x as a function of M is approximately linear and the slope seems considerably increased by the applied rf power. Form the Table 6.2, it is observed that, the refractive indices decreases, as the carbon content in the film increases. Furthermore, for the same carbon content, refractive indices of the HP films are smaller than ones of the LP films.

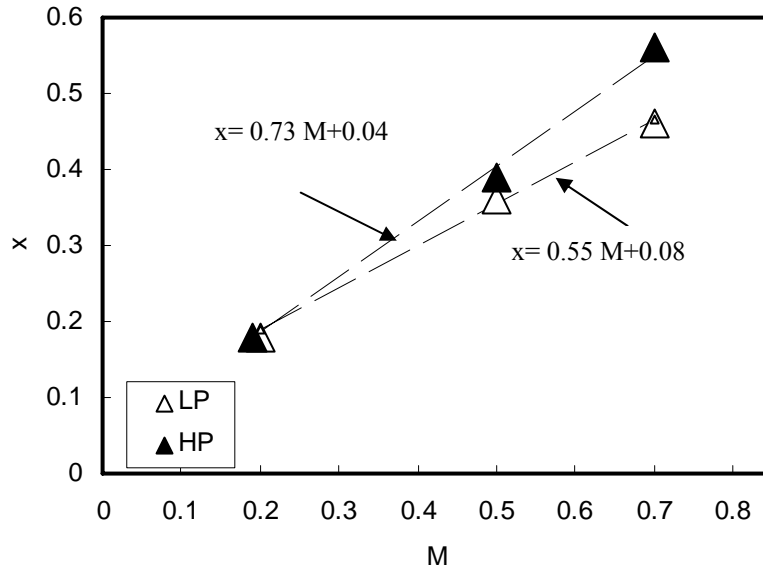


Figure 6.9. Carbon content (x) of $a\text{-SiC}_x\text{:H}$ films as function of gas concentration M (Akaoglu et. al., 2006).

Although the deposition of low carbon content films might be clearly explained by the incorporation of SiH_3 precursor to the hydrogen terminated growing surface under ionic bombardment, the growth mechanism of carbon rich films is more complex and cannot be explained by a single precursor radical. Nevertheless, the formation and amount of dangling bonds on the growing film surface might be considered as an essential part, which determines the deposition mechanism with various aspects. The measured deposition rates of the HP films might be due to cooperative participation of ions and radicals in the growth to form chemical bond by overcoming the activation barrier by the energy supplied by ions impinging on the growth surface. On the other hand, since the deposition rates of the HP films quite weakly depend on the relative C_2H_4 gas concentration in comparison to the LP films, it seems more effective to produce carbon based radicals at HP, reaching the level of silicon based radicals. Stronger ion bombardment at high power densities might result in higher density of dangling bonds regardless of type of bonds on the growing surface. Therefore, whether the growing surface is formed by Si-C and C-C bonds, impinging ions might be

sufficient to supply required energy to create dangling bonds. Optical properties of films, grown in capacitively coupled rf discharges at HP, are found to be insensitive to the hydrocarbon source gases due to the broad ion energy distributions at HP (Swhartz, 1996). The observed difference between deposition rates of the LP and HP films is also reasonable within this frame.

Although all deposition parameters are kept constant during the deposition process, the variation of film properties along the bottom electrode might come out due to eventual non-uniform distribution of carbon bearing precursors, whose formation takes more or less time after the gas molecules enter the central region of the plasma. The enhanced deposition rates towards the reactor edge might be interpreted by the increased density of unsaturated radicals towards the reactor edge. However, non-uniform hydrogen incorporation might be an alternative explanation because it has been found that surface loss probability of CH_3 radical becomes much higher in the case of large atomic hydrogen flux towards the surface (Kaudell, 2000, 2002). Decrease in refractive index and increase in the optical gap towards the reactor edge might occur due to the increase in atomic carbon fraction in the film. However, it should be also noted that such a change might be due to structural changes in the films along the radial direction. On the other hand, non-uniform deposition parameters might occur due to the design or geometry of the deposition system, which might lead to non-uniformity in the rf-voltage and pressure. Within this frame, the increase in deposition rate towards the reactor edge suggests an increase in plasma density and thus, an increase in rf-voltage. Besides, decrease in pressure leads to an increase in the voltage drop in the sheath region, which may raise kinetic energy of positive ions towards the growing surface.

E_g^{Tauc} , E_g^{Cody} and E_{04} are plotted as a function of x as shown in Figure 6.10(a). It is observed from the Figure 6.10(a) that, the increase in the carbon content in the films, results in an increase in the optical gaps for both LP and HP films. This increase is probably due to the increasing number of strong Si-C bonds (Robertson, 1992a, 1992b). On the other hand, it could also be due to the

increased number of Si-H bonds. But, this last contribution remains limited, because of the reason that, the maximum change of valence band tail upon hydrogenation in silicon rich alloys is about 0.7 eV (Rovira, 1997). Therefore, the increase in the optical gaps should be mostly originated from replacements of Si-Si bonds by Si-C bonds in the structure. In the Figure 6.10(a), the slope parameters B^{Tauc} and B^{Cody} are plotted, as a function of x , as an inset. It is observed that, B^{Tauc} and B^{Cody} decrease by increasing carbon content, especially for the HP films.

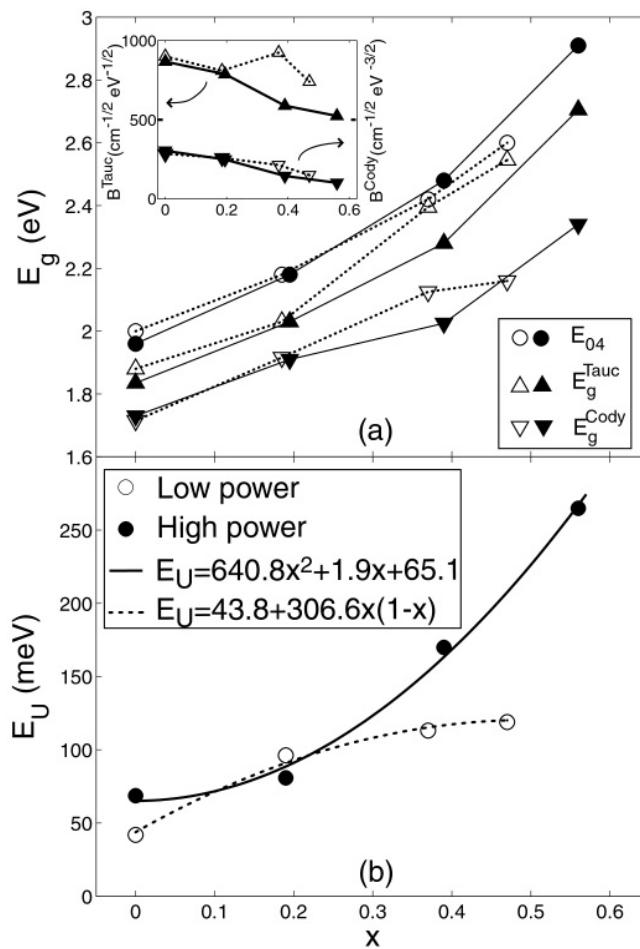


Figure 6.10. (a) Optical gaps E_g^{Tauc} , E_g^{Cody} and E_{04} , and as an inset, the slope parameters B^{Tauc} and B^{Cody} are plotted as function of carbon content (x) for a-SiC_x:H films at LP (empty markers) and HP (full markers). (b) Urbach energies E_U are plotted as function of carbon content (x), for a-SiC_x:H films, together with suitable representative fittings. (Akaoglu et. al., 2006).

In the Figure 6.10(b), the Urbach The Urbach energies (E_U) are plotted as a function of carbon content (x). It is observed that, E_U increases significantly by the increase in x for the HP films. Besides, for the films grown at LP, E_U exhibits an appreciable increase at lower values of x , while it does not significantly change at larger values. The rapid increase of E_U at HP might be due to the high deposition rate of the films. Since atoms are expected to have less time to reach thermodynamically preferred lattice positions in comparison to the films grown at low deposition rates (Aspnes, 1986), films would probably be structurally more disordered at higher deposition rates. The experimentally determined E_U of LP films, can be represented by a function $43.8+306.6x(1-x)$ (Equation 6.16) (Figure 6.10(b)). For the LP films, the contribution of structural and thermal disorder to the Urbach energy is found to be 43.8 meV. Whereas the compositional disorder variance is found to be 306.6 meV. On the other hand, Urbach energy of the HP films can be represented by a function $640.8x^2+1.9x+65.1$, which can be alternatively written in terms of x^2 , $(1-x)^2$ and $2x(1-x)$. Accordingly, it can be suggested that, the HP films involves C-C bonds. The strong increasing trend of Urbach energy for the HP films with respect to the LP films might be due to presence of C-C bonds, which can be seen as an additional source of disorder besides the disorder due to Si-C bonds. It should be kept in mind that, as x approaches 0.5, solid may start to be consisting of all three types of covalent 2-center hybrid σ -like sp , sp^2 and sp^3 bonds, together with π -like delocalized (or multicenter) bonds, which may lead to relaxation of network (Zanatta, 1998)(See capter 2).

CHAPTER 7

VIBRATIONAL CHARACTERISTICS OF a-SiC_x:H FILMS

7.1 MOLECULAR VIBRATIONS OF a-SiC_x:H FILMS

The vibration characteristics of a-SiC_x:H are closely related to its bonding configurations of atoms. Thus, this analysis directly gives information about the structure of the deposited a-SiC_x:H films.

For a molecule of N atoms, there are 3N degrees of freedom, corresponding to the three independent coordinates of each of the N atoms. Three of these are taken up by the translations of the entire molecule along the x-, y- and z-axes and another three by the rotation of the molecule about the three principal axes of inertia. Linear molecules have only two rotational degrees of freedom, because the moment of inertia along the molecular axis is zero. The number of remaining vibrational degrees of freedom n is identical to the number of fundamental vibrations, that is (Fadini, 1989, Kittel, 1996):

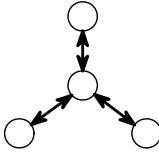
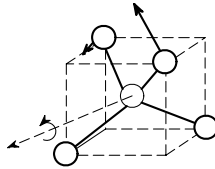
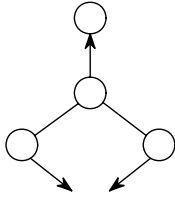
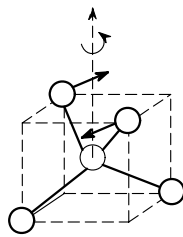
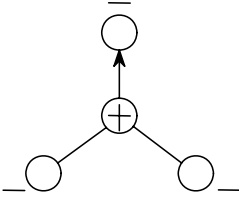
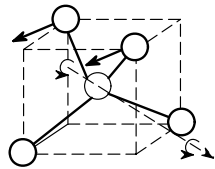
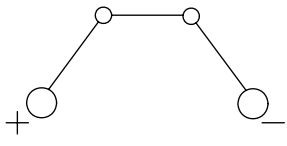
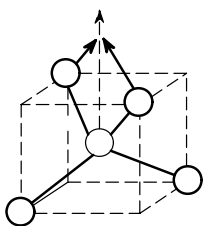
$$N = 3N - 3 - 3 = 3N - 6 \text{ for a non-linear molecule and}$$

$$N = 3N - 3 - 2 = 3N - 5 \text{ for linear molecule.}$$

The description of the vibrational degrees of freedom is not based on the Cartesian coordinates, but on 'internal' coordinates, which corresponds to bond lengths and angles. The normal modes of vibration are defined as a molecular motion in which all the atoms move in phase and with the same frequency. Additionally, vibrational motion does not cause a translation or rotation of the

molecule as a whole and each normal mode of vibration can be excited independently. Vibrations are described by so called normal coordinates, which are derived from the masses and relative moments of the atoms involved. During a vibration, the bond distance and the angle between the atoms of the molecule change periodically. Accordingly, four main types of vibrations can be distinguished (Table 7.1).

Table 7.1. The basic types of vibration and the special types of bending vibration.

Types of vibration		Schematic	Special type of bending vibration
Stretching vibrations (ν)			 Rocking
Bending vibrations	In-plane (δ)		 Twisting
	Out-of-plane (γ)		 Wagging
Torsion vibrations (τ)			 Scissoring

a) Stretching vibrations (ν): Only bond lengths are changed.

b) In-plane bending vibrations (δ): Only bond angles are changed.

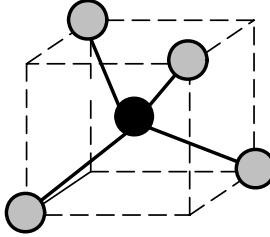
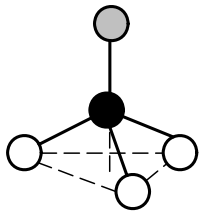
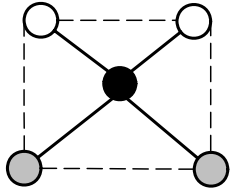
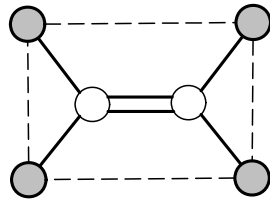
c) Out-of-plane bending vibrations (γ): Only bond angle of an atom changes through a plane defined by at least three neighboring atoms.

d) Torsion vibration (τ): A dihedral angle, that is the angle between two planes, which have one bond in common, is changed.

The frequency of these four types of vibration decreases in order $\nu > \delta > \gamma > \tau$. For larger molecules special types of vibration, which can be derived from these basic types, can also occur. For example, the bending vibrations could be further classified into rocking, twisting, wagging and scissoring. Furthermore, vibrations can be classified by symmetry. Symmetric vibrations are the ones that the symmetry of the molecule is retained throughout, and the asymmetric vibrations are the ones that one or more of the symmetry elements of the molecule vanish during the vibration. Also for highly symmetric molecules degenerate vibrations could occur.

The symmetry of the molecules that could occur in a-SiC_x:H films, which are determined by using group theory, represented in Table 7.2. For silicon rich a-SiC_x:H films σ -bonded molecules belonging mostly to T_d, C_{3v}, C_{2v} point groups and for C rich a-SiC_x:H films, in addition to the σ -bonded molecules, π -bonded carbon molecules belonging to D_{2h} point group are possibly occurring symmetry groups (Cotton, 1990).

Table 7.2. The possible geometric structures of ordinary and carbon rich a-SiC_x:H molecules.

Si rich a-SiC _x :H	Si _{4-n} -Si-H _n	<u>Symmetry operators:</u> E, 8C ₃ , 6σ _d , 6S ₄ , 3S ₄ ² ≡3C ₂ <u>Point group:</u> T _d	
	Si _{4-n} -C-H _n C _{4-n} -Si-H _n C _{4-n} -C-H _n	<u>Symmetry operators:</u> E, 2C ₃ (z), 3σ _v <u>Point group:</u> C _{3v}	
		<u>Symmetry operators:</u> E, C ₂ (z), σ _v (xz), σ _v (yz) <u>Point group:</u> C _{2v}	
C rich a-SiC _x :H	C ₂ H ₄	<u>Symmetry operators:</u> E, σ(xy), σ(xz), σ(yz), i, C ₂ (z), C ₂ (y), C ₂ (x) <u>Point group:</u> D _{2h}	

(○:C, ●:Si or C, ◐:H)

7.2 FOURIER TRANSFORM INFRARED SPECTROSCOPY ANALYSIS OF a-SiC_x:H FILMS

Fourier transform infrared spectroscopy (FTIR) enables us to analyze the vibrational characteristics of a-SiC_x:H films by the interaction between phonons and radiation in the IR region.. The corresponding absorption coefficient α is

evaluated from the transmission data, which are measured by a single-beam spectrum technique. In this technique, the instrument has only one beam and hence background and the transmission spectra cannot be measured simultaneously. Therefore, background spectrum is generally taken with no sample or only substrate placed in the sample holder and then a spectrum is measured by placing the sample in the holder. Finally, the true transmittance (T) is obtained by the ratio of the measured spectrum (I_s) and background (I_0):

$$T = \left(\frac{I_s}{I_0} \right)_\nu \quad (7.1)$$

where I_s is the instrument response function with the sample, and I_0 is the instrument response function without the sample for each frequency, ν . It is known that amount of absorption of incident radiation is determined by $\ln(T)$, if no reflection occurs at the interfaces like air-film, film-substrate and substrate-air. For a first approximation absorption coefficient (α) can be determined easily by,

$$\alpha = -\frac{1}{d} \ln(T) \quad (7.2)$$

FTIR spectroscopy indeed depends on the transmission or reflection properties of the film; i.e. the film thickness (d), refractive index (n). In order to correlate the FTIR data measured from each film with different thickness and different refractive index, they should be normalized by appropriate corrections. Therefore, transmission and reflection electromagnetic field through absorbing film on a transparent substrate should be studied.

The transmission intensity (T) of an absorbing thin film-substrate system was outlined in the chapter 5, by using Fresnel equations. Similarly for FTIR the transmission is given by Figure 7.1 (Heavens, 1991, Stallhofer, 1983);

$$T = \frac{(1 - R)^2 e^{-\alpha d}}{1 - R^2 e^{-2\alpha d}} \quad (7.3)$$

$$R = \frac{(n - 1)^2 + k^2}{(n + 1)^2 + k^2} \quad (7.4)$$

where R is the reflection, d is the film thickness, α is the absorption coefficient and k is the extinction coefficient. The term $1/(1 - R^2 e^{-2\alpha d})$ in equation 7.3. is a consequence of the multiple reflections in the film (Figure 7.1) (Stallhofer, 1983).

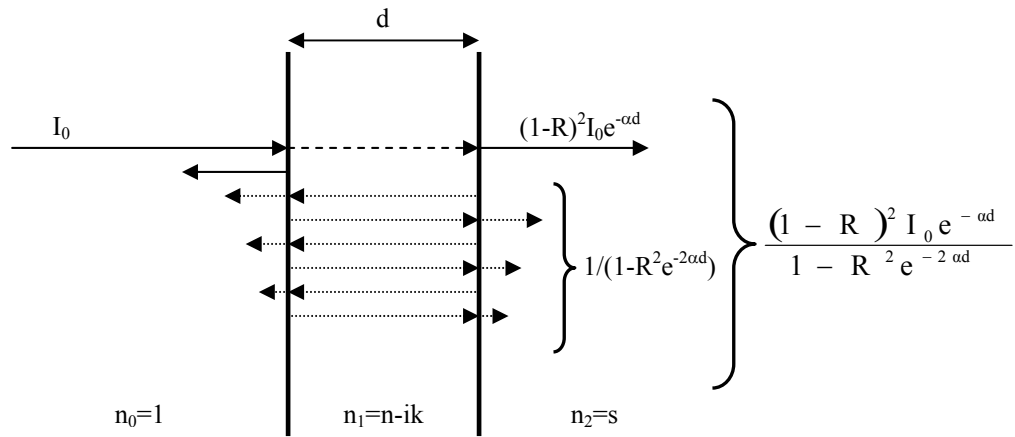


Figure 7.1. Transmission and reflection of an electromagnetic field through an absorbing film on a transparent substrate of infinite thickness.

The absorption coefficient α is equal to:

$$\alpha = \frac{4\pi k}{\lambda} \quad (7.5)$$

The permittivity ($\epsilon(\omega)$) of materials generally depends on the frequency of the electric field and can be written in terms of real (n) and complex (k) part of the index of the film as,

$$\varepsilon(\omega)=2nk=2nc\frac{\alpha(\omega)}{\omega} \quad (7.6)$$

where n is assumed to be independent of ω . Taking the integral of $\varepsilon(\omega)$ around ω_T , the concentration of the oscillator may be obtained (Fadini, 1989):

$$\int \varepsilon(\omega)d\omega = 2nc \int \frac{\alpha(\omega)}{\omega} d\omega = \frac{Ne^{*2}\beta}{\varepsilon_0 M_r} \int_0^{\infty} \frac{\omega d\omega}{(\omega_T^2 - \omega^2)^2 + \beta^2 \omega^2} \quad (7.7)$$

$$N=A \int \frac{\alpha(\omega)}{\omega} d\omega, \quad A=\frac{4\varepsilon_0 \omega_T M_r nc}{\pi e^{*2}} \quad (7.8)$$

where ε_0 is the permittivity of the vacuum, e^* is the effective mass, N is the concentration of ion pairs and M_r is the reduced mass of the ion pairs. If the exponential term in the equation 7.3 is taken as the unknown term, the bigger root of the quadratic equation gives us the absorption coefficient in the following way:

$$e^{-\alpha d} = \frac{-(1-R)^2 + (1-R)^2 \sqrt{1 + \frac{4T^2 R^2}{(1-R)^2}}}{2R^2 T} \quad (7.9)$$

Finally, the minus logarithm of the exponential term is divided by the thickness of the corresponding films, which are ranging from 200-750 nm, to obtain the absorption coefficient.

$$\alpha = -\frac{\ln(e^{-\alpha d})}{d} \quad (7.10)$$

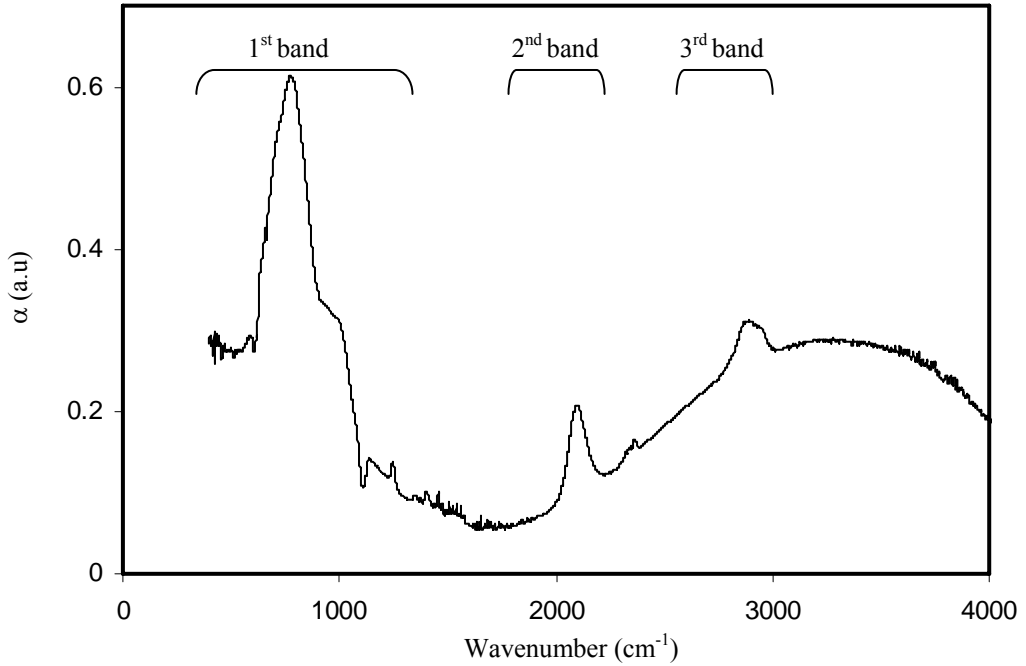


Figure 7.2. The FTIR spectrum obtained from a-SiC_x:H HP M=0.7 film.

FTIR measurements is performed at 4 cm^{-1} resolution and processed by averaging the results of 32 measurements. The typical FTIR spectra of HP a-SiC_x:H film with $x=0.56$ ($M=0.7$), is given in Figures 7.2. The spectra is mainly includes 3 absorption bands in the wavenumber ranges of $500\text{-}1500 \text{ cm}^{-1}$ (First band), $1900\text{-}2200 \text{ cm}^{-1}$ (Second band) and $2800\text{-}3000 \text{ cm}^{-1}$ (Third band). The first band mainly consists of eight different vibrational modes, the second band consists of three vibrational modes and finally the third band consists of six vibrational modes. The deconvolutions of these three bands for HP and LP a-SiC_x:H films are given in Figure 7.3 and 7.4 and the list of corresponding vibrational modes are presented in Table 7.3.

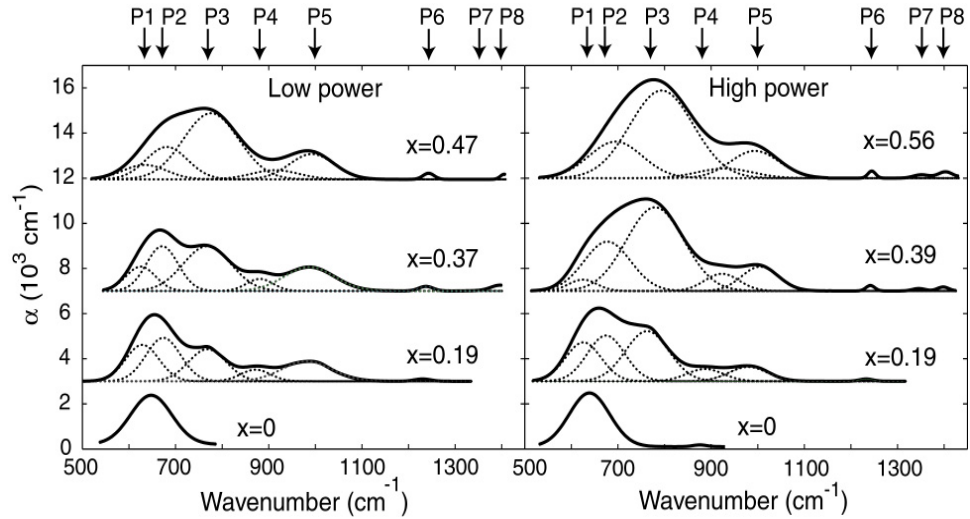


Figure 7.3. First FTIR absorption band of a-SiC_x:H thin films deposited at lower (30 mW/cm²) (LP) and higher power densities (90 mW/cm²) (HP) with deconvolutions of the peaks according to the assignments given in Table 7.3 (Akaoglu et. al., 2006).

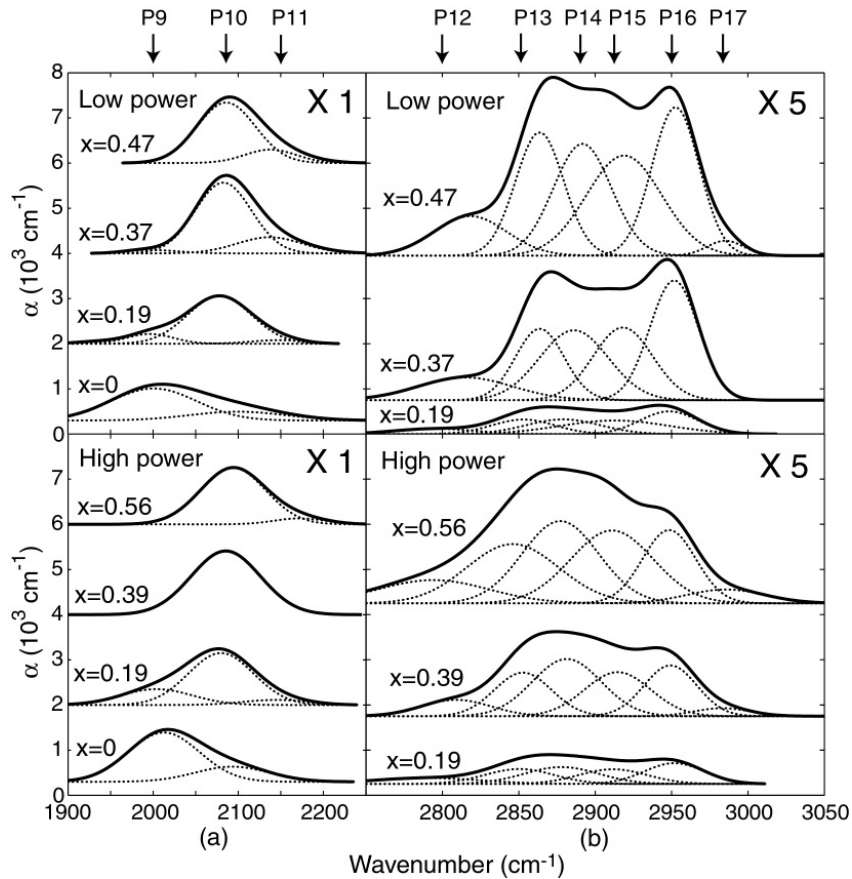


Figure 7.4. (a) Second and (b) third FTIR absorption band of a-SiC_x:H thin films deposited at lower (30 mW/cm²) (LP) and higher power densities (90 mW/cm²) (HP) with deconvolutions of the peaks according to the assignments given in Table 7.3 (Akaoglu et. al., 2006).

Table 7.3. Absorption peaks of different molecular vibrational in FTIR spectra of a-SiC_x:H films.

Peak No:	Wavenumber (cm ⁻¹)	Bond type and mode of vibration
P1	640	Si-H, Wagging (Ferreira, 2000, Catherine, 1983, Rovira, 1997)
P2	670	Si-H _n Wagging (Katayama, 1981, Demichelis, 1992, McKenzie, 1985, Swaaij, 1994, Bullot, 1987) Si-C Stretching (Swaaij, 1994, Bullot, 1987, Herremans, 1992, Weider, 1979)
P3	770	Si-C Stretching (Ferreira, 2000, Rovira, 1997, Katayama, 1981, Demichelis, 1992, Li, 1991, Leo, 1993, Lin, 1998, Demichelis, 1995) Si-CH ₃ Rocking and/or Wagging (Demichelis, 1992, Swaaij, 1994, Bullot, 1987, Weider, 1979, Lin, 1998, Demichelis, 1995)
P4	850-900	(Si-H ₂) _n Bending (Rovira, 1997, Bullot, 1987, Tawada, 1982)
P5	1000	C-H _n Wagging and/or rocking (Ferreira, 2000, Rovira, 1997, Katayama, 1981, Demichelis, 1992, Swaaij, 1994, Bullot, 1987, Leo, 1993)
P6	1245	Si-CH ₃ , Bending (symmetric) (Ferreira, 2000, Bullot, 1987, Weider, 1979, Tawada, 1982)
P7	1350	Si-CH ₃ , Bending (asymmetric) (Bullot, 1987, Weider, 1979) C-H ₂ Wagging (Bullot, 1987)
P8	1400	C-H ₂ , Bending, Scissoring (Bullot, 1987)
P9	2000	Si-H, Stretching (Rovira, 1997, demichelis, 1992, Swaaij, 1994, Weider, 1979, Tawada, 1982, Lucovsky, 1979)
P10	2090 2060-2100	Si-H ₂ , Stretching (Katayama, 1981, Demichelis, 1992, Swaaij, 1994, Tawada, 1982, Lucovsky, 1979) CSi-H, Stretching (Katayama, 1981, Demichelis, 1992, Swaaij, 1994, Tawada, 1982, Lucovsky, 1979, Weider, 1979)
P11	2150	CSi-H ₂ , Stretching (Tawada, 1982, Agrawal, 1989)
P12	2800	C-H, Stretching (Rovira, 1997, Katayama, 1981, Bullot, 1987, Tawada, 1982)
P13	2850	C-H ₂ , Stretching (symmetric) (Ferreira, 2000, Katayama, 1981, Bullot, 1987, Li, 1991, Demichelis, 1995)
P14	2880	C-H ₃ , Stretching (symmetric) (Katayama, 1981, Bullot, 1987, Weider, 1979, Li, 1991, Lin, 1998, Demichelis, 1995)
P15	2910	C-H ₂ , Stretching (asymmetric) (Katayama, 1981, Bullot, 1987, Weider, 1979, Li, 1991, Demichelis, 1995)
P16	2950	C-H ₃ , Stretching (asymmetric) (Katayama, 1981, Bullot, 1987, Weider, 1979, Li, 1991, Lin, 1998, Demichelis, 1995)
P17	2970	C-H, C-H ₂ , Stretching (sp ²) (Demichelis, 1995, Robertson, 2002)

In Figure 7.3, the absorption peaks beyond 700 cm⁻¹ start to appear for both power densities as carbon is incorporated in the films. Especially, the vibration mode at around 770 cm⁻¹, labeled as P3 in Figure 7.3, becomes dominant absorption peak so that it confirms enhanced Si-C bond density as x increases. In this respect, relative Si-C bond density is found to increase with RF power for the same x, depicted in Figure 7.5(a) (Ambrosone, 2000, 2003). The

gradual increase in full width at half maximum (FWHM) of this peak, given in Figure 7.5(b), points that disordered structure is mainly related to incorporation of C atoms (Foti, 2001, Losurdo, 2005).

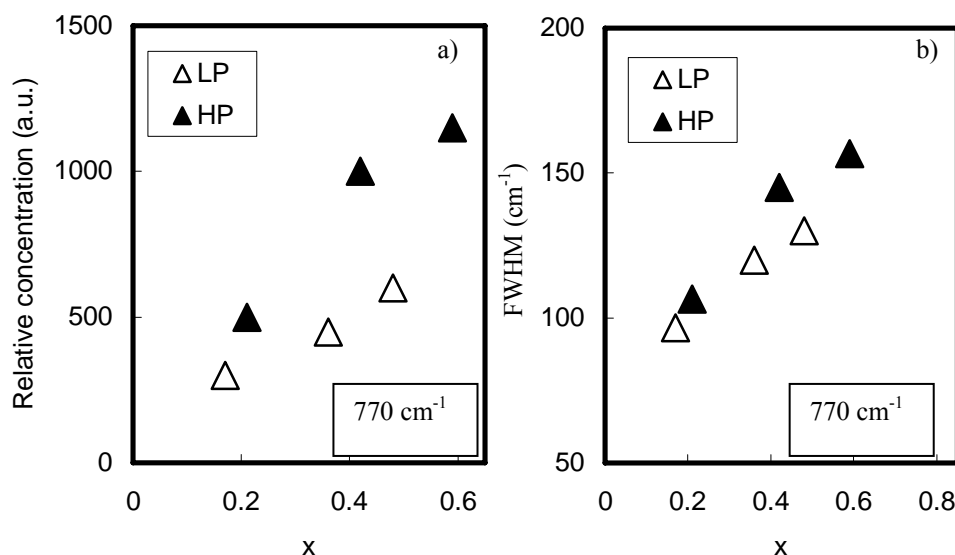


Figure 7.5. (a) Concentration of the vibration mode and (b) FWHM of the absorption peak, at 770 cm⁻¹ are plotted as a function of carbon content (x). Empty markers denote LP films and full markers denote HP films (Akaoglu et. al., 2006).

The concentration of Si-H wagging mode at about 640 cm⁻¹ abruptly decreases and tends to zero, as x increases (Figure 7.6). This behavior may misleadingly be envisaged, as an elimination of Si-H bonds in the film structure, if one disregards the fact that the Si-H stretching modes (of wavenumbers 2000-2150 cm⁻¹) are attenuated much more smoothly, as x increases. A possible explanation might be as follows for removing this controversy. The relative concentration of the peaks seen at around 670 cm⁻¹ are observed to be decreasing, as x increases. This composite peak might contain Si-H wagging mode, whose frequency would be shifted from 640 cm⁻¹ to 670 cm⁻¹, due to replacement of Si neighboring atoms with carbon atoms, as their content in the films increases. For supporting this interpretation, the sum of the concentrations of these two peaks is reported in the Figure 7.6.

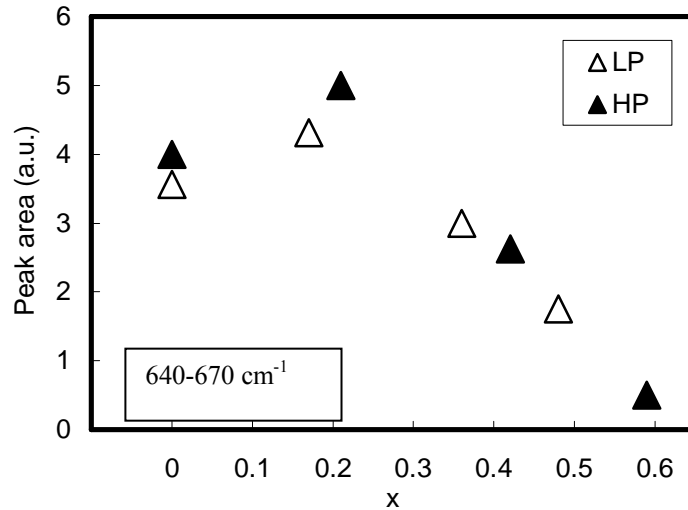


Figure 7.6. The sum of concentrations of the vibrational modes at about 640 cm^{-1} and 670 cm^{-1} is plotted, as a function of carbon content (x). Empty markers denote LP films and and full markers denote HP films (Akaoglu et. al., 2006).

The concentration of Si-H wagging mode (P1) at a wavenumber of about 640 cm^{-1} abruptly decreases and tends to zero as x increases, depicted in Figure 7.3. This may be misleadingly envisaged as elimination of Si-H bonds, if one disregards much more smooth decrease in the density of Si-H stretching modes. The relative concentrations of the peaks at around 670 cm^{-1} are also observed to have decreasing tendency as x increases, in contrast to widely adopted assignment to the Si-C stretching mode. Therefore, the sum of the concentrations of these two peaks is compared to that of Si-H_n stretching modes in the Figure 7.7. The concentrations of both modes are found to be same and become maximum for the films with $x\sim 0.3$, similar to the results given in reference (Chew, 2002). Since these peaks are located at different wavenumbers and have different oscillator strengths, the concentrations are determined by using the proportionality constants; $A_{640} = 2.1 \times 10^{19}\text{ cm}^{-2}$, $A_{2000} = 9.0 \times 10^{19}\text{ cm}^{-2}$ and $A_{2100} = 2.2 \times 10^{20}\text{ cm}^{-2}$ found for a-Si:H films (Langford, 1992). The proportionality constant A_{670} of the peak at 670 cm^{-1} is calculated as $2.5 \times 10^{19}\text{ cm}^{-2}$, by assuming the same change in the oscillator strength of stretching mode. As a result, the

composite peak P2 is attributed to Si-H wagging mode whose frequency is shifted from 640 cm^{-1} to 670 cm^{-1} ((Ambrosone, 2000, 2003).

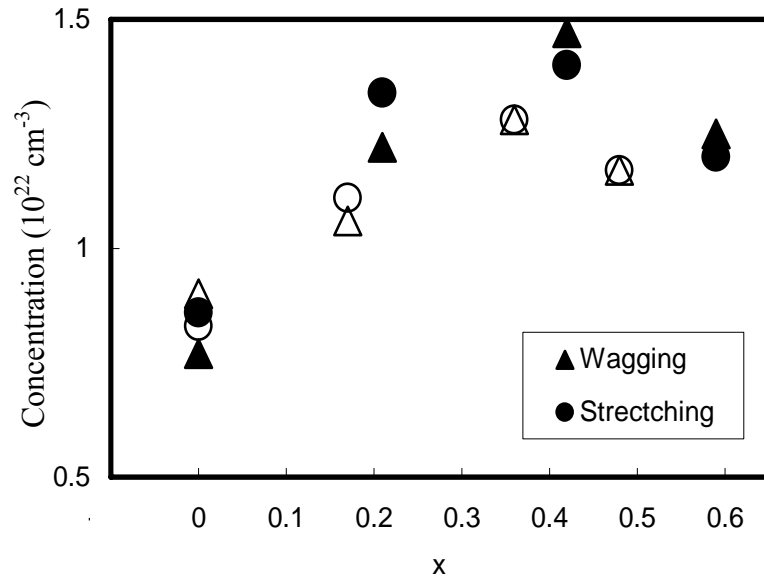


Figure 7.7. Carbon content influence on the sum of concentrations of wagging and stretching vibration modes of Si-H_n bonds. Empty markers denote LP films and full markers denote HP films (Akaoglu et. al., 2006).

In the region between $2000\text{--}2100\text{ cm}^{-1}$, the absorption peak at 2000 cm^{-1} assigned to the Si-H stretching mode. This peak disappears as carbon is incorporated in the films and replaced by a peak of substantial amount at about 2090 cm^{-1} . The replacement of Si neighbors with more electronegative carbon atoms might lead to an increase in the frequency of Si-H stretching mode from 2000 cm^{-1} towards $2070\text{--}2100\text{ cm}^{-1}$, depending on the number of carbon atoms bonded to Si of Si-H bond. Figure 7.8 represents a gradual shift from 2078 cm^{-1} to higher frequency of 2092 cm^{-1} , as the carbon content increases (Lukovsky, 1976), without any considerable change in their FWHM values. The reason of this shift might be an eventual reduction of Si-H bond length due to the higher electronegativity of carbon atom. The absorption peak around 2130 cm^{-1} is probably corresponds to similarly shifted frequency of Si-H₂ stretching mode, which originally occurs in the films without carbon around 2090 cm^{-1} . The existence of the Si-H₂ bonds suggests the presence of voids in the a-Si:H and a-

SiC_x:H films (Rovira, 1997, Losurdo, 2005, Giangregorio, 2006). However, it is difficult to differentiate overlapped peaks of Si₃Si-H₂ and C_nSi-H stretching modes. Similar linear shifts in the frequency of Si-H stretching mode at both power densities, as seen in Figure 7.8, suggest that the expected presence of voids in the films do not have considerable effect on the bonding structure (Rovira, 1997, Gracin, 2006). Consequently, as the carbon content increases, the whole peaks in this range might shift to higher wavenumbers.

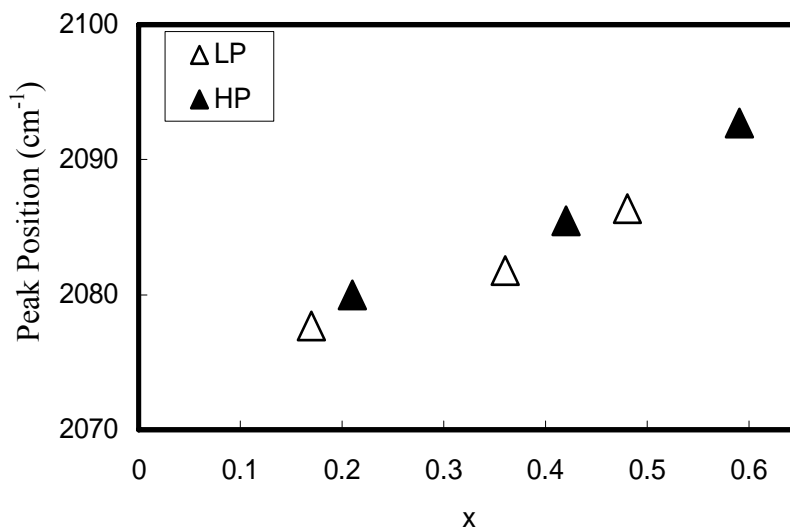


Figure 7.8. Peak position of Si-H stretching mode at 2090 cm⁻¹ is plotted, as a function of carbon content (x). Empty markers denote LP films and full markers denote HP films (Akaoglu et. al., 2006).

The absorption band between 2800-3000 cm⁻¹ (Figure 7.4), which is assigned to C-H_n (n=1,2 or 3) stretching vibration modes, is deconvoluted into four dominant peaks (P13-P16) given in Table 7.3. In order to see the relative change in concentrations of C-H_n (n=1,2,3...) bonds, symmetric and asymmetric absorption peak intensities of each mode are added up and the results are given in Figure 7.9(a) and 7.9(b). It is seen that, the concentrations of C-H₂ and C-H₃ vibrational modes increase, as x increases. Although, C-H₃ density is always greater than C-H₂ density, their ratio (CH₃/CH₂) is lowered for the HP films. In addition, C-H_n

concentrations in the films decreases at HP, in contrast to Si-H bonds in a-Si:H films.

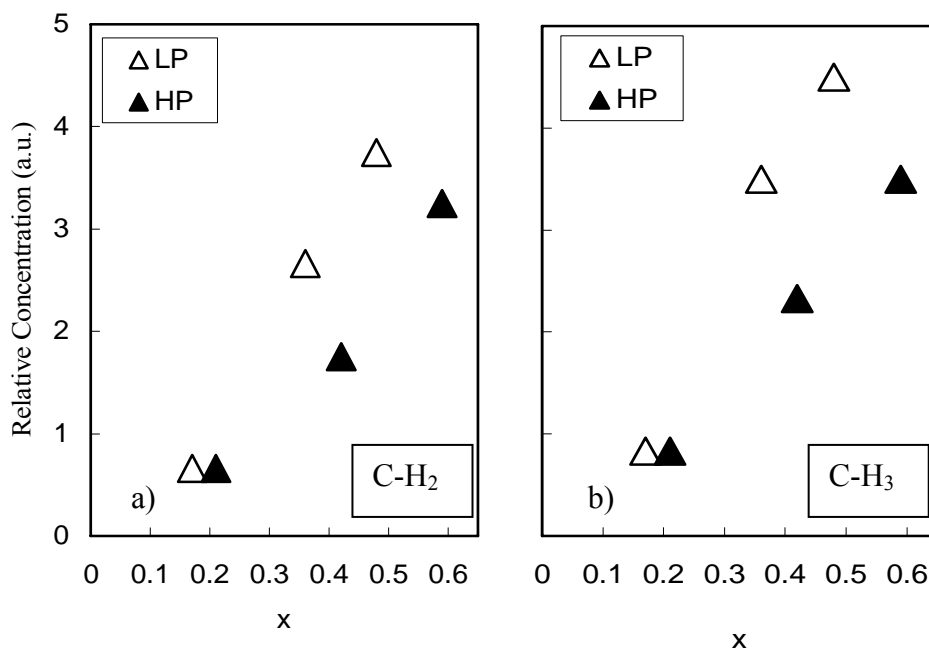


Figure 7.9. The sum of the relative concentrations of symmetric and asymmetric stretching modes of (a) C-H₂ and (b) C-H₃ bonds plotted as a function of carbon content (x). Empty markers denote LP films and full markers denote HP films (Akaoglu et. al., 2006).

The small peak beyond 2970 cm⁻¹ is attributed to sp² type C-H_n (n=1,2) bonds (Robertson, 2002) is not considered in the analysis of relative concentrations, since the intensity of this peak is very weak especially for silicon rich films. This behavior might be related to the enhanced dissociation rate of radicals which promotes formation of olefinic, even aromatic structures leading to sp² type bonds as more C atoms are incorporated in the film structure (Robertson 1992a). The peak at 3000 cm⁻¹ is attributed to sp² C-H₂ stretching mode. This peak is detected for x=0.38 and x=0.55 HP films and for only x=0.46 LP film. Its concentration increases as x rises. This is probably because of the enhanced dissociation rate of radicals, which promotes formation of olefinic and aromatic structures leading to sp² type bonds, in the film structure.

CHAPTER 8

ELECTRICAL CHARACTERISTICS OF a-SiC_x:H FILMS

8.1 CONDUCTIVITY IN AMORPHOUS SEMICONDUCTORS

In amorphous materials, at least two different electrical conduction mechanisms exist, one of which is the extended state conduction, where the mobility (μ) is not equal to zero and the second is the localized state conduction, where $\mu=0$.

The conductivity is the product of the carrier density (n) and the carrier mobility (μ) (Street, 1991, Overhof, 1989),

$$\sigma = ne\mu \quad (8.1)$$

The contributions to σ are summed over the density of states,

$$\sigma = \int N(E) \mu(E) f(E, T) dE \quad (8.2)$$

where $f(E, T)$ is the Fermi function. The integral contains contributions from electron transport above E_F and hole transport below E_F . When conductivity takes

place far from E_F by a single type of carrier, by applying the non-degenerate statistics, the equation.8.2 leads to:

$$\sigma = \frac{1}{kT} \int \sigma(E) \exp\left[-\frac{(E - E_F)}{kT}\right] dE \quad (8.3)$$

where

$$\sigma(E) = N(E) e \mu(E) kT$$

8.2 ELECTRICAL TRANSPORT IN EXTENDED STATES

If the electrons and holes in the localized states do not contribute at all to the electronic transport, the transport mechanism is entirely due to the carriers in extended states beyond the mobility edges. For this particular case, in which $\sigma(E)$ increases abruptly from zero to a σ_{\min} at the mobility edge energy (E_c), the evaluation of equation 8.3 gives:

$$\sigma = \sigma_{\min} \exp\left[-\frac{(E_C - E_F)}{kT}\right] \quad (8.4)$$

where

$$\sigma_{\min} = N(E_C) e \mu kT$$

where μ is the free carrier mobility at E_C (Overhof, 1989, Street, 1991).

8.3 ELECTRICAL TRANSPORT BY HOPPING MECHANISM

On the other hand, although there is no macroscopic conduction throughout the localized states at $T=0^\circ$ K, at higher temperatures for highly distorted medium such as in the case of amorphous structure, the localized states contribute to the conduction by the hopping mechanism.

In the case of hopping conduction, the probability P_{ij} , that an electron will jump from the state i to the state j is determined by the following three factors (Mott, 1979).

- 1) The probability of finding a phonon with excitation energy equal to E_{ij} , given by Boltzmann factor ($\exp(-(E_j-E_i)/kT)$).
- 2) The attempt to escape frequency ω_{ph} , which can not be greater than the maximum phonon frequency (In the range 10^{12} - 10^{13} s^{-1}).
- 3) The probability of electron transfer from one state (i) to another (j) ($\exp(-2\alpha_L R)$).

$$P_{ij} = \omega_{ph} \exp \left[-2\alpha_L R - \frac{E_{ij}}{kT} \right] \quad (8.5)$$

With,

$$\alpha_L = \left[\frac{\hbar^2}{2m(E - E_C)} \right]^{-1/2} \quad \text{and } E_{ij} = E_j - E_i$$

where, ' α_L ' is the localization length and ' R ' is the effective hopping distance.

Analogy with the motion of particles in a gas, diffusion coefficient (D) in crystals may be expressed by the formula of the kinetic theory of gases (Pathria, 1996, Katircioğlu, 2004):

$$D = \frac{1}{3} \bar{v} \lambda = \frac{\lambda^2}{3\tau} \quad (8.6)$$

where \bar{v} is average velocity, ' λ ' is the mean free path in the gas phase and ' τ ' is the time interval between collisions. Since the typical number of stopping atoms

in the film, where L^2 is the cross-sectional area of the film and dx is the incremental distance travelled by the particles, is the concentration of atoms ' N ' times the volume, i.e., NL^2dx , the probability that a beam particle will be stopped in that incremental region is the net area of the stopping atoms (A , cross-sectional area) divided by the total area (L^2) of the film.

$$P_{\text{stopping in } dx} = \frac{AnL^2 dx}{L^2} = ANdx \quad (8.7)$$

The drop in the flux of particles (dn) equals to the initial flux of particles (n) multiplied by the probability of being stopped within the film.

$$dn = -nANdx \quad (8.8)$$

Taking into account that $1/AN = \lambda$, the solution of this differential equation is,

$$n = n_0 \exp(-x/\lambda) \quad (8.9)$$

Because λ is equal to the mean distance travelled by a particles, it can be expressed as,

$$\lambda = \frac{1}{NA} = \int \exp\left(-\frac{x}{\lambda}\right) dx \quad (8.10)$$

Instead of mean free path (λ), mean square values (\bar{x}^2) between collisions can be calculated. Then the probability of a particle traveling the distance x without suffering any collision is given:

$$\bar{x}^2 = \frac{\int_0^{\infty} x^2 \exp\left(-\frac{x}{\lambda}\right) dx}{\int_0^{\infty} \exp\left(-\frac{x}{\lambda}\right) dx} = 2\lambda^2 \quad (8.11)$$

Substituting equation 8.11. into equation 8.6. D can be expressed in terms of R and P_{ij} .

$$D = \frac{\lambda^2}{3\tau} = \frac{\bar{x}^2}{6\tau} = \frac{R^2}{6} P_{ij} \quad (8.12)$$

Using Einstein relation, the mobility can be expressed in terms of diffusion coefficient, and hence;

$$\mu = \frac{e}{KT} \frac{R^2}{6} P_{ij} \quad (8.13)$$

Substituting equation 8.13 into equation 8.1, the conductivity can be expressed as:

$$\sigma = e^2 R^2 N(E) \frac{P_{ij}}{6KT} \quad (8.14)$$

8.3.1 VARIABLE RANGE HOPPING

At low temperatures (<200° K), the number and the energy of phonons decreases and then the more energetic phonon-assisted hopping (Nearest neighbor hopping) will progressively become less favorable. In this case, carriers tend to hop to larger distances in order to find sites, which lie energetically closer than the nearest neighbors. This mechanism is the so-called variable range hopping (VRH) (Mott, 1979, Overhof, 1989)).

For variable range hopping, in order to find the most favorable hopping distance, the transition probability (Equation 8.5.) must be maximized. Since finding an occupied state (i) and an empty state (j) with a minimum energy difference (E_{ij}) is most probable around Fermi energy, hopping should occur

around Fermi level. On the other hand, electron can leave its site only if the number of states with energy difference E_{ij} within a distance R from its site is at least one. Accordingly using $N(E_F)$, E_{ij} can be expressed in terms of R (Katırcıoğlu, 2004).

$$E_{ij} = \frac{3}{4\pi R^3 N(E_F)} \quad (8.15)$$

The maximum of the transition probability could be obtained by minimizing the exponent in the equation 8.5 by taking the derivative with respect to R .

$$R_{\min} = \left[\frac{9}{8\pi \alpha_L N(E_F) K T} \right]^{1/4} \quad (8.16)$$

Therefore, P_{ij} takes the form of;

$$P_{ij} = \omega_{ph} e^{-\frac{A}{T^{1/4}}} \quad (8.17)$$

where

$$A = 2 \left[\frac{\alpha_L^3}{k N(E_F)} \right]^{1/4}$$

Finally, substituting equation 8.17. into equation 8.14, the conductivity for variable range hopping mechanism can be written with a prefactor $\sigma_0(T)$ as,

$$\sigma = e^2 R_m^2 N(E) \frac{\omega_{ph}}{6} e^{-\left(\frac{A}{T^{1/4}}\right)} = \sigma_0(T) e^{-\left(\frac{A}{T^{1/4}}\right)} \quad (8.18)$$

8.3.2 NEAREST NEIGHBOR HOPPING

If the localization is very strong and the temperature is relatively high (typically $>200^\circ\text{K}$) a carrier will normally jump to the nearest state in space by phonon-assisted excitation to an energy level E_i within the tail states. In another word, P_{ij} falls off rapidly with distance, so that VRH is not probable. This type of conduction is called as ‘nearest neighbor hopping’ and generally occurs in the tail states of DOS distribution in the mobility gap of amorphous semiconductors (Mott, 1979, Overhof, 1989).

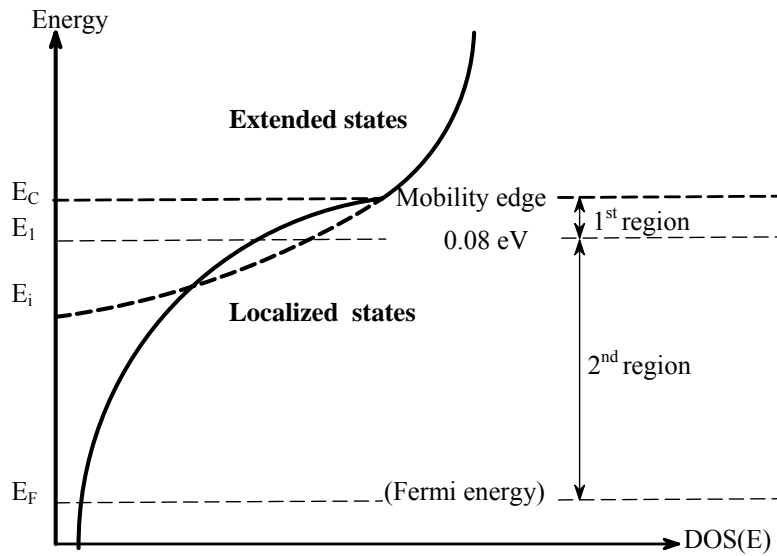


Figure 8.1. DOS distribution in the mobility gap of amorphous semiconductors.

The occupied energy level E_i , shown in Figure 8.1, can be assumed high enough above E_F , such that the majority of sites having energy E , below E_i , should be unoccupied. The carrier at E_i can eventually hop towards these empty states. Their total density can be approximated by:

$$\bar{N}(E) = \int_{E_F}^{E_i} N(E)[1 - f_F(E)]dE \quad (8.19)$$

where f_F is Fermi distribution function. For $E-E_F \gg kT$ at tail states, $f_F(E)$ can be replaced by Boltzmann distribution.

$$f_B = e^{-\frac{E-E_F}{KT}} \quad (8.20)$$

DOS of amorphous semiconductors is derived in chapter 2 for three regions of shallow (1st region), intermediate (2nd region) and deep binding energies (3rd region). As a matter of fact, DOS corresponding to the states of deep binding energy was very small with respect to the other two region. In order to derive the density of empty states, the deep binding states are neglected for simplicity and only DOS with shallow and intermediate binding energies taken into account (Godet, 2001).

If E_i is in the 2nd region ($E_1 < E_i < E_F$), the electron can only hop to the sites of 2nd region. Consequently, for this case the total number of DOS of empty states can be derived by taking into account the equation 2.29 which gives DOS corresponding to the 2nd region:

$$\bar{N}(E_i) = \int_{E_F}^{E_i} N(E_1) e^{-\frac{CEV_0}{E_0}} \left(1 - e^{-\frac{E-E_F}{KT}}\right) dE \quad (8.21)$$

The second term in equation 8.21. is very small and can be neglected that all states above E_F are empty. Resultantly by changing the variables of the integral as $\xi = E_C - E$ and $-d\xi = dE$, the solution of the first integral gives,

$$\bar{N}(\xi_i) \approx N(E_1) E_0 e^{-\frac{C\xi_i V_0}{E_0}} \quad (8.22)$$

If E_i is in the 1st region, the electron can hop to the sites of both 1st and 2nd regions. Consequently, for this case the total number of DOS of empty states can

be derived by taking into account the DOS corresponding to both 1st and 2nd regions (Equation 2.28 and 2.29) ($E_i < E_1$ eV):

$$\begin{aligned} \bar{N}(E_i) \approx & \int_{E_F}^{E_1} N(E_1) e^{-\frac{CEV_0}{E_0} - \frac{E-E_F}{KT}} dE + \\ & \int_{E_1}^{E_i} N(E_C) \frac{1}{\sqrt{E}} e^{-\frac{B\sqrt{E}V_0^{3/2}}{E_0} - \frac{E-E_F}{KT}} dE \end{aligned} \quad (8.23)$$

The terms with $\exp((E-E_F)/KT)$ are very small with respect to the other terms and can be neglected, since $E-E_F \gg KT$. By change of variables ($(E_C-E)=\xi$ and $dE=-d\xi$), the solution of the remaining parts gives,

$$\begin{aligned} \bar{N}(\xi_i) \approx & N(E_1)E_0 \left[e^{\left(\frac{CV_0E_1}{E_0}\right)} - e^{\left(\frac{CV_0E_F}{E_0}\right)} \right] + \\ & N(E_C)E_0 \left[e^{\left(\frac{BV_0^{3/2}\sqrt{\xi_i}}{E_0}\right)} - e^{\left(\frac{BV_0^{3/2}\sqrt{E_1}}{E_0}\right)} \right] \end{aligned} \quad (8.24)$$

In the nearest neighbor hopping, hopping distance R is approximated to be the distance between nearest neighbors. The volume of one site ($1/\bar{N}(\xi_i)$) can be taken equal to R^3 . Thus the hopping distance evaluated to be:

$$R(\xi) = [\bar{N}(\xi)]^{-1/3} \quad (8.25)$$

The differential current (dI) is the time derivative of the charges flowing in the differential volume (dV) defined by differential cross-sectional area (ds) and hopping distance (R) of the sample.

$$dI = \frac{dQ}{dt} \quad (8.26)$$

where

$$dQ = qn'dV$$

On the other hand, it can be expressed in terms of differential current density (dj) and cross-sectional area (ds) as:

$$dI = djds = qRds \frac{dn'}{dt} \quad (8.27)$$

The time derivative of n' , which is the density of carriers that undergoes hopping

$$\frac{dn'}{dt} = dn\delta P \quad (8.28)$$

where δP is the differential transition probability and dn is the density of filled states within $d\xi$ and ξ .

$$dn = N(\xi)f(\xi)d\xi \quad (8.29)$$

where $d\xi = qRF$ is the potential energy originated from the electric field (F) in a distance R . Hence the differential current density can be written by using the equations 8.27 and 8.28, in terms of R and ξ as;

$$dj=qRN(\xi)f(\xi)\delta P d\xi \quad (8.30)$$

The differential transition probability (δP) can be expressed differently for two different cases: First case, α is independent of energy. Then, δP can be written as;

$$\delta P = \frac{dP}{dR} \frac{dR}{d\xi} d\xi \quad (8.31)$$

The two regions of the localized states should be taken into consideration, since R is related to $N(E)$. For the 2nd region of the localized states (Figure 8.1):

$$\frac{dP}{dR} = -2\alpha P(\xi) \quad (8.32)$$

and

$$\frac{dR}{d\xi} = \frac{R}{3E_0} \quad (8.33)$$

Substituting equation 8.32 and equation 8.33 into equation 8.31 gives:

$$\delta P = \frac{qRF}{3E_0} P(\xi) \ln \left(\frac{\omega_{ph}}{P(\xi)} \right) \quad (8.34)$$

For the 1st region of the localized states (Figure 8.1):

$$\frac{dR}{d\xi} = R^4 \frac{N(E_C) B V_0^{3/2}}{6\sqrt{\xi}} e^{-\frac{B V_0^{3/2} \sqrt{\xi}}{E_0}} \quad (8.35)$$

Substituting equation 8.32 and equation 8.35 gives:

$$\delta P = qR^4 F \frac{N(E_C) B V_0^{3/2}}{6\sqrt{\xi}} e^{-\frac{B V_0^{3/2} \sqrt{\xi}}{E_0}} P(\xi) \ln\left(\frac{\omega_{ph}}{P(\xi)}\right) \quad (8.36)$$

Second case, α is depended on energy:

$$\delta P = \frac{dP}{dR} \frac{dR}{d\xi} d\xi + \frac{dP}{d\alpha} \frac{d\alpha}{d\xi} d\xi \quad (8.37)$$

For this case, for the 2nd region of the localized states (Figure 8.1):

$$\frac{dP}{d\alpha} = -2RP(\xi) \quad (8.38)$$

and

$$\frac{d\alpha}{d\xi} = \frac{\alpha}{2\xi} \quad (8.39)$$

Substituting equation 8.32, 8.33, 8.38 and 8.39 into equation 8.37 gives:

$$\delta P = qRF \left(\frac{1}{3E_0} + \frac{1}{2\xi} \right) P(\xi) \ln\left(\frac{\omega_{ph}}{P(\xi)}\right) \quad (8.40)$$

For the 1st region of the localized states (Figure 8.1), substituting equation 8.32, 8.35, 8.38 and 8.39 gives:

$$\delta P = qRF \left[\left[\frac{R^3 N(E_C) B V_0^{3/2}}{6\sqrt{\xi}} e^{-\frac{B V_0^{3/2} \sqrt{\xi}}{E_0}} \right] + \frac{1}{2\xi} \right] P(\xi) \ln \left(\frac{\omega_{ph}}{P(\xi)} \right) \quad (8.41)$$

Finally, the differential conductivity of nearest neighbor hopping mechanism for the 1st and 2nd regions of the localized states is obtained by substituting the corresponding quantities into equation 8.30. For the 1st region:

$$d\sigma = q^2 R(\xi)^2 N_{1st}(\xi) f(\xi) \left(\frac{N(E_C) B V_0^{3/2} R^3}{\frac{B V_0^{3/2} \sqrt{\xi}}{e^{-\frac{B V_0^{3/2} \sqrt{\xi}}{E_0}}}} + \frac{R}{2\xi} \right) P \ln \left(\frac{\omega_{ph}}{P} \right) d\xi \quad (8.42)$$

For the 2nd region:

$$d\sigma = -q^2 R(\xi)^2 N_{2nd}(\xi) f(\xi) \left(\frac{C V_0}{3E_0} + \frac{1}{2\xi} \right) P \ln \left(\frac{\omega_{ph}}{P} \right) d\xi \quad (8.43)$$

In Figure 8.2, differential hopping conductivity is plotted for various selections of T , E_0 , 'a' and $N(E_C)$ by considering the 1st and the 2nd regions, together and by considering only the 2nd region. In both cases, as T , E_0 , 'a' and $N(E_C)$ are increased the differential hopping conductivity also increased (Figure 8.2 a1,a2,b1,b2,c1,c2). This was expected, due to the increase in the probability of hopping between states. Furthermore, in Figure 8.2.c2, it is observed that the dominant conduction moves toward E_F especially for large potential well widths, as seen in Figure 8.2.c1. Besides, large DOS has the same effect especially for the approximation when 1st region is not taken into consideration. When both regions are considered, lower conductivities are obtained, this is probably because of the reason that $E^{-1/2}$ dependence, in the first region, sharply reduces DOS, since $N(E_C)$ at E_C is taken to be constant. The sharp increase of conductivity near E_C is caused by the energy dependence of $\alpha(E)$, which results in $1/E$ term in equations 8.42 and 8.43.

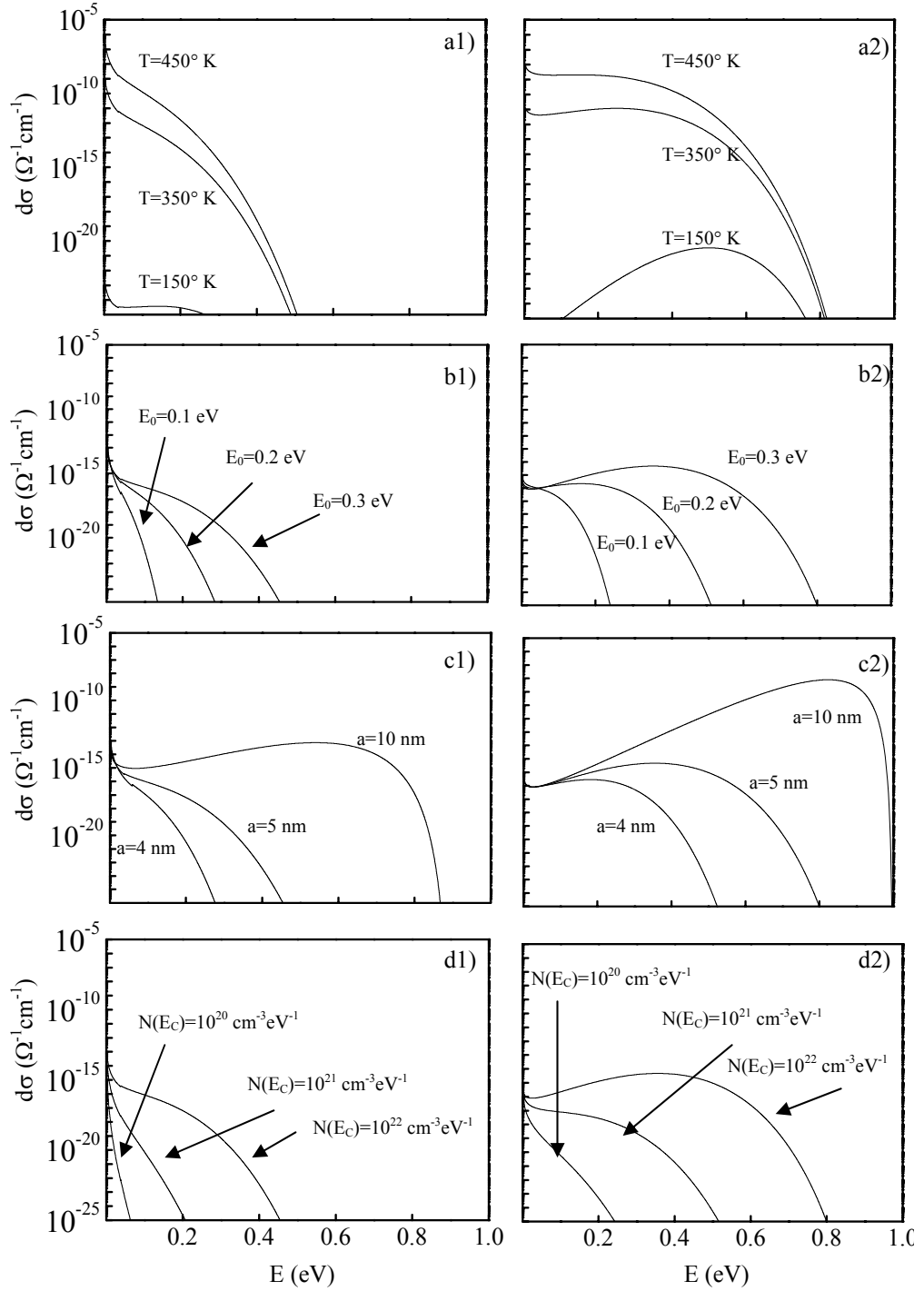


Figure 8.2. Differential hopping conductivity plotted for various values of a) temperatures; b) E_0 ; c) a ; and d) $N(E_c)$, by considering the 1st and the 2nd regions together (a1, b1, c1, d1) and by considering only the 2nd region (a2, b2, c2, d2). For each graph fixed parameters are taken as $\omega_{ph}=10^{12} \text{ s}^{-1}$, $E_F=1 \text{ eV}$, $a=5 \text{ nm}$, $T=300^\circ\text{K}$, $E_0=0.3 \text{ eV}$ and $N(E_c)=10^{22} \text{ cm}^{-3} \text{ eV}^{-1}$.

Finally, the conductivity of hopping mechanism is obtained by taking the integral of differential conductivity, where the limits of the integral starts from $-\infty$, and extracts to $+\infty$ in energy. But, the differential hopping conductivity is approximated to be zero for energies lower than E_F and higher than E_C . Then, σ can be written for the DOS including the 1st and 2nd regions as;

$$\sigma = \left[\int_{E_F}^{E_1} d\sigma_2(\xi) + \int_{E_1}^0 d\sigma_1(\xi) \right] \quad (8.44)$$

and for only 2nd region;

$$\sigma = \left[\int_{E_F}^0 d\sigma_2(\xi) \right] \quad (8.45)$$

In Figure 8.3 conductivity is plotted for various values of E_0 , 'a' and $N(E_C)$ by considering the 1st and the 2nd regions, together. The Arrhenius plots, σ versus $1/T$, are depicted in Figure 8.3 by considering 1st and 2nd regions (Figure 8.4.a1, b1, c1) and by considering only 2nd region, (Figure 8.3. a2, b2, c2) respectively, for various values of E_0 , a and N_0 . In these Figures, increase in 'a' resulted in an increase in conductivity mostly for lower temperatures. It is also clear from Figures that Arrhenius plots show thermally activated conduction mechanisms with much lower activation energies, than the actual 1 eV. For instance, for even the most ordered case with $E_0=0.1$ eV, $\omega_{ph}=10^{12}$ s⁻¹, $E_F=1$ eV, a=5 nm, $E_0=0.3$ eV and $N(E_C)=10^{22}$ cm⁻³eV⁻¹ the activation energy is equal to 0.9 eV for considering 1st and 2nd regions and equal to 0.89 eV for considering only the 2nd region. This proves that the dominant conduction path occurs in the tail states, which result in lower activation energies, especially for high well widths and high DOS in the tail states. This kind of conduction mechanism can be expected in amorphous semiconductors, mostly with large E_0 .

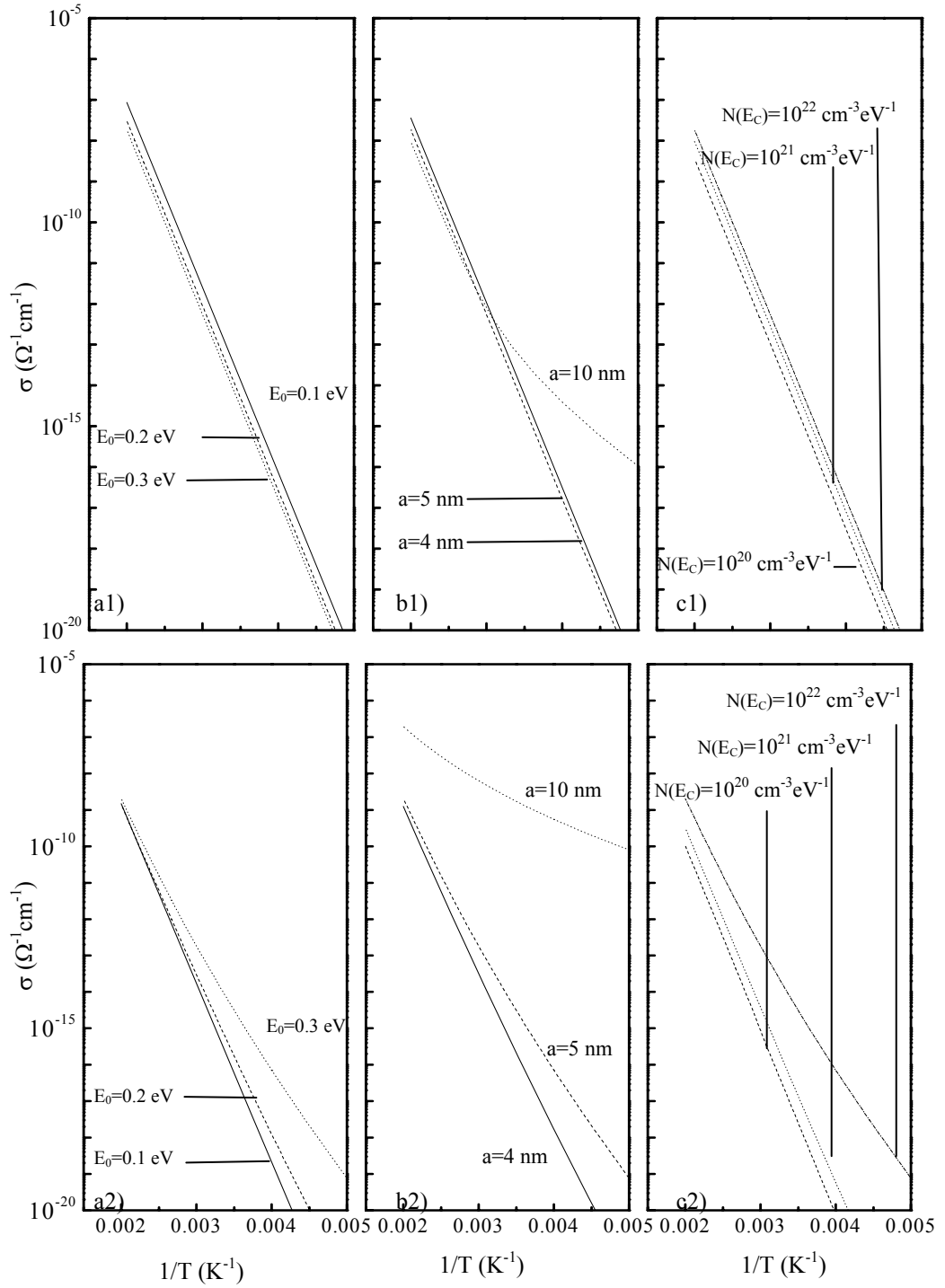


Figure 8.3. Hopping conductivity plotted for various values of a) temperatures; b) E_0 ; c) a; and d) $N(E_C)$ by assuming equation 8.44 and 8.45 (a1, b1, c1), together and assuming only equation 8.44 (a2, b2, c2). For each graph fixed parameters are taken as $\omega_{\text{ph}}=10^{12} \text{ s}^{-1}$, $E_F=1 \text{ eV}$, $a=5 \text{ nm}$, $E_0=0.3 \text{ eV}$ and $N(E_C)=10^{22} \text{ cm}^{-3} \text{ eV}^{-1}$.

8.4 ELECTRICAL ANALYSIS OF a-SiC_x:H FILMS

In the light of the theoretical analysis, the electrical characterization of the a-SiC_x:H films, deposited by PECVD with various gas concentrations at two different r.f. power densities (Lower (LP) and higher (HP) powers of 30 mW/cm² and 90 mW/cm²) was performed.

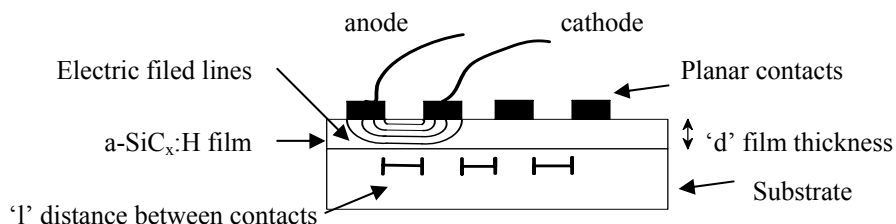


Figure 8.4. Schematic diagram of sample prepared for conductivity measurements.

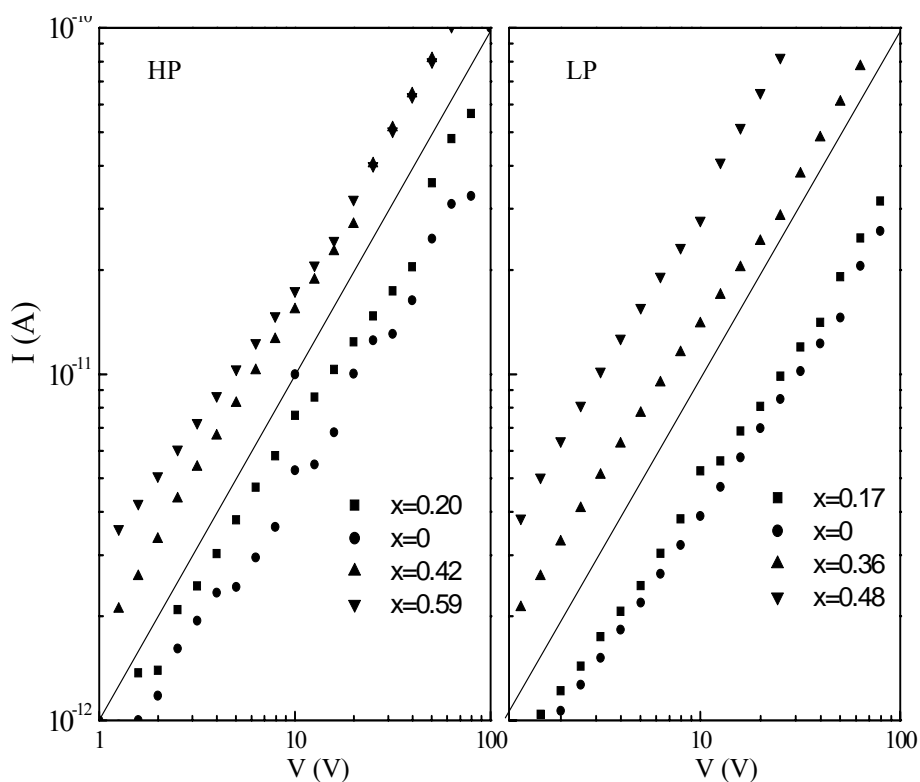


Figure 8.5. Room temperature dc conductivity measurements of HP and LP a-SiC_x:H films, are plotted as a function of carbon content (x). Ohmic trend is shown by solid line.

The room temperature dc conductivities were obtained by using conventional two probe method through planar contacts, given in Figure 8.4. First, conductivity measurements were taken by changing the direction of the current in order to eliminate probable depletion layer or voltage barrier at the contacts. It is revealed that conductivity behavior is independent of the direction of the current through the sample. Second, multiple conductivity measurements were performed by fixing the anode on one planar contact and changing the cathode for each measurement to next planar contact, in order to change the dimensions of the sample and resultantly the convenience of the conductivity measurements could be investigated by comparing each measurement. Resistance of each sample is calculated by using the Ohmic part of the conductivity measurements as shown in Figure 8.5.

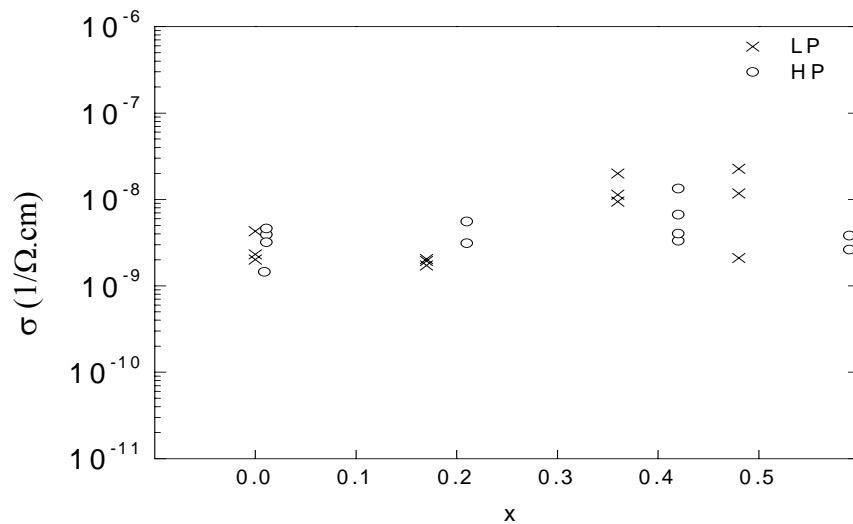


Figure 8.6. Room temperature dc conductivities of HP and LP a-SiC_x:H films are plotted as a function of carbon content (x)

The dc conductivities are determined by using resistance (R) and dimensions of the film between contacts, as given in equation 8.46.

$$\sigma = \frac{l}{R.A} \quad (8.46)$$

where 'l' is the distance between the contacts and A is the cross-sectional area of the film, which is the product of the film distance (d) and the contact length. The room temperature conductivities are given in Figure 8.6. They increase for LP a-SiC_x:H films, and they slightly increase for HP a-SiC_x:H films, with increasing carbon content (x).

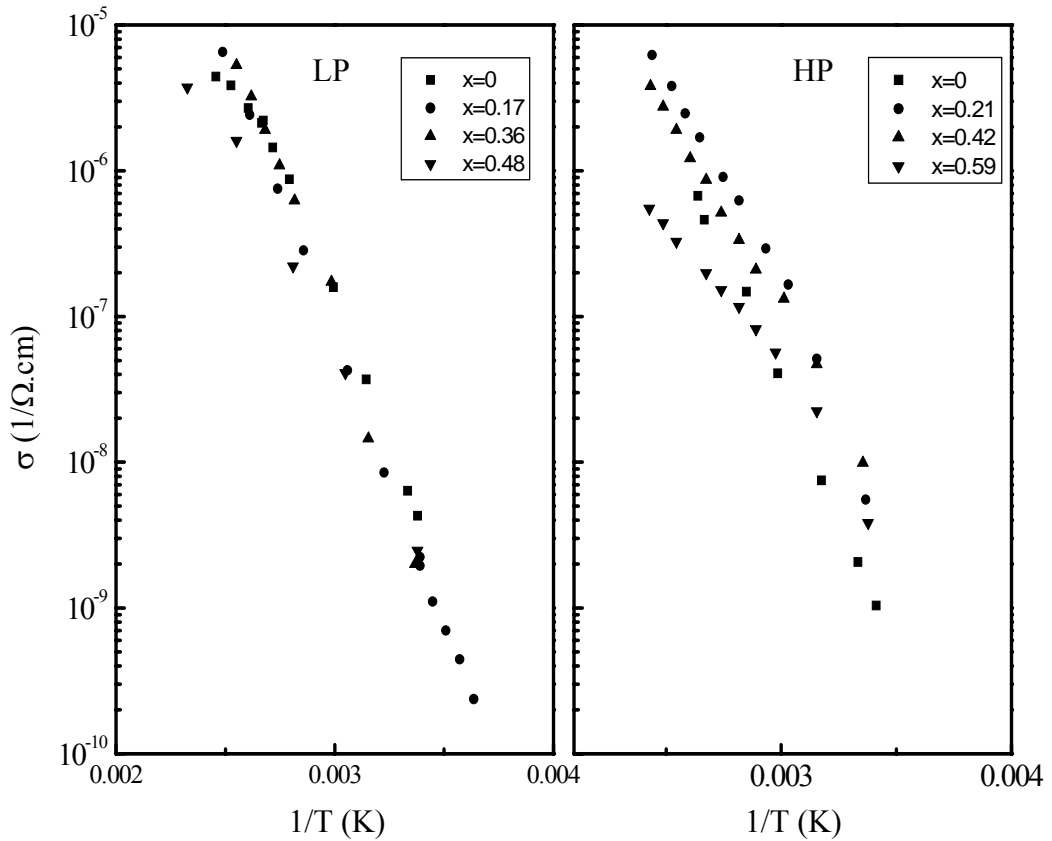


Figure 8.7. Conductivity of HP and LP a-SiC_x:H films are plotted as a function of inverse temperature.

The dc conductivities of the films were also studied in the temperature range of 250 to 450 K°, as given in Figure 8.7. In Figure 8.7, each data mark represents a conductivity, which is obtained by using the Ohmic part of conductivity measurement at constant temperature.

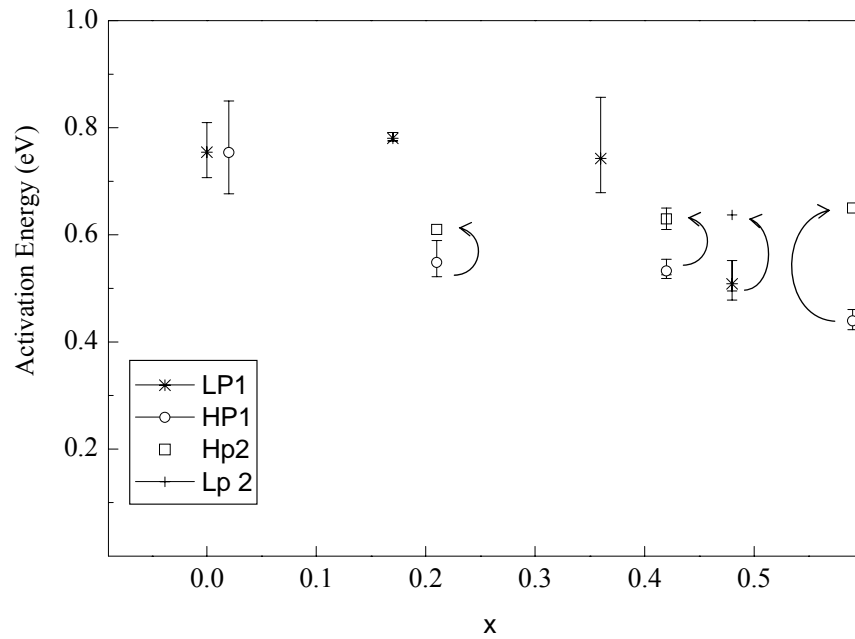


Figure 8.8. Activation energies of a-SiC_x:H films obtained for only standard transport model case (LP1 and HP1) and for both standard model and hopping mechanism case (LP2 and HP2) are plotted as a function of carbon content (x). Where HP denotes higher (90 mW/cm²), and LP denotes lower (30 mW/cm²) power densities.

The activation energies of the a-SiC_x:H films were evaluated firstly by using the standard transport model, where the localized states do not contribute to the electronic transport and the transport mechanism is entirely due to the carrier in extended states beyond the mobility edge (Figure 8.8.(LP1 and HP 1)), equation 8.4). The increase in 'x', for both HP and LP a-SiC_x:H films, was apparently resulted in a decrease in the activation energies. As it is known that mobility gap of the films increase with x and hence a decreasing activation energy may not be expected for intrinsic films. But, hopping conduction at localized states might be the reason for apparent E_a. For this reason, the contribution of hopping conduction at tail states is numerically analyzed by computer based fitting to experimental conductivity versus 1/T graphs. In the fitting procedure, σ_H and σ_E, are used for hopping and extended state conductivities, given by equation 8.4 and 8.45, respectively. The second region is

considered due to $1/\sqrt{E}$ term, resulting in underestimated hopping conductivity. The percentage of hopping and extended state conductivities are also determined by using a simple unconstrained multivariable function fitting expression.

$$\sum (\sigma_M - (\eta\sigma_H + (1-\eta)\sigma_E))^2 = 0 \quad (8.47)$$

where σ_M denotes measured conductivity, and η is a constant, used to determine the percentage of hopping conductivity. The DOS at mobility edge was taken as $10^{22} \text{ cm}^{-3} \text{ eV}^{-1}$ and the potential well width 'a' (localization radius) was considered to be independent of the energy of the localized states and was taken as 5×10^{-8} cm. As a result of fitting, an increase in the activation energies is observed for HP films of carbon content $x=0.21, 0.42$ and 0.59 ; whereas for LP films an increase was observed for only $x=0.48$.

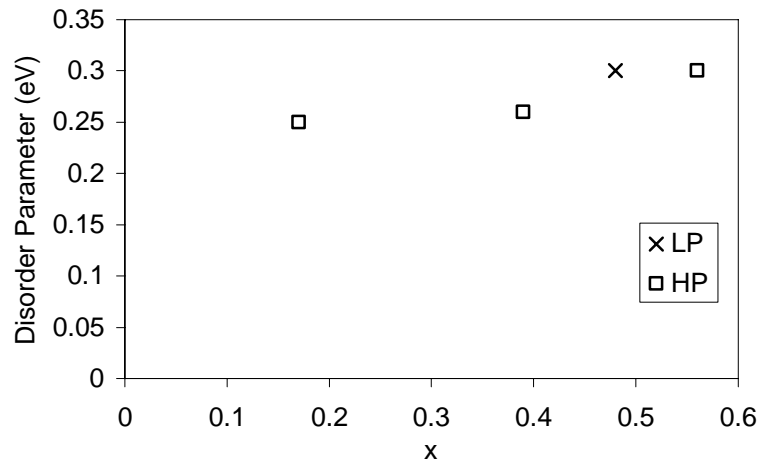


Figure 8.9. Disorder parameters obtained for the hopping conduction mechanism for a-SiC_x:H films, deposited at higher (90 mW/cm²)(HP), and lower (30 mW/cm²)(LP) power densities are plotted as a function of carbon content (x)

It is known that hopping conduction depends on DOS distribution in the mobility gap, which is related to disorder parameter (E_0) for amorphous thin

films. The disorder parameters are obtained and presented in Figure 8.9. The parameter increases with carbon content as expected.

The percentage of the hopping current, given in Figure 8.10, is determined by multiplying η with 100 in the fitting equation 8.47. The contribution of hopping conduction is mostly observed for HP a-SiC_x:H films, whereas for LP a-SiC_x:H films only for the one with $x=0.48$, a slight contribution is observed. This conforms that, incorporation of carbon into the films sharply promotes disordered structure especially for high power case, due to the higher dissociation rate of C₂H₄ molecules by plasma species.

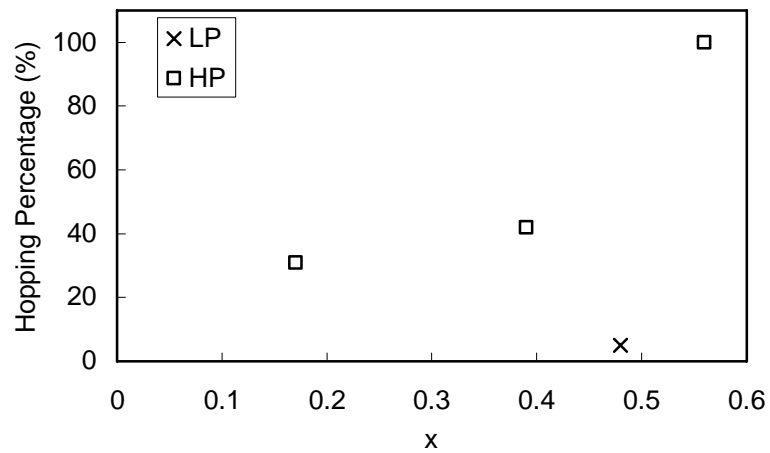


Figure 8.10. Hopping conduction percentage among the overall conduction of a-SiC_x:H films, deposited at higher (90 mW/cm²)(HP), and lower (30 mW/cm²)(LP) power densities are plotted as a function of carbon content (x).

CHAPTER 9

CONCLUSIONS

The structure of $a\text{-SiC}_x\text{H}$ is theoretically revised. The bonding organization changes drastically from pure $a\text{-Si:H}$, $x=0$, to pure $a\text{-C:H}$, ($x=1$) and resultantly, the film consists of many different structures, such as tetrahedral (sp^3), aromatic (sp^2), and olefinic (sp^1) structures. Accordingly, effects of this structural diversity on the energy band gap is discussed on the basis of cluster sizes. In this respect, the characteristics of DOS distribution are investigated by reviewing the corresponding characteristics of $a\text{-Si:H}$ and $a\text{-C:H}$. In the Si rich region sp^3 Si-Si bonds exists. If C is introduced into the film with small concentration ratio, stronger sp^3 type Si-C bonds are formed, which are eventually increased the energy gap. In the light of defect pool model, the DOS distribution in the mobility gap is also investigated. Assuming the defect states to be spherical potential wells, first the solutions for quantum mechanically true binding states are obtained in terms of potential well depth and energy. By using the solutions obtained for shallow, intermediate and deep binding energies, the corresponding DOS distributions are determined.

The aspects of PECVD system and dissociation of plasma gases are revised. The films are deposited by PECVD system with various gas concentrations at two different, lower (30 mW/cm^2) and higher (90 mW/cm^2), r.f. power densities, as source gases consist of C_2H_4 , SiH_4 and H_2 . The samples are

prepared for electrical measurements by coating appropriate metal contacts by e-beam and magnetron sputtering and resistive evaporation techniques.

The elemental composition of the a-SiC_x:H films and relative composition of existing bond types are analyzed by XPS measurements. It is observed that, the elemental composition of C increases, as gas concentration (M) increases. Additionally, the composition of C-C/C-H bond increases and Si-Si/S-H bond decreases with increasing M. This effect is increased especially for HP films as expected due to higher dissociation rate of ethylene molecules. Finally, Si-C bonds are found to be increased with increasing carbon content, especially reaching relatively higher values for HP films.

The thicknesses, deposition rates, refractive indices and optical band gaps of the films are determined by UV-Visible transmittance measurements. The optical properties are analyzed by both envelop method and optical characterization software. The uniformity of the deposited films are analyzed along the radial direction of the PECVD reactor. The thickness, and optical gaps of the films increases, whereas the refractive indices decrease towards the edge of the reactor, respectively. This is attributed to the eventual non-uniform distribution of carbon bearing precursors, the increased density of unsaturated radicals towards the edge and the cooperative participation of ions and radicals in the growth to form chemical bond by overcoming the activation barrier via the energy supplied by ions impinging on the growth surface. The higher deposition rates at high power might be caused by increased dissociation rate and stronger ion bombardment resulting in high density of dangling bonds regardless of type of bonds on the growing surface. On the other hand, the deposition rates of the films are observed to be decreasing as M increases for both power densities. On the other hand, the decrease at HP films is much smaller than the one at LP films. The carbon contents of the films are determined by comparing the optical gaps and refractive indices separately with the values published in the literature. The estimated x by using refractive indices are the same with the ones obtained by using the optical gaps. Additionally, almost similar carbon contents are obtained with UV-Visible spectroscopy and XPS. The variation of x as a function of M is

approximately linear and the slopes of HP and LP films seem considerably increased for LP films. It is observed that the refractive indices decrease, as x increases. Furthermore, for the same x , refractive indices of the HP films are smaller than the ones of LP films. Oppositely, the optical gaps increase as x increases and the amount of increase is higher for HP films, respectively. The reason for the decrease in the refractive indices and increase in the optical gap might be the increasing number of strong Si-C bonds.

The vibrational characteristics of the a-SiC_x:H films are reviewed and analyzed by FTIR measurements. The absorption peaks, consisting of three main absorption bands, are deconvoluted according to the published peak values given in the literature. The absorption peaks beyond 700 cm⁻¹ start to appear for both power densities as carbon is incorporated in the films. Especially, the peak around 770 cm⁻¹, which is associated to Si-C, becomes dominant, as x increases. Whereas, the peaks at around 640 cm⁻¹ and 670 cm⁻¹ show similar character to the peak around 2000 cm⁻¹ associated to Si-H. Therefore, the peak at 670 cm⁻¹ is attributed to the Si-H bond. The small peak, around 2970 cm⁻¹ is attributed to sp² type C-H and C-H₂ bonds, which is observed mostly in carbon rich films. The presence of this peak implements the enhanced dissociation rate of radicals, which promotes formation of olefinic, even aromatic structures as more carbon atoms are incorporated in the film.

Electrical characteristics of the films are analyzed by dc conductivity measurements performed at room temperature and in the temperature range of 250 K° to 450 K°. The obtained dc conductivities increase for both LP and HP films, where the increase is slightly higher for HP films. By using the Arrhenius plots of the conductivities, considering only the extended state conduction, the activation energies are calculated. The obtained activation energies, especially the ones of C rich films, have lower values with respect to the expected ones, which should be nearly the half of the optical gap. Additionally, a decrease is observed in activation energies as carbon content increases, where the trend should be increasing, since the optical gap increases with carbon content. Hence,

considering the probable high DOS distribution in the tail states, occurring mostly for C rich films, variable range hopping conduction mechanism is also taken into account, besides the extended state conduction. Resultantly, the conduction mechanisms, such as extended state conduction and hopping conduction, in amorphous materials are revised. By using the previously obtained DOS distributions in various regions of the mobility gap, the differential conductivities in the tail states are investigated. The differential hopping conductivities in the tail states are calculated as a function of energy, in the range from zero to E_F , for different temperatures, disorder parameters, potential well widths and DOS values at the mobility edge. In the next step, by integrating the differential conductivities, the conductivities are obtained and examined for different disorder parameters, potential well widths and DOS values at mobility edge. After that, the resultant conductivities are analyzed by a numerical fitting considering both extended state conduction and hopping conduction. Finally, as a result of fitting, an increase in the activation energies is observed for HP films, whereas for LP films only an increase is observed for the film with $x=0.48$.

REFERENCES

- Agrawal B.K., J. Non-Cryst. Solids, vol. 114, p. 519, 1989.
- Akaoglu B., Gulses A., Atilgan I., Katircioglu B., Vacuum, vol. 81, p. 120, 2006.
- Akaoglu B., Atilgan I., Katircioğlu B., Thin solid films, 437, p.257-265, 2003.
- Akaoglu B., Optical Properties of Silicon Based Amorphous Thin Films, Ph. D. Thesis, METU, Ankara, 2004.
- Akaoglu B., Sel K., Atilgan I., Katircioglu B., ‘Carbon Content Influence On The Optical Constants Of Hydrogenated Amorphous Silicon Carbon Alloys’, Optical Materials, (In press, 2006)
- Ambrosone G., Coscia U., Ferrero S., Giorgis F., Mandracci P., Pirri C. F., Phil. Mag. B, vol. 82, p. 35, 2002.
- Ambrosone G., Ballarini V., Coscia U., Ferrero S., Giorgis F., Maddalena P., Patelli A., Rava P., Rigato V., Thin Solid Films, vol. 427, p. 279, 2003.
- Ambrosone, Capezzuto P., Catalanotti S., Coscia U., Mormone S., Philosophical Magazine B, vol. 80, p.497, 2000.
- Aspnes D.E, Craighead H.G., Appl. Opt., vol. 25, p. 1299, 1986.
- Atilgan I, The Production and Characterization of Si Thin Films, (Ph.D Thesis), METU, Ankara(1993)
- Avilla A, Montero I., Galan L., Ripalda J.M., Levy R., Journal of Applied Physics, Volume 89, Number 1, 2001.
- Bacalis N., Economou E.N., Cohen M.H., Phys. Rev. B37, pp. 2714-2717, 1988.

- Bassani F., Parravicini G.P., Ballinger R.A., *Electronic States and Optical Transitions in Solids*, Pergamon Press, Oxford, 1975.
- Birgin E.G., Chamboleyron I., Martinez J.M., *J. Comput. Phys.*, vol. 151, p. 862, 1999.
- Bullot J., Schmidt M.P., *Phys. Stat. Sol. (b)*, vol. 143, p.345, 1987.
- Catherine Y., Zamouche A., Bullot J., Gauthier M., *Thin Solid Films*, vol. 109, p. 145, 1983.
- Catherine, Y., Turban G., Grolleau B., *Thin Solid Films*, 76, 23, 1981.
- Catherine, Y., Turban, G., *Thin Solid Films*, 60, 193, 1979.
- Chamboleyron I., Martinez J. M., Moretti A.C., Mulato M., *Appl. Opt.*, vol. 36, p.8238, 1997.
- Chamboleyron I., Martinez J.M., Moretti A.C., Mulato M., *Thin Solid Films*, vol. 317, p. 133, 1998.
- Chew K., Rusli, Yoon S.F., Ligatchev V., Teo E. J., Osipowicz T., Watt F., *J. Appl. Phys.*, vol. 92, p. 2937, 2002.
- Choi W. K., Ong T. L., Tan L. S., Loh F. C., Tan K. L., *J. Appl. Phys.*, Vol. 83, p. 4968, 1998.
- Chui J., Yoon S.F., Teo E.J., Yu M.B., Chew K., Ahn J., Zhang Q., Osipowicz T., Watt F., *J. Appl. Phys.*, vol. 89, p. 6153, 2001.
- Cody G.D., Brooks B.G., Abeles B., *Solar Energy Mater.*, vol. 8, p. 231, 1982.
- Cody G.D., *Semiconductor and Semimetals*, Vol. 21, part B, p.11, 1984.
- Cotton A. F., *Chemical Applications of Group Theory*, Third Edition, John Wiley & Sons, New York, 1990.
- D. Briggs and Seah M.P., *Practical surface analysis vol. 1 Auger and x-ray photoelectron spectroscopy*, John Wiley and Sons, Chichester, UK. 1990
- Dagel, D.J., Mallouris C. M., Doyle J. R., *J. Applied Physics*, 79, 8735, 1996.
- Demichelis F., Pirri C.F., Tresso E., Stapinski T., *J. Appl. Phys.*, vol. 71, p.5641, 1992.

- Demichelis F., Giorgis F., Pirri C.F., Tresso E., *Phil. Mag. A*, vol. 72, p. 913, 1995.
- Dieguez Campo J.M., Lenski M., Comes F.J., *Thin Solid Films*, 3243, 115, 1998.
- Economou E.N., Soukoulis C.M., Cohen M.H., John S., *Disordered Semiconductors*, Ed. by Kastner M.A., Thomas G.A., Ovshinsky S.R., 1987.
- Fadini A., *Vibrational Spectroscopy*, John Wiley & Sons, New York, 1989.
- Ferreira I., Costa M. E. V., Pereira L., Fortunato E., Martins R., Ramos A. R., Silva M. F., *Appl. Surf. Sci.*, vol. 184, p. 8, 2000.
- Foti G., *Appl. Surf. Sci.*, vol. 184, p. 20, 2001.
- Frova A., Selloni A., in: *Tetrahedrally-Bonded Amorphous Semiconductors*, ed. by Adler D., Fritzsche H., Plenum Press, New York, p. 271, 1985.
- Fujii, T., and Kim, H. S., *Chemical Physics Letters*, 268, 229, 1997.
- Gasiorowicz S., *Quantum Physics*, 2nd. Ed., John Wiley & Sons, Inc. Press, New York, 1996.
- Giangregorio M. M., Losurdo M., Sacchetti A., Capezzuto P., Bruno G., *Thin Solid Films*, vol. 511-512, p. 598, 2006.
- Giorgis, F., Pirri C. F., Tresso E., Rava P., *Philosophical Magazine*, B 75, 4, 471, 1997.
- Godet C., *Philosophical Mag. B*, Vol. 81, No: 2, p. 205-222, 2001
- Gracin D., Juraik K., Dupcek P., Gajovic A., Bernstoff S., *App. Surf. Sci.*, vol. 252, p. 5598, 2006.
- Grein C.H., John S., *Phys. Rev. B*, vol. 36, p. 7457, 1987.
- Halac E. B., *Surface and Coatings technology*, 122, p51, 1999.
- Handbook of X-Ray Photoelectron Spectroscopy*, Perkin Elmer Corporation, Physical Electronics Division
- Heavens O. S., *Optical Properties of Thin Solid Films*, Dower Publications, New York, 1991.

- Heavens O.S., *Physics of Thin Films*, ed. by Hass G., Thun R.E, Academic, New York, 1964.
- Herremans H., Grevendonk, Van Swaaij R.A. C. M. M., Van Sark W.G.J.H.M., Berntsen A.J.M., Arnold Bik W.M., Bezemer J., *Philos. Mag. B*, vol.66, p. 787, 1992.
- Hopf C., Schwarz-Selinger T., Jacop W., von Keudell A., *J. Appl. Phys.*, vol. 87, p. 2719, 2000.
- Inagaki, N., “Plasma Surface Modification and Plasma Polymerization”, Technomic Publishing Company Inc., Basel, 1996.
- Jackson W.B., Tsai C.C., Kelso S.M., *J. Non-Crystalline Solids*, Vol. 77&78, p. 281, 1985.
- Jackson W.B., Kelso S.M., Tsai C.C., Allen J.W., Oh S.J., *Phys. Rev. B*, vol. 31, p. 5187, 1985.
- Jacobsson R., in *Progress in Optics*, ed. by Wolf E., (Noth-Holland, Amsterdam, Vol. 5, p.247, 1965.
- Jasinski, J.M., Becerra R., Walsh R., *Chem. Rev.*, 95, 1203, 1995.
- John S., Soukoulis C., Cohen M.H., Economou E.N., *Phys. Rev. Lett.* 57, 1986.
- Jong W.L., Koeng S.L., *Appl.Phys.Lett.*, 69 pp.547, 1996.
- Kampas F.J., *J. Appl. Phys.*, vol. 53, p.6408, 1982..
- Kanicki J., *Amorphous and Microcrystalline Semiconductor Devices: Optoelectronic Devices*, Arctect House, Boston, London, 1991.
- Katayama Y., Usami K., Shimada T., *Philos. Mag. B*, vol. 43, p.283, 1981.
- Katircioğlu, B., METU Physics Department Lecture Notes, (2004).
- Keudell A. V., Meier M., Hopf C., *Diamond Related Materials*, vol. 11, p.969, 2002.
- Keudell A. V., Schwarz-Selinger T., Meier M., Jacob W., *J. Appl. Phys.*, vol. 76 p.676, 2000.

- Kittel C., Introduction to Solid State Physics, John Wiley & Sons, New York, 1996.
- Knights J.C., Lujan R.A., Rosenblum M.P., Street R.A., Biegelsen D.K., Reimer J.A., Appl. Phys. Lett., vol. 38, p. 331, 1981.
- Kobayashi, H., Shen M., Bell A. T., Macromol J., Macromol J., Science Chemistry, A8, 373, 1974.
- Kobayashi, H., Bell A. T., Shen M., Macromolecules, 7, 3, 277, 1974.
- Koos, M., Diamond and related Materials, 8, 1919, 1999.
- Kruangam, D. in “Amorphous and Micro-crystalline Semiconductor Devices II: Optoelectronic Devices”, Ed. By Kanicki, J., Artech House, London, 1991.
- Kuhman D, S. Grammatica, F. Jansen, Thin Solid Films, vol. 177, p. 253, 1989.
- Langford A.A., Fleet M.L., Nelson B.P., Landford W.A., Maley N., Phys. Rev. B, vol. 45, 13367, 1992.
- Leo G., Galluzzi G., Guattari G., Viicenzoni R., Demichelis F., Ciovini G., Pirri C.F., Tresso E., J. Non.Cryt. Solids, vol. 164-166, p. 1035, 1993.
- Li Y.M., Fieselmann B.E., Appl. Phys Lett., vol. 59, p. 1720, 1991.
- Lieberman A. M., Lichtenberg J. A., A Wiley-Interscience Publication, New York, 1994.
- Lin S., Chang S. T., J. Phys. Chem. Solids, vol. 59, p. 1399, 1998.
- Losurdo M., Giangregorio M., Capezzuto P., Bruno G., Giorgis F., J. Appl. Phys., vol. 97, 103504, 2005.
- Lucovsky G., Solid State Communications, vol. 29, p. 571, 1979.
- McKenzie D. R., J. Phys. D:Appl. Phys., vol. 18, p.1935, 1985.
- Minkov D.A., J. Phys. D: Appl. Phys. Vol. 22, p. 199, 1989.
- Mott N. F., Davis E. A., Electronic Processes in Non-crystalline materials, 2nd Ed., Oxford, 1979
- Mott N. F., Philosophical Mag., 19, pp.385, 1969.

- Mui K., Basa D.K., Smith F.W., Corderman R., Phys. Rev. B, vol. 35, p. 8089, 1987.
- O'Leary S.K. , Lim P.K., Appl. Phys. A66 pp. 53-58, 1997.
- O'Leary S.K., Appl. Phys. Lett., vol. 82, p. 2784, 2003.
- O'Leary S.K., Zukotynski S., Perz J.M., Phys. Rev. B 51, pp. 4143-4149, 1995.
- Oheda H., Jap. J. Appl. Phys., vol. 18, p. 1973, 1979.
- Overhof H., Thomas P., Electronic Transport in Hydrogenated Amorphous Semiconductors, Springer-Verlag, London, 1989.
- Robertson J, materials Science Engineering R, Vol. 37, p 129, 2002.
- Robertson, J, O'Reilly, E., P., Phys. Rev. B, 36, 2946, 1987.
- Robertson, J, Philosophical Magazine B, Vol.66, No.5, 615-638, 1992a.
- Robertson, J, Surface and Coating Technology, 50,185-203, 1992b.
- Robertson, J,Advances in physics, 35, 317-374, 1986.
- Robertson, J. Non-Cryst. Solids, 137&138, 825-830, 1991.
- Rovira P.I., Alvarez F., Phys. Rev. B, vol. 55, p. 4426, 1997.
- Schiff L. I., Quantum Mechanics, 3rd Ed., Mc. Graw Hill, New York, 1968.
- Sha Z. D., Wu X. M., Zhuge L. J., Vacuum, 7, p. 250, 2005.
- Siebert W., Carius R., Fuhs W., Jahn K., Phys. Stat. Sol. (b), vol. 140, p. 311, 1987.
- Skumanich A., Frova A., Amer N.M., Solid State Communications, vol. 54, p. 597, 1985.
- Sotiropoulos J., Weiser G., J. Non-Cryst. Solids, vol. 92, p. 95, 1987.
- Stallhofer P., Huber D., Solid States technology, pp 233-237, 1983.
- Street, R.A., Hydrogenated Amorphous Silicon, Cambridge University Press, Cambridge, 1991.

- Summonte C., Rizzoli R., Bianconi M., Desalvo A., Lencinella D., Giorgis F., J. Appl. Phys., vol. 96, p. 3987, 2004.
- Sussman R.S., Ogden R., Philos. Mag. B, vol. 44, p. 137, 1981.
- Swaaij R.A.C.M.M.V., Berntsen A.J.M., Van Sark W.G.J.H.M., Herremans H., Bezemer J., Van der Weg W.F., J. Appl. Phys., vol. 76, p.251, 1994.
- Swannepoel R. J., Phys. E: Sci. Instrum, 16, 1214, 1983a.
- Swannepoel R. J., Phys. E: Sci. Instrum, 17, 896, 1983b.
- Swhartz-Selinger T., von Keudell A., Jacob W., J. Appl. Phys., vol. 86, p.3988, 1996.
- Tanaka K., Maruyama E., Shimada T., Okamoto H., Amorphous Silicon, John Wiley & Sons, 1999.
- Tauc J., in: Optical Properties of Solids, edt. by Abeles F., North-Holland, Amsterdam, p. 277, 1972.
- Tauc J., Grigorovici R., Vancu A., Phys. Stat. Sol., vol. 15, p. 627, 1966.
- Tawada Y., Tsuge K., Condo M., Okamoto H., Hamakawata Y., J. Appl. Phys., vol. 53, p. 5273, 1982.
- Tean S.J., Jen W.P, Nerng F.S., Jyh W.H., Chun Y.C., IEEE Trans. Electron.Dev, 41 pp.1761, 1994.
- Tikhonravov A.V, Trubets M. K., OptiChar Software, Version 4.13., 2002
- Toneva A., Marinova T, Krastev V., Journal of Luminescence, 80, p455, 1999.
- Vorlicek V., Zatetova M., Pavlov S.K., Pajasova L., Journal of Non-Crystalline Solids, vol. 45, p. 289, 1981.
- Vorlicek V., Zatetova M., Pavlov S.K., Pajasova L., Journal of Non-Crystalline Solids, vol. 45, p. 289, 1981.
- Weaire D., Phys. Rev. Lett., vol. 26, p.1541, 1971.
- Weider H., Cardona M., Guarnieri C.R., Phys. Stat. Solid. B., vol. 62, p. 99, 1979.

Wooten F., Optical Properties of Solids, Academic Press, New York, 1972.

Yu P.Y., Cardona M., Fundamentals of Semiconductors, Springer-Verlag, Berlin, p. 247, 1996.

Zanatta A. R., Mulato M., Chambouleyron I., J. Appl. Phys, vol 84, p. 5184, 1998.

VITA

The author of this work was born in Kocaeli on November 19, 1976. He received his B.S. and M.S. degrees in physics at 1999 and 2002, both at Middle East Technical University (METU), Ankara. Since 2000, he has been employed as a teaching/research assistant by the Department of Physics at METU.

His main area of interest is structural, electrical and optical characterization of silicon based amorphous thin films for optoelectronic applications by FTIR, XPS, conductivity and transmittance measurements.

His publications include:

- Ismail Atilgan, Orhan Ozdemir, Baris Akaoglu, Kivanc Sel, Bayram Katircioğlu, ‘Transport Studies of Carbon-rich a-SiC_x:H Film Through Admittance and Deep-level Transient Spectroscopy Measurements’, Philosophical Magazine, Vol. 86, No. 19, 2771-2796, July 2006.
- Orhan Ozdemir, Ismail Atilgan, Baris Akaoglu, Kivanc Sel, Bayram Katircioğlu, ‘Frequency Dependence of Conductivity in Intrinsic Amorphous Silicon Carbide Film, Assessed Through Admittance Measurement of Metal Insulator Semiconductor Structure’, Thin Solid Films, 497, 149-156, 2006.
- Akaoglu B., Sel K., Atilgan I., Katircioğlu B., ‘Carbon Content Influence On The Optical Constants Of Hydrogenated Amorphous Silicon Carbon Alloys’, Optical Materials, (In press, 2006)